

## **UC Merced**

### **UC Merced Electronic Theses and Dissertations**

#### **Title**

Ultrafast optical parametric processes in photonic crystal fibers: fundamentals and applications

#### **Permalink**

<https://escholarship.org/uc/item/00b7q2ck>

#### **Author**

Gu, Chenji

#### **Publication Date**

2012

Peer reviewed|Thesis/dissertation

UNIVERSITY OF CALIFORNIA, MERCED

**Ultrafast optical parametric processes in photonic crystal fibers:  
fundamentals and applications**

A dissertation submitted in partial satisfaction of the  
requirements for the degree  
Doctor of Philosophy

in

Physics

by

Chenji Gu

2012

Copyright  
Chenji Gu, 2012  
All rights reserved.

The dissertation of Chenji Gu is approved, and it is acceptable in quality and form for publication on microfilm and electronically:

---

Jay E. Sharping

---

Boaz Ilan

---

Kenneth K.Y. Wong

---

Kevin A. Mitchell, Chair

University of California, Merced

2012

## TABLE OF CONTENTS

Signature Page . . . . .		iii
Table of Contents . . . . .		iv
List of Figures . . . . .		vi
Acknowledgements . . . . .		ix
Vita and Publications . . . . .		x
Abstract of the Dissertation . . . . .		xii
Chapter 1	Introduction and outline . . . . .	1
Chapter 2	Nonlinear optics and its application using photonic crystal fibers (PCFs) . . . . .	5
	2.1 Introduction to nonlinear fiber optics in PCF . . . . .	5
	2.2 Introduction to fiber-based optical parametric processes . . . . .	14
	2.3 Fiber optical parametric oscillators (FOPOs) for widely tunable light sources . . . . .	21
Chapter 3	Femtosecond operation of FOPOs . . . . .	28
	3.1 Performance in femtosecond region . . . . .	28
	3.2 Dispersive pulse broadening, walk-off, and gain-narrowing effects . . . . .	34
	3.3 Optimization of pulse duration for the sub-50fs generation . . . . .	38
Chapter 4	Picosecond operation of FOPOs . . . . .	43
	4.1 Performance in picosecond region . . . . .	43
	4.2 Asymmetric spectrum behavior . . . . .	50
	4.3 Cross-phase-modulation-induced spectral effects . . . . .	54
Chapter 5	Theoretical analysis of fiber optical parametric processes . . . . .	59
	5.1 Modeling ultrafast four-wave mixing . . . . .	59
	5.2 Simulation and experimental results . . . . .	66
	5.3 Further discussions . . . . .	68
Chapter 6	Spectrum reversal and temporal phase conjugation . . . . .	71
	6.1 Introduction to phase conjugation and time reversal . . . . .	72
	6.2 Concept of spectral mirror imaging and analytic theory . . . . .	78
	6.3 Analogy between spectral reversal and time reversal . . . . .	83

Chapter 7	Future studies . . . . .	87
Appendix A	Simulations of ultrashort pulse dynamics using split-step Fourier method . . . . .	89
Appendix B	Characterization of ultrafast optical pulses . . . . .	92
	B.1 Optical spectrum analyzer . . . . .	93
	B.2 Spectrogram and frequency-resolved optical gating (FROG) . . . . .	95
Bibliography	. . . . .	101

## LIST OF FIGURES

Figure 2.1:	Photograph of visible supercontinuum generation using highly nonlinear PCF. . . . .	7
Figure 2.2:	SEM cross section photograph of the sample PCF1. (a) the whole area of transverse section (b) the central area only . . .	10
Figure 2.3:	SEM cross section photograph of the sample PCF2. (a) the whole area of transverse section (b) the central area only . . .	11
Figure 2.4:	(a) Single pump optical parametric process. (b) Two photons (pump) are annihilated and two photons (signal and idler) are generated. . . . .	16
Figure 2.5:	(a) A single-pass optical parametric amplifier where a pump and signal are input to the system. (b) A optical parametric oscillator where only a pump is input, but cavity feedback results in coherent buildup of a signal. . . . .	22
Figure 2.6:	Schematic of generalized FOPO. . . . .	26
Figure 3.1:	The setup of FOPO utilizing a short PCF within a Fabry-Perot cavity. . . . .	30
Figure 3.2:	(a) Measured group velocity delay and inferred group velocity dispersion of the PCF3 used in these experiments. (b) SEM image of the PCF3. . . . .	31
Figure 3.3:	Experimental measurements of the output of the FOPO for a 27-mm long fiber. (a) Measured FROG spectrogram. (b) Retrieved temporal amplitude (solid line) and phase (dashed line). . . . .	32
Figure 3.4:	Measured spectra for both sidebands at high and low pump power for a 33-mm long fiber. Curves for 1W have been vertically offset for clarity. . . . .	33
Figure 3.5:	(a) The setup of FOPO utilizing a short PCF3 within a Fabry-Perot cavity. (b) Single pass FOPO model. . . . .	36
Figure 3.6:	(a) Pulse dispersion: $\Delta t_{dispersion} \approx  D(\lambda_i) \Delta\lambda_i L$ . (b) The pump-to-signal walk-off: $\Delta T_{walk-off} \approx  D(\lambda_c)  \lambda_i - \lambda_p L$ . (c) Gain narrowing effect. . . . .	37
Figure 3.7:	Reconstructed amplitude and phase in the time domain of the output of the FOPO measured on both sidebands for different fiber lengths. . . . .	39
Figure 3.8:	(a) Measurement of pulse duration as a function of fiber length at both output wavelengths ranges. (b) Measurement of center wavelength as a function of fiber length. . . . .	40
Figure 3.9:	Measurement of pulse duration as a function of fiber length at both output wavelengths ranges. . . . .	41
Figure 4.1:	The setup of FOPO utilizing a 1.2m-long PCF. . . . .	45

Figure 4.2:	The group velocity dispersion of the PCF used in these experiments. . . . .	46
Figure 4.3:	Calculated walk-off between pump and Stokes waves. . . . .	47
Figure 4.4:	Measured spectra from the reflection of prism. . . . .	48
Figure 4.5:	Retrieved output pulse from a FROG measurement . . . . .	49
Figure 4.6:	Measured output spectra at different pump power level. (a) Coupled pump at $535mW$ and output at $80mW$ . (b) Coupled pump at $484mW$ and output at $63mW$ . (c) Coupled pump at $432mW$ and output at $48mW$ . . . . .	51
Figure 4.7:	Measured output spectra at different cavity synchronization (a) Maxima output power at $80mW$ . (b) Shorten the cavity length by $0.056cm$ to get the output power at $60mW$ . (c) Shorten the cavity length by $0.16cm$ to get the output power at $45mW$ . . .	52
Figure 4.8:	Single pass mode with different initial pulse delay between pump and signal. . . . .	53
Figure 4.9:	Spectra at different pump power and synchronization conditions: theory and experiment. . . . .	56
Figure 5.1:	Schematic of a generalized FOPO for both femtosecond and picosecond operation. . . . .	62
Figure 5.2:	Simulations of two sideband spectrograms in femtosecond domain.	64
Figure 5.3:	Simulations of two sideband spectrograms in picosecond domain.	65
Figure 5.4:	Demonstration of SMI in the femtosecond domain. (a) Measured output spectrum from the femtosecond FOPO. From trace 1 to trace 3 one reduces the round-trip delay by $0.1$ ps per step. From left to right, the broadband spectra for each trace includes a signal sideband, a residual pump and an idler sideband. (b) Simulations of two spectral sidebands in the presence of a femtosecond pump pulse where $\tau$ is an initial delay between the pump and signal. The resulting spectra at $\tau=-80$ fs resemble the experimental measurement in trace 1. . . . .	67
Figure 5.5:	Demonstration of SMI in the picosecond domain. (a) Measured output spectrum from the picosecond FOPO. From trace 1 to trace 2 one reduces the round-trip delay by $8.3$ ps. (b) Simulations of two spectral sidebands in the presence of a picosecond pump pulse where $\tau$ is an initial delay between the pump and signal. The signal is the left trace and the idler is the right trace. The resulting spectra at $\tau=3$ ps resemble the experimental measurement in trace 1. . . . .	69
Figure 6.1:	Reflections (a) an ordinary mirror and (b) a phase-conjugate mirror. . . . .	73
Figure 6.2:	Geometry of phase conjugation by degenerate four-wave mixing.	75



Figure 6.3:	The concept of SMI. Two pulses, signal and idler, are depicted at the top left and right respectively, where the solid lines are the temporal amplitudes $ A_{1,2}(t) $ and dashed lines are the temporal phase profiles $\arg\{A_{1,2}(t)\}$ . Their spectral amplitudes $ \tilde{A}_{1,2}(\omega) $ are depicted at the bottom left and right with different center frequencies $\omega_{1,2}$ . The demonstration of SMI involves an additional pump pulse serving as the “mirror”. Two spectral sidebands appear as mirror images of one another about the center frequency of pump $\omega_0$ . . . . .	80
Figure 6.4:	Analogy between time reversal and spectrum reversal. The complex wavefunctions of electric fields are $E_{1,2}$ (the actual electric fields are the real parts $E_{1,2} = Re[E_{1,2}]$ ), the complex envelopes are $A_{1,2}$ and their center frequencies are $\omega_{1,2}$ . The center frequency of pump is $\omega_0$ . The wavevectors for optical beams are $k_{1,2}$ . The propagation constants for optical pulses are $\beta(\omega_{1,2})$ . . . . .	85
Figure B.1:	Measurement of spectral intensity with an optical spectrum analyzer. (a) Schematic of optical implementation using prisms. (b) System. . . . .	94
Figure B.2:	A spectral “interferometer” based on nonlinear effects generates an spectrogram in the frequency domain. . . . .	95
Figure B.3:	Schematic of a second-harmonic generation frequency-resolved optical gating. . . . .	98
Figure B.4:	Original and retrieved FROG data with the center wavelength at 1212 nm and a pulse duration of 86.35 fs. . . . .	99
Figure B.5:	A variety of measured spectrograms and retrieved pulses. (a) The pulse duration is 86.35 fs and the center wavelength is 1212 nm. (b) The pulse duration is 114.2 fs and the center wavelength is 1223 nm. (c) The pulse duration is 183.1 fs and the center wavelength is 1240 nm. (d) The pulse duration is 182.3 fs and the center wavelength is 1262 nm. . . . .	100

## ACKNOWLEDGEMENTS

First and foremost, I would like to thank my advisor, Prof. Jay E. Sharping, for all the help and support throughout my graduate study at University of California, Merced. During the past five years, he always gave me the continuous encouragement and free research environment. I learned a lot from his hands-on advice on experimental techniques. My special thanks also goes to my lab-mates: Dr. Yanhua Zhai, Leily Kiani, Jeremy R. Sanborn, Tessa Pinon, Thompson Lu. I have learned a lot from them and would like to express my appreciation for their technical help, stimulating conversations, and friendship.

Moreover, I would like to thank my committee members for their time. In particular, I would like to thank Prof. Raymond Chiao who had served on the committee chair of my qualifying exam. His classes PHYS238 “Quantum Mechanics II” and PHYS292 “Quantum Optics and Information” strongly influenced my PHD study.

My deepest gratitude goes to Prof. Boaz Ilan. I am greatly indebted to him for the long hours he spent on discussing the research with me. The discussions gave me a lot of valuable insights and resulted in most of the theoretical work presented in this thesis.

I would like to thank many scholars with whom I benefit a lot from the fruitful and enlightening discussions. In particular, my grateful thanks go to Dr. Katsunari Okamoto from AiDi Corporation, Yue Zhou and Prof. Kenneth K. Y. Wong from The University of Hong Kong, Prof. Yasuyuki Ozeki from Osaka University. Furthermore, I would like to thank Masaaki Hirano from Sumitomo Electric Industries, ltd. and Huifeng Wei from Yangtze Optical Fibre and Cable Co., Ltd., for the consultation of fibers and providing a variety of fibers to our lab.

Finally, I would like to thank my parents for their dedication and unconditional support throughout my graduate study over the Pacific ocean. Last but not least, I would like to thank my wife, Zaihong Shuai, for her constant support and understanding during the past few years. My Ph.D. also belongs to her.

## VITA

Ph.D. University of California, Merced  
*Major:* Physics, expected Dec. 2012

M.Sc, Southeast University, Nanjing, China  
*Major:* Photonics and Optoelectronics, Jun. 2007

B.Sc, Southeast University, Nanjing, China  
*Major:* Electrical Engineering, Jun. 2004

## PUBLICATIONS

### JOURNAL PUBLICATIONS

**Chenji Gu**, Boaz Ilan, and Jay E. Sharping, “*Demonstration of nondegenerate spectral reversal in optical frequency regime*”, submitted.

**Chenji Gu**, Boaz Ilan, and Jay E. Sharping, “*Nondegenerate spectral reversal and amplified frequency-to-time mapping through ultrafast optical parametric processes*”, preparing.

**Chenji Gu**, Christiane Goulart, and Jay E. Sharping, “*Cross-phase-modulation-induced spectral effects in high-efficiency picosecond fiber optical parametric oscillators*”, Opt. Lett., **36**, 8, 1488 (2011).

**Chenji Gu**, Huifeng Wei, Su Chen, Weijun Tong, and Jay E. Sharping, “*Fiber optical parametric oscillator for sub-50 fs pulse generation: optimization of fiber length*”, Opt. Lett., **35**, 20, 3516 (2010).

Jay E. Sharping, Christiane Pailo, **Chenji Gu**, Leily Kiani, and Jeremy R. Sanborn, “*Microstructure fiber optical parametric oscillator with femtosecond output in the 1200 to 1350 nm wavelength range*”, Opt. Express, **18**, 4, 3911 (2010).

### SELECTED PRESENTATIONS

**Chenji Gu**, Boaz Ilan, and Jay E. Sharping, “*Spectral mirror imaging in ultrafast optical parametric processes*”, **QF2G.8**, CLEO, 2012.

**Chenji Gu** and Jay E. Sharping, “*XPM-induced spectral distortion in high efficiency, picosecond, fiber optical parametric oscillators*”, **JThA012**, OFC, 2011.

**Chenji Gu**, Jay E. Sharping, Huifeng Wei, and Weijun Tong, “*Fiber length optimization in a dispersion compensated fiber optical parametric oscillator*”, **CTuM6**, CLEO, 2010.

**Chenji Gu**, Jay E. Sharping, Huifeng Wei, and Weijun Tong, “*Chirped sub-50 fs pulse generation: optimization of fiber length for ultrafast fiber optical parametric oscillators*”, **OTuJ4**, OFC, 2010.

Jay E. Sharping, Christiane Goulart-Pailo, and **Chenji Gu**, “*Pulsed fiber-optical parametric oscillators in the near infrared*”, **NThA4**, NLO (Nonlinear Optics: Materials, Fundamentals and Applications), 2009. (Invited)

**Chenji Gu**, Boaz Ilan, and Jay E. Sharping, “*Parabolic pulse generation in gain-guided optical fibers with nonlinearity*”, **ThZ2**, IEEE LEOS Annual Meeting, 2008.

ABSTRACT OF THE DISSERTATION

**Ultrafast optical parametric processes in photonic crystal fibers:  
fundamentals and applications**

by

Chenji Gu

Doctor of Philosophy in Physics

University of California, Merced, 2012

Facilitated by the advent of photonic crystal fibers two decades ago, the moded-locked fiber lasers become the new trend of ultrafast light sources. Nevertheless, their major limitations are the output wavelength range and pulse quality. Motivated by building widely tunable ultrashort light sources, this thesis focuses on the experimental and theoretical studies of fiber optical parametric process. As one important application of this process, fiber optical parametric oscillator (FOPO), promises to address the shortcomings of fiber lasers.

From the application point of view, it is important to manage and optimize the output performance of light sources such as the pulse duration, pulse shape, spectrum width and so on. So there is a need to clearly understand the pulse evolution from a platform of applied mathematics. Under this theoretical guidance, experimental work can be better oriented to develop functional light sources

which address needs for applications such as pulsed-light microscopy, multiphoton spectroscopy and so on.

We demonstrate FOPO as tunable light sources in both femtosecond and picosecond domains. For the femtosecond operation, we generate sub-50 *fs* pulses with linear chirp. The studies on the pulse quality are carried out where the fiber length inside the oscillator is varied. In particular, our studies focus on dispersive pulse broadening and walk-off effects which influence the performance of FOPO. The optimal condition, i.e., the shortest pulse duration, arises from the minimization of these two effects. For the picosecond operation, we generate pulses with the duration of 2 ~ 4 *ps*. The experiment also reveals that the spectral shape and width of output pulses are determined by cross-phase modulation and cavity synchronization. More precisely, the spectrum exhibits pump power dependent broadening which can be asymmetric with a red or blue shift depending on cavity synchronization. Moreover, the average power conversion efficiency is maximized by adjusting the cavity length to the long range of its operation which leads to a blue shifted spectrum.

To capture the operational principles and precisely emulate the performance of FOPO, we also focus on the theoretical analysis of fiber optical parametric processes. We extend the previous theory of partially degenerate four-wave mixing to the ultrafast situation where waves are all ultrashort pulses with broadband spectra. Then we perform the simulation based on justified parameters and compare our calculation results with experimental data. We find both experimentally and numerically that there exhibits an interesting symmetry behavior in the frequency domain - two widely separated spectral sidebands can always behave as mirror images of one another with respect to the center frequency of the controlling pump pulse. We call this interesting physical phenomenon “Spectral Mirror Imaging”. Not just limited to the numerical computation, under certain operation regime we obtain an analytic solution and clarify the physical mechanisms of this phenomenon. A simple analytical expression for the coupled governing equations of two sideband spectra is obtained, which reveals that the opposite values of group-velocity dispersion and the complex-conjugated parametric gain are the physical

mechanisms responsible for this phenomenon. Furthermore, we give a comparison between spectral reversal and time reversal.

# Chapter 1

## Introduction and outline

Photonic crystal fibers (PCF) give us numerous outstanding optical properties, such as endless single mode, high nonlinearity and controllable chromatic dispersion. Based on these novel properties, it is possible to make a variant of functional optical devices. For example, one can make compact and portable light sources which deliver output pulses with ultrashort durations and high energies. In particular, our research focus is on fiber based optical parametric oscillators (FOPOs) for widely tunable pulsed light sources. There are both fundamental and applied interests in the development of this kind of fiber-based nonlinear optical devices. We will discuss its tremendous applicability first.

Commercial solid-state laser systems are commonly used and quite successful, however, they are still expensive. During these years, facilitated by the development of PCFs there is a trend towards using ultrafast fiber lasers. Nevertheless, the major drawbacks of fiber lasers are their limited tunable wavelength and pulse duration. Operating through four-wave mixing (FWM) mediated by the nonlinearity of glass, FOPOs promise to address this shortcoming. Listed below are some major advantages for fiber-based devices in comparison with traditional bulk nonlinear crystals based systems. First, the FWM phase-matching bandwidth can be continuous and hundreds of nanometers wide. Thus, the generated two sidebands can be a few hundred nanometers from the input pump. Second, due to the endless single mode property of PCF the transverse mode quality of FOPOs is exceptionally good. Third, rather than using external energy supplies



from laser diode, FOPOs simply utilize the parametric process from optical waves which makes it convenient to further integrate with other fiber components and optical systems. Therefore, the widespread adoption of ultrafast systems will be greatly facilitated by the development of fiber-integrated synchronous ultrashort light sources.

From the application point of view, it is important to manage and optimize the output performance of light sources such as the pulse duration, pulse shape, spectrum width and so on. So there is a need to clearly understand the pulse evolution from a platform of applied mathematics. This heavy job is usually carried out by the numerical computation of partial differential equations. In particular, for the simulation of fiber-based optical parametric devices, instead of a single governing equation one needs to consider coupled nonlinear Schrödinger equations. Therefore, an important aim of this thesis is to understand the pulse generation and evolution in fiber-based optical devices. Under this guidance, our experimental work is aimed at building widely tunable pulsed light sources, which address needs for a lot of applications such as pulsed-light microscopy and spectroscopy. Interestingly, in our demonstration of this fiber optical parametric device there exhibits a noticeable symmetric phenomenon in the spectrum domain, which we call “spectral mirror imaging”. This interesting phenomenon is also verified by numerical computations.

Chapter 2 gives an introduction to nonlinear fiber optics and PCFs. In particular, we focus on the new opportunities in nonlinear fiber optics since the demonstration of PCFs. We discuss the configuration of FOPOs as widely tunable light sources. In order to develop some operational principles of this device, we also give an section to introduce on the theory of fiber optical parametric process under continuous-wave approximation.

Chapter 3 focuses on the operation of FOPOs in the femtosecond domain. Using a  $27\text{mm}$  fiber, we generate  $48\text{fs}$  pulses with linear chirp. The output ultrashort pulse is synchronized with  $400\text{fs}$  pump which is delivered by a mode-locked Yb-doped fiber laser. We study the pulse quality for both short-wavelength and long-wavelength operation where the fiber length inside the oscillator is varied from

17mm to 61mm. The optimal pulse duration is only observed in short wavelength operation. Furthermore, to better understand the optimal condition, we model the FOPO system as a single-pass parametric amplifier including dispersive pulse broadening and walk-off effect. The optimal condition arises from the minimization of the walk-off and dispersion. When walk-off is large, the parametric amplification process is most efficient over some reduced effective fiber length leading to an upper limit in the amount of observed pulse broadening.

Chapter 4 focuses on the operation of FOPOs in the picosecond domain. We generate pulses with the duration of  $2 \sim 4ps$  using 1.2m fiber. The output ultrashort pulses are synchronized with 8ps pump pulses which are delivered by a mode-locked Nd:Vanadate fiber laser. Our experiment also reveals that the spectral shape and width of output pulses are determined by cross-phase modulation and cavity synchronization. More precisely, the spectrum exhibits pump power dependent broadening which can be asymmetric with a red or blue shift depending on cavity synchronization. Moreover, the average power conversion efficiency is maximized by adjusting the cavity length to the long range of its operation. This leads to a blue shifted spectrum and conversion efficiency as high as 15% for 80mW of output and a 535mW of pump.

Chapter 5 focuses on the theoretical analysis of fiber optical parametric processes. We first extend the model of FWM process to the ultrafast situation, in which three waves, pump, signal and idler, are all ultrashort pulses with broadband spectra. Then we will show our simulation results based on justified parameters and compare our simulations with experimental results. We found both experimentally and numerically that there exhibits an interesting physical phenomenon, which we call “spectral mirror imaging”.

Chapter 6 focuses on the analytic theory and physics of “spectral mirror imaging”. Not just limited to the discussion of simulations results, under certain operation regime we obtain an analytic solution and clarify the physical mechanisms of this phenomenon. Furthermore, we give a comparison between spectral reversal and time reversal.

During the course of our study, several new interesting directions are iden-

tified but have not been detailedly explored in this thesis. We briefly give an introduction on some of them in Chapter 7. Furthermore, there are some important calculation methods and experimental techniques used as tools when we referred in this thesis. On the one hand, since a lot of theoretical work in this thesis depends on the simulation of ultrashort pulse propagation we need to discuss an effective numerical computation method. On the other hand, we discuss a novel technique for the characterization of ultrashort pulses.

In Appendix A, we discuss the split-step Fourier method for the numerical computations of nonlinear Schrödinger equation. This is a powerful tool for simulations of ultrashort pulses propagation and their interactions.

In Appendix B, we focus on the technical details of a measurement technique to capture the temporal and spectral information of ultrashort optical pulses within nonlinear optical fibers. As the fastest available photodetector to date is still too slow, we introduce a technique called frequency-resolved optical gating to perform this great job.

# Chapter 2

## Nonlinear optics and its application using photonic crystal fibers (PCFs)

In this chapter, we first give an introduction to nonlinear fiber optics and PCFs. In particular, we focus on the new opportunity in nonlinear fiber optics since the demonstration of PCFs.

Then we discuss the configuration of fiber optical parametric oscillators (FOPOs) for widely tunable light sources. In order to have a deeper understanding of fiber optical parametric processes and develop some operational principles of this device, FOPO, we give an introduction to the theory of fiber optical parametric process under continuous-wave approximation.

### 2.1 Introduction to nonlinear fiber optics in PCF

The invention of the LASER (Light Amplification by Stimulated Emission of Radiation) in 1960 [1] boomed the development of a new field - nonlinear optics. This is because the optical field is so strong that the response of medium can not be treated linearly. Shortly after this invention, there were various observations of nonlinear phenomena, such as second harmonic generation (SHG) [2], stimulated Raman scattering (SRS) [3], stimulated Brillouin scattering (SBS) [4], and four-

wave mixing (FWM) [5]. However, all these early experimental reports were in bulk materials or liquids. At that time, concerning optical fibers, however, the silica fibers were available but exhibiting very high losses and small nonlinearities. The revolution happened in 1970 as low losses optical fibers were demonstrated in Corning [6]. Soon after this, pioneered by Dr. Stolen and other researchers at Bell Lab a variety of nonlinear effects including SBS and SRS, self-phase modulation (SPM), FWM [7, 8, 9, 10, 11, 12]<sup>1</sup> and various advancements of optical solitons [14, 15, 16] were achieved by using silica fibers. The advent of photonic-crystal fibers (PCFs) two decades ago stimulated this area, nonlinear fiber optics.

Before we go to the introduction of PCFs, the key question we first need to answer is why using fiber as nonlinear media. In comparison with bulk materials, other than compact and portable, fibers can offer very long interaction distance. Furthermore, the nonlinearity of the material (silica) is small, but the effective nonlinearity is high<sup>2</sup> due to the small fiber core. Therefore, the nonlinear effects can be observed at relatively low power levels. These properties make fibers ideal to build nonlinear optical devices.

---

<sup>1</sup>Please refer to Ref. [13] for the early works on nonlinear fiber optics.

<sup>2</sup>We will show later in Eq. (2.6) that the nonlinear coefficient are inversely proportional to fiber core.

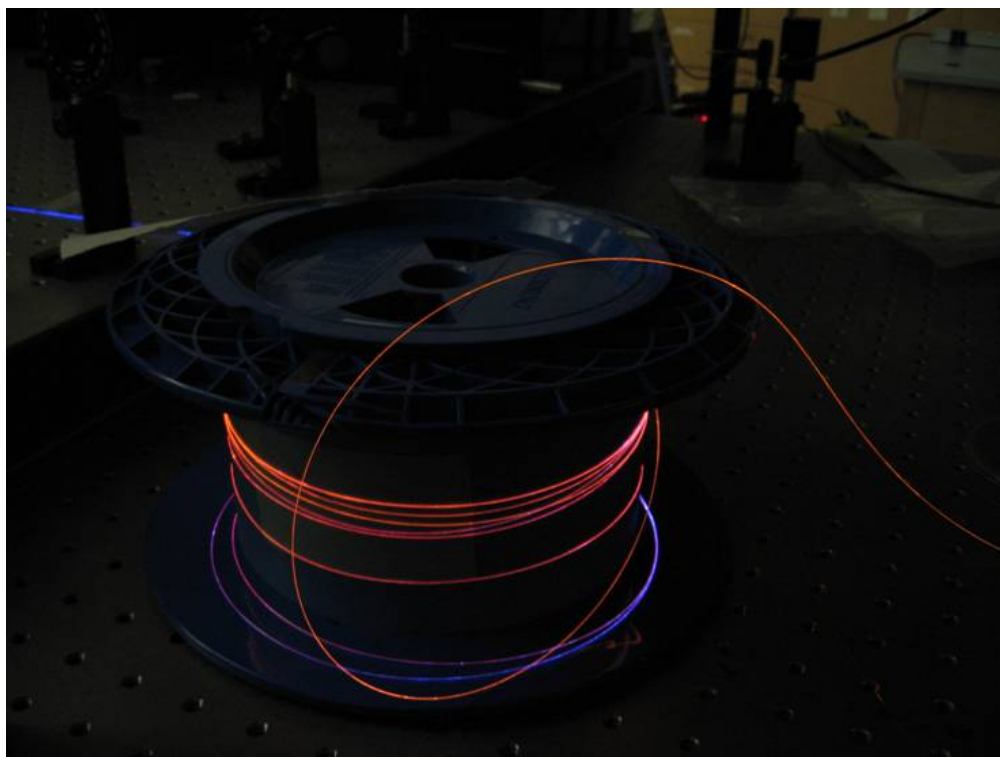


**Figure 2.1:** Photograph of visible supercontinuum generation using highly nonlinear PCF.

The study of PCF began in the early 1990s [17]. The initial motivation of this kind of fiber is to guide optical wave by means of a photonic bandgap effect. Therefore, rather than highly nonlinearity, the first successful PCF can guide optical waves because of an effective refractive index difference between a solid silica core and a surrounding cladding region containing a transverse microstructure of air holes. Although index guiding in PCF is conceptually similar to the guidance in conventional fibers<sup>3</sup>, there exists the additional degrees of freedom by engineering the air-hole geometry resulting in unattainable guidance properties in standard fiber. Furthermore, the strong waveguide contribution to the dispersion made it possible to obtain zero-dispersion wavelengths (ZDW) in the visible or near infrared region, very far from the intrinsic material value of fused silica (around  $1.3 \mu m$ ). As an example as shown in Fig. 2.1, the demonstration of supercontinuum at visible wavelength in our lab looks magically colorful. This feature is due to the shifting ZDW close to the pump wavelength. The demonstration of highly nonlinear PCF has led to a variety of technological advancements such as high-brightness sources, precise measurements of fundamental physical constants [18, 19, 20, 21, 22, 23], or even mature commercial products.

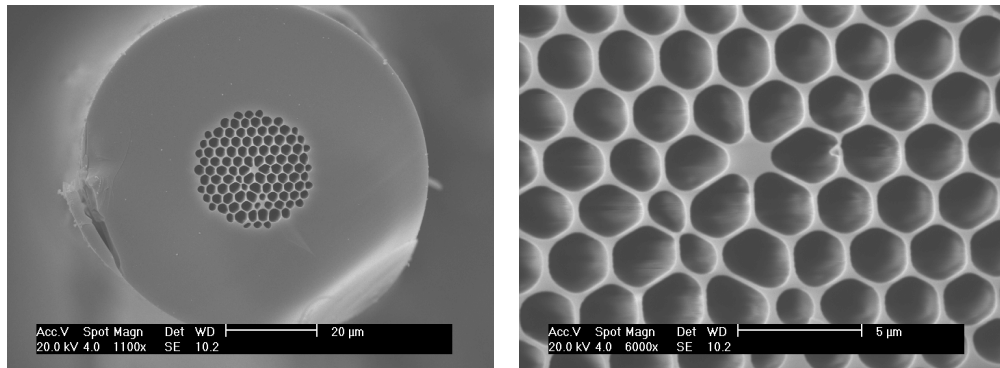
More comprehensively, not just limited to highly nonlinearity and shift ZDW to short wavelength, let us take a detail look at other outstanding properties of PCFs. This new class of fiber is referred to other names such as holey fiber, hole-assisted fiber, or microstructure fiber. Pioneered by Prof. Philip Russell's research group [17], PCFs give unique optical property that is impossible in conventional optical fibers. In particular, the control over transverse geometrical pattern of fibers leads to the freedom to design their outstanding optical properties. One can spatially vary an arrangement of very tiny and closely spaced air holes which go through the whole length of fiber. Such air holes can be obtained by using a preformed design with holes, made by stacking capillary tubes. These "lattices", the relative size of the holes and small displacements among them, lead to different designs of the hole pattern. These designs result in a variety of interesting optical properties as follows. First, it is possible to obtain a high numerical aperture of 0.7

---

<sup>3</sup>Index guide in conventional fibers refers to the total internal refraction between the fiber core and the cladding area due to their index contrast.

for multimode fibers [24]. Second, the single-mode guidance over wide wavelength regions (endlessly single-mode fiber) can also be obtained for small ratios of hole size and hole spacing [25]. Third, extremely small or extremely large mode areas are achievable, which leads to either very strong or very weak optical nonlinearities. Fourth, even for large mode areas, low sensitivity to bend losses were achieved by the special design of PCFs [26, 27]. Fifth, instead of index guiding of conventional fibers certain design of hole arrangements can result in a photonic bandgap. The significance of this is that a higher refractive index in the inner part is no longer required, where the guidance is possible even in a hollow core. This property made the advent of air-guiding hollow-core fibers, which are interesting for dispersive pulse compression at high pulse energy levels by filling gases or liquids into the hollow-core. This is highly useful in fiber-optic sensors, or for variable power attenuators. Sixth, asymmetric hole patterns can lead to extremely strong birefringence for polarization-maintaining fibers [28] as well as polarization-dependent fibers [29, 30]. In summary, there are substantial design freedoms available for PCFs, which yields different combinations of desirable parameters of fibers for the applications in fiber-optic communications, fiber lasers, nonlinear optical devices, high-power transmission, highly sensitive gas sensors, and other areas [31].

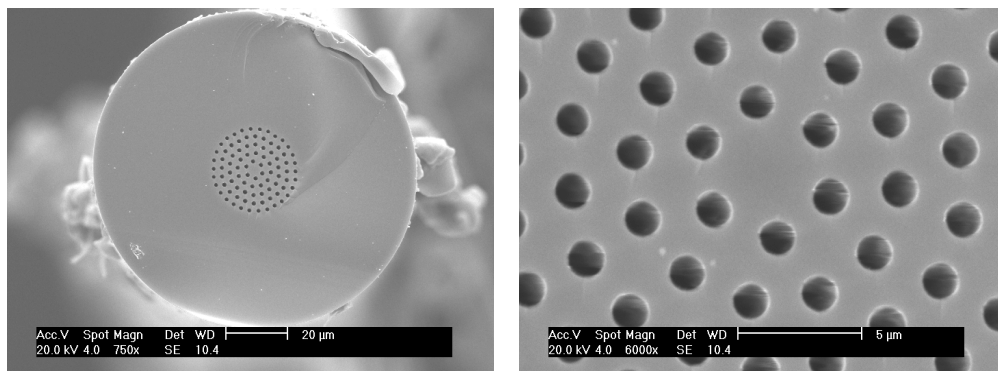




(a)

(b)

**Figure 2.2:** SEM cross section photograph of the sample PCF1. (a) the whole area of transverse section (b) the central area only



(a)

(b)

**Figure 2.3:** SEM cross section photograph of the sample PCF2. (a) the whole area of transverse section (b) the central area only

As an example of PCF design, i.e., the transverse hole pattern, shown in Fig. 2.2 and Fig. 2.3 are scanning electron microscope (SEM) of two sample fibers from our collaborator - Yangtze Optical Fibre and Cable Co., Ltd. The design of PCF1 is shown in Fig. 2.2, which is a piece of nonlinear photonic crystal fiber guide optical waves in a small silica core, surrounded by a high air filling ratio microstructured cladding formed by a periodic arrangement of air holes in silica. The optical properties of the core closely resemble those of a rod of glass suspended in air, resulting in strong confinement of the light. Some key parameters of this fiber are high nonlinear coefficients (about  $40W^{-1}km^{-1}$  at  $1550nm$ ), ZDW around  $715nm$  and near-Gaussian mode profile over the widely near IR wavelength. This piece of fiber is ideal for supercontinuum generation pumped by Ti:Sapphire or other ultrafast laser sources. Using this fiber, one can convert ultrafast lasers into a compact, low-cost, ultra-bright supercontinuum source. The design of PCF2 is shown in Fig. 2.3, this piece of fiber is single-mode nonlinear photonic crystal fiber, with ZDW around  $950nm$  and nonlinear coefficient about  $11W^{-1}km^{-1}$  at  $1030nm$ . Furthermore, this fiber is available spliced to standard single mode fiber or other endlessly single mode PCFs, and is also available with hermetically sealed ends for the patch cord connection.

As the design of PCF can engineer the dispersion curve of the fibers, in principle, one can shift the ZDW of fibers to any visible or near infrared wavelength. Thus, our discussion below will not be sensitive at where center wavelength is, although the focus of this thesis will be at the wavelength window of  $1\ \mu m$ . In the remaining contents of this section, we will give an introduction to the temporal and spectral property of nonlinear ultrashort pulses propagation inside optical fibers.

We first start to consider a dispersive medium with nonlinear responses, and some major steps for the derivation of governing equations are summarized here.<sup>4</sup> We consider a simple case that an input pulse at the carrier frequency  $\omega_0$  is launched such that it excites a single mode of the fiber. Furthermore, we assume that the pulse maintains its linear polarization (the  $x$  axis) during the propagation

---

<sup>4</sup>For the detail discussion, please refer to Ref. [32].

along the fiber length (the  $z$  axis), the electric field can be written in the form

$$\mathbf{E}(\mathbf{r}, t) = \hat{x}F(x, y, \omega_0)A(z, t)e^{i(\beta_0 z - \omega_0 t)}. \quad (2.1)$$

where  $\hat{x}$  is a unit vector along the  $x$  axis, and  $F(x, y, \omega)$  represents the spatial distribution of the fiber. Here we assume that the spectrum bandwidth of pulse is not very wide ( $\Delta\omega \ll \omega_0$ ). So  $F(x, y, \omega)$  is a constant at the carrier frequency  $\omega_0$ . Furthermore, it is also useful to remove the rapidly varying part of the optical field at this frequency and introduce a slowly varying pulse envelope  $A(z, t)$ .

On the other hand, one can rewrite the optical fields in the frequency domain by Fourier transform.

$$\mathbf{E}(\mathbf{r}, t) = \frac{1}{2\pi} \int_{-\infty}^{\infty} \hat{x}F(x, y, \omega)A(\omega) e^{i[\beta(\omega)z - \omega t]} d\omega, \quad (2.2)$$

The physical meaning of Eq. (2.2) is that although each spectral component of the input field propagates as a plane wave, there exhibits a slightly different phase shift among them. This is because the propagation constant  $\beta(\omega)$  is frequency dependent. Moreover, we will expand  $\beta(\omega)$  in a Taylor series at a carrier frequency  $\omega_0$  as

$$\beta(\omega) = \beta_0 + (\omega - \omega_0)\beta_1 + \frac{1}{2}(\omega - \omega_0)^2\beta_2 + \dots, \quad (2.3)$$

where each order of dispersion parameters are defined as  $\beta_m = (d^m\beta/d\omega^m)_{\omega=\omega_0}$ .

If only the Kerr and Raman contributions to the nonlinear polarization are included, one can obtain the slowly varying pulse envelope  $A(z, t)$  satisfying the following propagation equation [32]:

$$\begin{aligned} \frac{\partial A}{\partial z} + \frac{\alpha}{2}A = & i \sum_{m=1}^{\infty} \frac{i^m \beta_m}{m!} \frac{\partial^m A}{\partial t^m} \\ & + i\gamma \left(1 + \frac{i}{\omega_0} \frac{\partial}{\partial t}\right) \times (A(z, t) \int_0^{\infty} R(t') |A(z, t - t')|^2 dt'), \end{aligned} \quad (2.4)$$

where fiber losses is  $\alpha$ , the nonlinear coefficient is

$$\gamma = \frac{\omega_0 n_2(\omega_0)}{c A_{eff}}, \quad (2.5)$$

and the parameter

$$A_{eff} = \frac{[\int \int |F(x, y, \omega_0)|^2 dx dy]^2}{\int \int |F(x, y, \omega_0)|^4 dx dy} \quad (2.6)$$

is known as the effective mode area which is related to the optical mode extending beyond the core region of the fiber. This effective mode area is generally proportional to the size of the fiber core. Note that we assume the nonlinear parameter  $n_2$  is independent on frequency.

Since in Eq. (2.4) the nonlinear response function,  $R(t)$ , includes both the electronic and Raman (nuclear) contributions, we assume that the electronic contribution is nearly instantaneous and Raman contribution suffers from a delay. Then the functional form of  $R(t)$  can be written as

$$R(t) = (1 - f_R)\delta(t) + f_R h_R(t). \quad (2.7)$$

One can find in Ref. [33] for the typical parameters of the silica fibers, where the Raman response function is  $h_R(t)$  and the fractional contribution  $f_R \approx 0.18$ .

Under certain operational region [32], Eq. (2.4) can be simplified as:

$$\frac{\partial A}{\partial z} + \frac{\alpha}{2}A + \frac{i\beta_2}{2}\frac{\partial^2 A}{\partial T^2} - \frac{\beta_3}{6}\frac{\partial^3 A}{\partial T^3} = i\gamma(|A|^2 A + \frac{i}{\omega_0}\frac{\partial}{\partial t}(|A|^2 A) - T_R A \frac{\partial |A|^2}{\partial T}). \quad (2.8)$$

where  $\alpha$  is the fiber loss (in inverse meters  $1/m$ ),  $\gamma$  is the fiber nonlinearity (in inverse Watt meters  $(Wm)^{-1}$ ),  $\beta_2$  is second-order dispersion of the fiber (in seconds squared per meter  $(s^2/m)$ ),  $\beta_3$  is third-order dispersion of the fiber (in seconds cubed per meter  $(s^3/m)$ ),  $T_R$  incorporates the Raman effect with delayed nonlinearity.

## 2.2 Introduction to fiber-based optical parametric processes

Optical parametric process is a well-known phenomenon in nonlinearly media. A typical example in bulk nonlinear material is SHG based on second-order nonlinearity. The similar process also happens in optical fibers exploiting the third-order nonlinearity, relying on highly efficient FWM. In particular, we will focus on the partially degenerated case including three optical waves: one pump at  $\omega_0$ , one signal at  $\omega_1$  and one idler at  $\omega_2$ . As shown in Fig. 2.4 (a), the frequencies of the two waves, signal and idler, are symmetrically positioned on each side of the

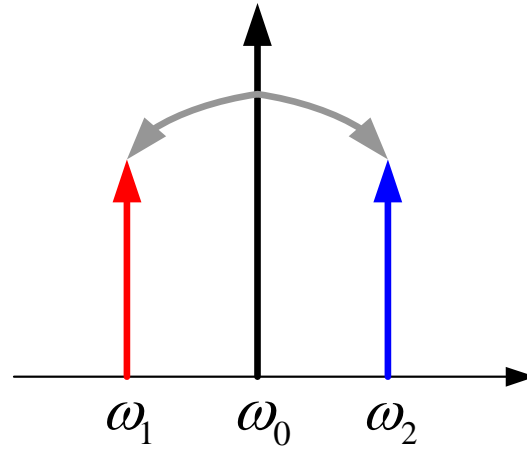
pump. And the optical property of these three waves should satisfy following two relationships:

$$2\omega_0 = \omega_1 + \omega_2, \quad (2.9)$$

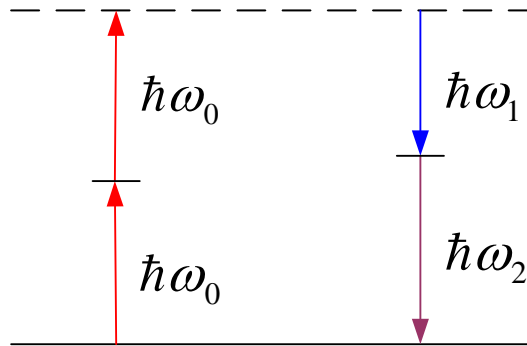
$$\Delta\beta = \beta(\omega_1) + \beta(\omega_2) - 2\beta(\omega_0) = 0, \quad (2.10)$$

where  $\beta\omega_j = \omega_j n(\omega_j)/c, j = \{0, 1, 2\}$  is the propagation constant of each wave,  $n$  is the reflective index,  $c$  is the speed of light in vacuum, and  $\Delta\beta$  is the lower power propagation mismatch.

Equations (2.9) and (2.10) indicate that fiber parametric process based on third-order nonlinearity can be understood from a quantum mechanical point of view. As shown in Fig. 2.4 (b), the degenerate parametric amplification is manifested as the annihilation of two pump photons at frequency  $\omega_0$  and the generation of a signal and an idler photon at frequencies  $\omega_1$  and  $\omega_2$ , respectively. The conversion needs to satisfy the photon energy conservation relation as shown in Fig. 2.4 (b) which is microcosmic energy conservation relation as indicated in Eq. (2.9). Equation (2.10) generally regarded as phase-match condition actually indicates the relation of photon momentum conservation. We will show later that the contribution from the Kerr nonlinear effect can strongly influence this phase-match condition.



(a)



(b)

**Figure 2.4:** (a) Single pump optical parametric process. (b) Two photons (pump) are annihilated and two photons (signal and idler) are generated.

Now we give a more detailed discussion to the fiber optical parametric process from an electromagnetic point of view. This process involves the interaction of three copolarized waves whose complex amplitudes (slowly varying electric fields) are  $A_0(z)$ ,  $A_1(z)$  and  $A_2(z)$ , respectively. Based on the relation of photon energy conservation, i.e., Eq. (2.9), three carrier waves (stationary collinearly polarized monochromatic waves) are at frequencies  $\omega_0, \omega_1 = \omega_0 - \Omega, \omega_2 = \omega_0 + \Omega$ , respectively. Assuming the transverse mode of three waves are the same during their propagation, the total electric field propagating along a single-mode optical fiber may be written as:

$$E(z) = [A_0(z)e^{i(\beta_0 z - \omega_0 t)} + A_1(z)e^{i[\beta_1 z - (\omega_0 - \Omega)t]} + A_2(z)e^{i[\beta_2 z - (\omega_0 + \Omega)t]}], \quad (2.11)$$

where  $\beta_0 = \beta(\omega_0)$ ,  $\beta_1 = \beta(\omega_0 - \Omega)$ , and  $\beta_2 = \beta(\omega_0 + \Omega)$  are the propagation constants evaluated at the relative frequencies for pump, signal and idler, respectively.

To clarify the physics of parametric optical process, before we give the formulation of governing equations, let us take a brief review on the assumptions we had made till now. First, we assume that the three waves interact through the intensity-dependent refractive index (i.e., a purely nonlinear Kerr effect) with instantaneous response of the fiber. Second, the nonlinear susceptibility is nearly constant over the range of frequencies considered (the nonlinear parameter  $n_2$  is independent on frequency), Third, the Raman-scattering process does not affect the parametric exchange of energy among the waves (i.e., the susceptibility is real). Then (the fourth assumption), we further consider that the process is nearly phase matched, so that the usual assumption of neglecting the generation of higher-order harmonics can be made. Under these hypotheses, three waves satisfy the coupled governing equations are obtained as [32, 34, 35, 36]:

$$\frac{dA_0}{dz} = i\gamma[(|A_0|^2 + 2(|A_1|^2 + |A_2|^2))A_0 + 2A_1A_2A_0^*e^{i\Delta\beta z}], \quad (2.12)$$

$$\frac{dA_1}{dz} = i\gamma[(|A_1|^2 + 2(|A_2|^2 + |A_0|^2))A_1 + A_2^*A_0^2e^{-i\Delta\beta z}], \quad (2.13)$$

$$\frac{dA_2}{dz} = i\gamma[(|A_2|^2 + 2(|A_1|^2 + |A_0|^2))A_2 + A_1^*A_0^2e^{-i\Delta\beta z}]. \quad (2.14)$$

On the right-hand side of Eq. (2.12)-(2.14), the first two terms are responsible



for the nonlinear phase shift due to SPM and XPM, respectively. The last term is responsible for the energy flow among the three interacting waves. These three equations (Eqs. (2.12) to (2.14)) are named as coupled nonlinear Schrödinger equations (NLSE).

Furthermore (the fifth assumption), assuming the system is under the strong pump approximation, i.e.,  $A_0(z) \gg A_{1,2}(z)$ , based on three coupled Eqs. (2.12)-(2.14) one can simplify as,

$$\frac{dA_0}{dz} = i\gamma|A_0|^2A_0 \quad (2.15)$$

$$\frac{dA_1}{dz} = i\gamma 2|A_0|^2A_1 + i\gamma A_0^2 A_2^* e^{-i\Delta\beta z} \quad (2.16)$$

$$\frac{dA_2}{dz} = i\gamma 2|A_0|^2A_2 + i\gamma A_0^2 A_1^* e^{-i\Delta\beta z}. \quad (2.17)$$

The first equation is for the pump amplitude, and can be integrated for the solution as,

$$A_0 = A_{p0} e^{i\gamma|A_{p0}|^2 z} = \sqrt{P_0} e^{i\gamma P_0 z} \quad (2.18)$$

where  $|A_{p0}|^2 = P_0$  is the pump power at  $z = 0$ , which implies that the pump signal does not lose any energy. This is justified if signal and idler are still small as the assumption we made is pump undepleted. Then the signal and idler amplitudes can now be described with the two coupled equations given as

$$\frac{dA_1}{dz} = 2i\gamma P_0 A_1 + i\gamma P_0 e^{i\kappa z} A_2^*, \quad (2.19)$$

$$\frac{dA_i}{dz} = 2i\gamma P_0 A_i + i\gamma P_0 e^{i\kappa z} A_2^*, \quad (2.20)$$

where the parameter, phase mismatch, is defined as,

$$\kappa = 2\gamma P_0 + \Delta\beta. \quad (2.21)$$

We will show later that phase mismatch plays the key role in the operation of fiber optical parametric processes. Here, we will discuss an important parameter for the characterization of the tunable range fiber optical parametric processes - the parametric gain profile.

The coupled Eqs. (2.19) and (2.20) above describe a strong pump and a weak signal launched together at the fiber input such that the pump remains

undepleted during the parametric gain process. These two coupled eqs. can be solved analytically, and the unsaturated single pass gain  $G_1$  is written [39, 40],

$$\begin{aligned} G_1 &= \frac{P_1(L)}{P_1(0)} = 1 + \left[ \frac{\gamma P_0}{g} \sinh(gL) \right]^2 \\ &= 1 + (\gamma P_0 L)^2 \left[ 1 + \frac{gL^2}{6} + \frac{gL^4}{120} + \dots \right]^2, \end{aligned} \quad (2.22)$$

where  $L$  is the fiber interaction length and the parametric gain coefficient  $g$  is given by  $g^2 = [(\gamma P_0)^2 - (\kappa/2)^2] = -\Delta\beta[\frac{\Delta\beta}{4} + \gamma P_0]$ . In Chapter 4, we will use this relation to estimate the tunable range of FOPOs (the dashed line) and compare with our experimental demonstration, as shown in Fig. 4.4.

Let us go back to Eqs. (2.12)-(2.14) and rewrite them in terms of powers and phases of the waves as some further insights can be revealed. Let  $P_j(z) = |A_j(z)|^2$  and  $\phi_j(z)$ , where  $A_j(z) = \sqrt{P_j} e^{i\phi_j}$  for  $j \in \{0, 1, 2\}$ .

$$\frac{dP_0}{dz} = -4\gamma(P_0^2 P_1 P_2)^{1/2} \sin \theta \quad (2.23)$$

$$\frac{dP_1}{dz} = 2\gamma(P_0^2 P_1 P_2)^{1/2} \sin \theta \quad (2.24)$$

$$\frac{dP_2}{dz} = 2\gamma(P_0^2 P_1 P_2)^{1/2} \sin \theta \quad (2.25)$$

$$\begin{aligned} \frac{d\theta}{dz} &= \Delta\beta + \gamma(2P_0 - P_1 - P_2) + \gamma[(P_0^2 P_1 / P_2)^{1/2} \\ &\quad + (P_0^2 P_1 / P_2)^{1/2} - 4(P_1 P_2)^{1/2}] \cos \theta, \end{aligned} \quad (2.26)$$

where  $\theta(z) = \Delta\beta z + 2\phi_0(z) - \phi_1(z) - \phi_2(z)$  describes the relative phase difference between the three waves. The first term of  $\theta$  on the right hand side of Eq. (2.26) describes the linear phase shift, while the second and third term describe the nonlinear phase shift.

By inspecting three governing Eqs. (2.23) to (2.26), one can identify the opportunity to direct the power flow among three waves by controlling their relative phase relation. In particular, the direction can be from the pump to the signal-idler ( $\theta = \pi/2$ , parametric amplification) or from the signal-idler to the pump ( $\theta = -\pi/2$ , parametric attenuation). This gives us the possibility to create a phase-sensitive amplifier, which has potential applications in low-noise amplifier [37].

For the more commonly used and practical application of a phase-insensitive fiber-based parametric processes which are the focus of this thesis, we may consider

an intense pump at  $\omega_0$  and a weak signal at  $\omega_1$ . The idler is assumed to be zero and the relative phase difference is in a special case,  $\theta = \pi/2$ , at the input end of fiber. This can be understood by realizing that the idler will be generated after an infinitesimal propagation distance in the fiber [38]. Furthermore, suppose within small propagation distance the interaction of three waves still make the operation in the phase-matched condition  $\theta(z)$  remains near  $\pi/2$ . Then Eq. (2.26) may be simplified as following equation,

$$\frac{d\theta}{dz} \approx \Delta\beta + \gamma(2P_0 - P_1 - P_2) \approx \Delta\beta + 2\gamma P_0 = \kappa. \quad (2.27)$$

where the phase mismatch parameter  $\kappa$  is introduced in a different way from the approach of Eq. (2.21). Moreover, assuming higher-order dispersion is neglectible we can rewrite the propagation mismatch as,

$$\Delta\beta = \beta(\omega_1) + \beta(\omega_2) - 2\beta(\omega_0) \approx -\frac{2\pi c}{\lambda_{zero}^2} \frac{dD}{d\lambda} (\lambda_0 - \lambda_{zero})(\lambda_0 - \lambda_1)^2, \quad (2.28)$$

where  $dD/d\lambda$  is the slope of the dispersion at the ZDW, pump at  $\lambda_0$  and ZDW is  $\lambda_{zero}$ . The approximation we made is linearly dependent dispersion curve within a small bandwidth separation between the pump and signal-idler ( $\lambda_0 - \lambda_1 \ll \lambda_0$ ). Using the relation in Eq. (2.28) to consider the phase-matched condition, Eq. (2.27), gives a crucial operation principle of fiber optical parametric processes: When the pump wavelength  $\lambda_0$  is positioned in the normal dispersion regime ( $\lambda_0 < \lambda_{zero}$  and  $\Delta\beta > 0$ ), the phase mismatch will accumulate and increase with the growth of signal, wavelength at  $\lambda_1$ , thus decreasing the resulting efficiency of the process. By positioning the pump wavelength in the anomalous dispersion regime ( $\lambda_0 > \lambda_{zero}$  and  $\Delta\beta < 0$ ), it is possible to compensate the nonlinear phase mismatch  $2\gamma P_0$  using the linear phase mismatch  $\Delta\beta$ .

In a more general case, for the simulation of the performance of fiber optical parametric processes one need to have the numerical calculations based on Eqs. (2.15) to (2.17) which include a depleted pump, higher order dispersion and a nonlinear phase shift. We will discuss this important approach more detailedly in Chapter 5 and Appendix A.

For a fixed pump wavelength at  $\lambda_0$ , the gain versus signal wavelength  $\lambda_1$  will thus be formed in two lobes on each side of  $\lambda_0$ , where the peak of each lobe

is at the wavelength that meets the relation  $\kappa = \Delta\beta + 2\gamma P_0 = 0$ . This process is identical to the phenomenon that is also referred to as modulation instability [32], i.e., the parametric process establishes a balance between GVD and the nonlinear Kerr effect.

Note that the theoretical analysis presented here in this section based on coupled Eqs. (2.12)-(2.14) only apply for CW or long-pulsed pump. In the rest of chapters, either the experiments or the theories, where most of work this thesis focused on, will be at the ultrashort situation. The purpose of this introduction is to clarify some physics meanings and the operational principles of fiber-based optical parametric devices.

## **2.3 Fiber optical parametric oscillators (FOPOs) for widely tunable light sources**

In the previous section, we gave an introduction to fiber optical parametric processes. Based on these theoretical understandings, we will discuss one important application of nonlinear optical devices - FOPOs.

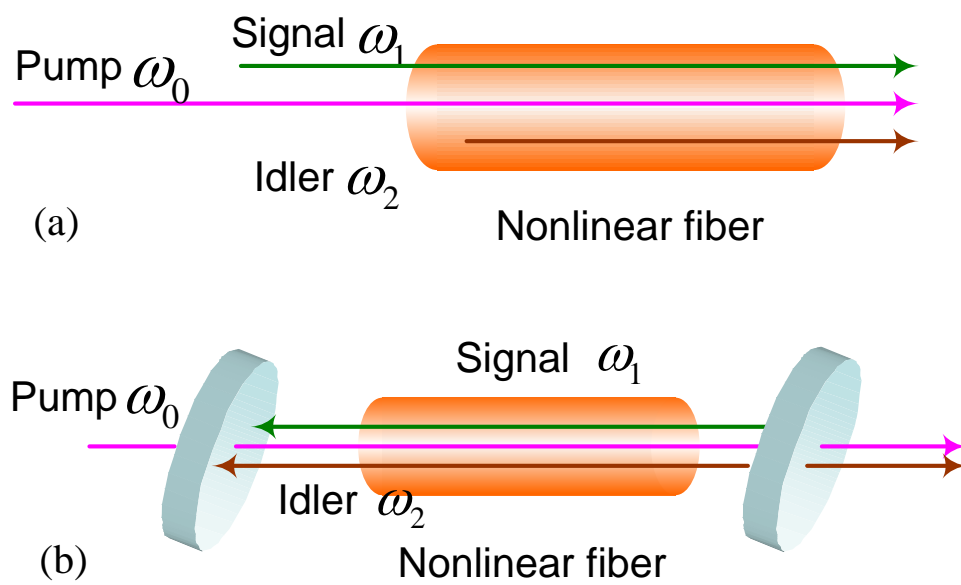


**Figure 2.5:** (a) A single-pass optical parametric amplifier where a pump and signal are input to the system. (b) An optical parametric oscillator where only a pump is input, but cavity feedback results in coherent buildup of a signal.

First, there are two configurations based on optical parametric processes illustrated schematically in Fig. 2.5. Let us have a comparison between these two, a single-pass optical parametric amplifier and a optical parametric oscillator. Shown in Fig. 2.5 (a) is a parametric amplifier which includes both *pump* and *signal* fields at the input where the energy flow is from the strong pump to the weaker signal-idler resulting in the amplification of signal and generation of idler. As we discussed above in Eq. (2.9), the relation of energy conservation indicates the generation of a third “conjugate” (we refer this as “idler” in this thesis) field whose frequency is at  $\omega_2 = 2\omega_0 - \omega_1$ . The generation of the idler field also means that this configuration, optical parametric amplifier, can be used for wavelength conversion.

The configuration shown in Fig.2.5 (b) is an oscillator where there is only a pump coupled input to the system, but the presence of feedback as the design of cavity structure allows for the coherent buildup of the amplified spontaneous emission (ASE) in a manner similar to laser action. There is usually some sort of filter within the cavity that prevents both of the sidebands from oscillating which would result in undesirable phase-sensitive operation [41].

Before we go to the detail of design and operation of this configuration, however, the first question one may ask is that what is the motivation for non-linear fibers based devices and why not just keep on using the already popular solid-state laser systems. It is true that solid-state laser systems often use crystals for stable generation of wavelength-agile short pulsed laser radiation [42]. One can have synchronous short pulses trains at different wavelengths, and the wavelength can be widely tunable at certain frequency domain. These pulse trains are useful in pump-probe measurements such as probing the carrier lifetimes in semiconductors and spectroscopically resolving fast chemical and biological reactions [43, 44, 45]. These commercial solid-state laser systems are quite successful and commonly used, but they are still kind of expensive. During these years, facilitated by the development of PCFs there is a trend towards using ultrafast fiber lasers. The major limitations of fiber lasers are their range of tunable wavelength and quality of pulse duration. Operating through FWM mediated by the nonlinearity of glass, FOPOs

promise to address this shortcoming. Some major advantages for fiber-based devices in comparison with crystals based systems [41] are as follows. Since the FWM phase-matching bandwidth can be continuous and hundreds of nanometers wide, the output occurs at wavelengths either longer or shorter than that of the input pump. The transverse mode quality of fiber-based oscillators is exceptionally good due to the endless single mode property of PCF. Furthermore, a fiber-based gain medium lends itself to further integration with fiber components. The widespread adoption of ultrafast systems will be greatly facilitated by the development of fiber-integrated wavelength-agile synchronous sources. So one of our motivations is to develop compact tunable pulsed light sources.

More detailedly, operating through FWM and mediated by the third-order nonlinearity, FOPOs can enhance the performance of mode-locked fiber lasers through greater wavelength flexibility and shorter pulse durations [41, 46]. The pump laser delivers a stable high-power pulse train at a fixed wavelength while FOPOs enable conversion to other wavelengths. As the design of PCF allows engineering dispersion, i.e., shifting the ZDW, novel PCFs have extended FOPO functionality from visible wavelengths to the infrared [47, 48]. These FOPO systems deliver complimentary functionality as compared with the relatively mature bulk material to build optical parametric light sources based on second-order nonlinearity. Furthermore, our intention also refer to the optimal capability of pulsed FOPOs [49] and to exploit these systems as new light sources for applications in other areas [50, 51]. Operating over a broad range of wavelengths, pulse durations, and output powers [41, 48, 52], the design of FOPO ranges from fiber integrated to mostly bulk where the design is determined by usability versus performance trade-offs [53, 54]. The need for greater fiber integration and optimization of FOPOs provides motivation for identifying the primary physical mechanisms that govern the output. For an example in nonlinear microscopy, it is critical to know what governs the spectral width and quality of output spectrum. This will be covered in chapter 4. There are also some practical applications of FOPO systems reported by our group [55]. Since parametric amplification is an ultrafast process based on the electronic susceptibility of the materia, there is no long-lived excited state, so

the FOPO cavity must be aligned so that it is synchronous with that of the pump laser cavity. The goal is to amplify the small portion of feedback after each round trip through the system, and so a new pump pulse must be passing through the fiber and synchronized with existing feedback pulses. Additionally, the ultrafast pump pulses can experience distortion upon propagation through the fiber. When the cavity is perfectly aligned then the system produces a stable pulse train with a minimum of amplitude fluctuations. Unstable amplitude fluctuations are present if the cavity is not perfectly synchronous.

Figure show the basic design of FOPO, where . As we discussed in the previous section, based on Eqs. (2.27) and (2.28), it is critical to choose a fiber with suitable dispersion curve to obtain wideband parametric amplification [41]. One needs to choose a fiber and pump wavelength so that the system operates in the small transition region between anomalous and ZDW. The system will still operate over a fairly wide bandwidth when the pump laser is tuned slightly into the anomalous GVD, and in practice the system is much easier to align under this situation. Oscillation is considerably more challenging to obtain for operation even slightly into the region of normal GVD. This is because it is hard to compensate for the nonlinear phase mismatch  $2\gamma P_0$  by the linear phase mismatch  $\Delta\beta$  as we discussed in the previous section based on Eqs. (2.27) and (2.28). However, if the pump wavelength is tunable one can achieve a different design of FOPOs whose parametric gain profiles are isolated narrow spectrum-band [56] by imposing pump wavelength in normal GVD region of fibers.

The cavity lifetime is also an interesting consideration. Most of systems described in this thesis have relatively lossless cavity mirrors at the oscillating wavelength, but suffer significant loss due to fiber input coupling. It is reasonable to estimate that the round-trip loss is more than 70%. The system depicted in Fig. 2.6 will operate at a center wavelength corresponding to the peak of the parametric gain. Wavelength tunability can be introduced by including a dispersive element within the cavity. If sufficient dispersion is added then the optical path length depends on wavelength. As such, the wavelength at which synchronous operation is achieved depends on the position of one of the end mirrors within the cavity.



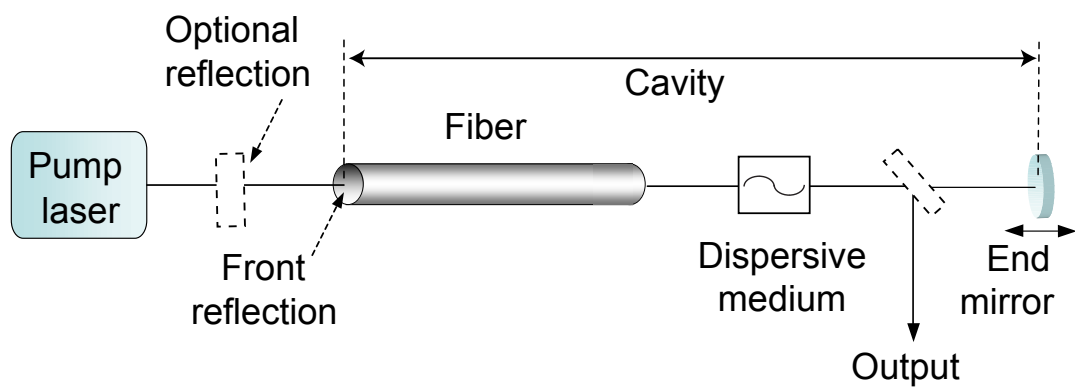


**Figure 2.6:** Schematic of generalized FOPO.

In order to identify the optimum oscillating signal feedback condition one must consider shifting pump energy as much as possible to the output fields. Using this system we can independently adjust the feedback of the oscillating signal to obtain the optimum pump depletion. For example, by introducing an intracavity filter detuned from the oscillator's phase-matched frequency conversion efficiencies considerably higher than those possible when operating at the phase-matched frequency are demonstrated [57].

# Chapter 3

## Femtosecond operation of FOPOs

In this chapter, our discussion focuses on the generation of  $48fs$  pulses with linear chirp using a short ( $27mm$ ) fiber based on the configuration of FOPO. The output ultrashort pulse is synchronized with pump which is delivered by a mode-locked Yb-doped fiber laser. We study the pulse quality for both short-wavelength and long-wavelength operation where the fiber length inside the oscillator is varied from  $17mm$  to  $61mm$ . The optimal pulse duration is only observed in short wavelength operation.

Furthermore, to better understand the optimal condition, we model the FOPO system as a single-pass optical parametric amplifier including dispersive pulse broadening and walk-off between the pump and output. The optimal condition arises from the minimization of the walk-off and dispersion. When walk-off is large, the parametric amplification process is most efficient over some reduced effective fiber length leading to an upper limit in the amount of observed pulse broadening.

### 3.1 Performance in femtosecond region

The detailed FOPO setup in our experiment is illustrated in Fig. 3.1. The pump laser source is a  $400 \pm 30fs$ ,  $50MHz$  mode-locked Yb-doped fiber laser (PolarOnyx, Inc. Uranus) with a polarized output centered at  $1032nm$  [58]. The coupled average pump power was adjusted to be  $1.0W$  for all of the measurements.

Pump light is coupled into the Fabry-Perot cavity via a glass window where Fresnel reflections provide sufficient feedback for oscillation. The repetition rate of FOPO cavity is the same as laser and the output is synchronized with pump laser. The FOPO can oscillate due to feedback from either surface of “Window” and we adjust to use the right-most surface (see Fig. 3.1). The “Q”-factor of the cavity is low, but the parametric gain provided by phase-matched FWM compensates for the loss. This piece of fiber, PCF3, is not designed to be birefringent, but fibers of this type generally exhibit birefringence with a difference in refractive indices on the order of  $10^{-5}$ . We observe variations in the amount of SPM of the pump, and there are two maximal polarization-maintaining modes. The FOPO can oscillate on either mode. The output was experimentally verified to be co-polarized with respect to the pump. One can change the output wavelength range by switching the mirror (see Fig. 3.1) from a longpass dielectric mirror to a shortpass dielectric mirror. The output is obtained from the front coated surface of the dielectric mirror while the back uncoated surface can be used to monitor the oscillating wave and residual pump. For the long-pass mirror there is oscillation of long wavelengths while the short wavelengths are coupled out. For the short-pass mirror there is oscillation of short wavelengths while the long wavelengths are coupled out. To clarify the nomenclature used in this chapter, we refer to the oscillating portion of the spectrum as “signal” and the output-coupled portion of the spectrum as “idler”.

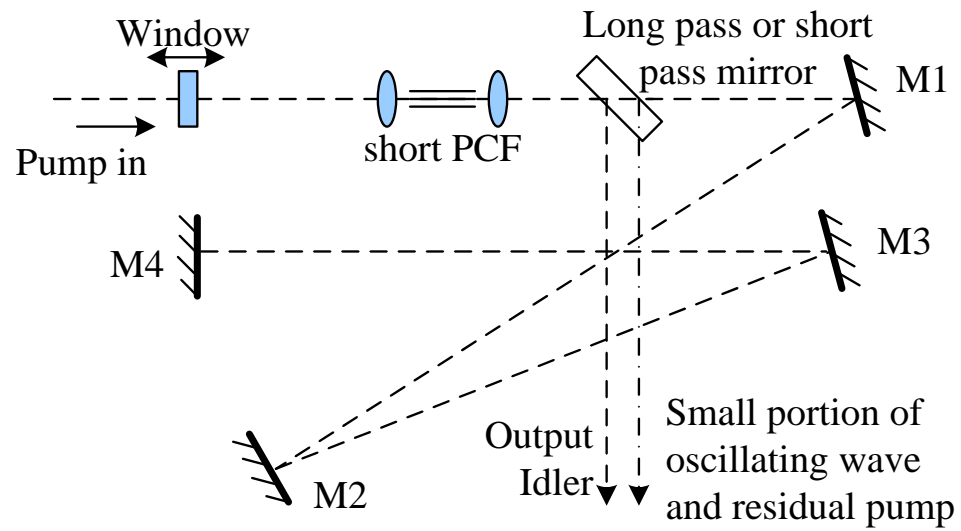
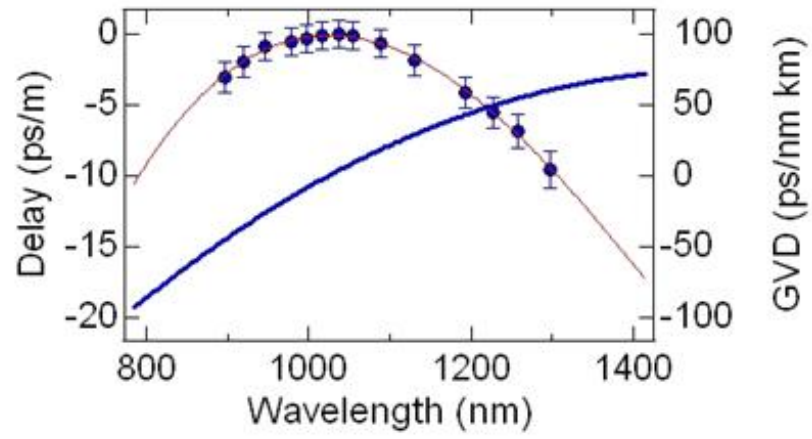
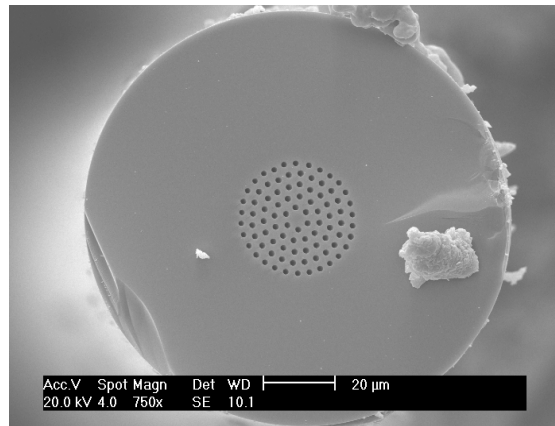


**Figure 3.1:** The setup of FOPPO utilizing a short PCF within a Fabry-Perot cavity.

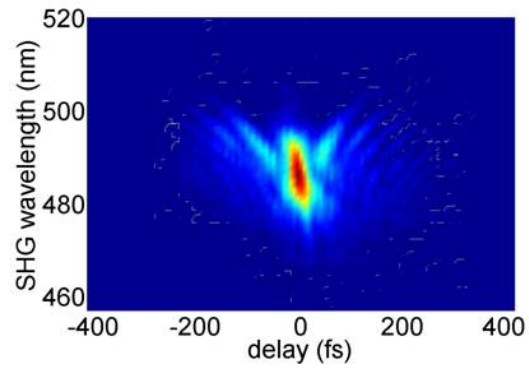


(a)

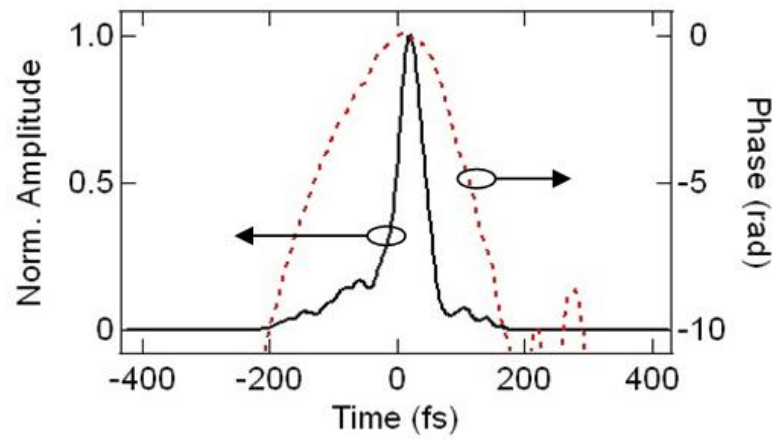


(b)

**Figure 3.2:** (a) Measured group velocity delay and inferred group velocity dispersion of the PCF3 used in these experiments. (b) SEM image of the PCF3.



(a)



(b)

**Figure 3.3:** Experimental measurements of the output of the FOPO for a 27-mm long fiber. (a) Measured FROG spectrogram. (b) Retrieved temporal amplitude (solid line) and phase (dashed line).

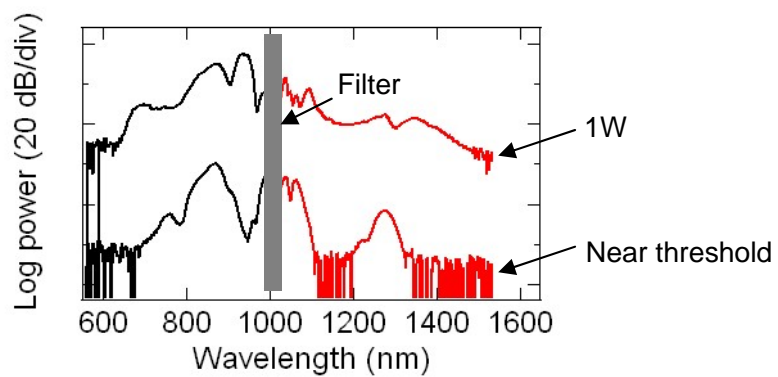


**Figure 3.4:** Measured spectra for both sidebands at high and low pump power for a 33-mm long fiber. Curves for 1W have been vertically offset for clarity.



This piece of optical fiber, PCF3, was provided by Yangtze Optical Fibre and Cable Co. Ltd. At  $1060\text{nm}$  it has a nonlinear coefficient of  $11(\text{W} \cdot \text{km})^{-1}$ , a mode field diameter of  $3.6 \pm 0.1\mu\text{m}$ , and an attenuation of  $3.0\text{dB}/\text{km}$ . As illustrated in Fig. 3.2, our measurement of the zero dispersion wavelength for this fiber is  $1030\text{nm}$ . We characterized the output of the FOPO for different fiber lengths ranging from  $17\text{mm}$  to  $61\text{mm}$ , where the fibers were individually cut and cleaved from the same fiber spool. Second harmonic generation frequency resolved optical gating (SHG-FROG) was used for the characterization [59].

Shown in Fig. 3.3 are measurements of FOPO output at short wavelengths for a fiber length of  $27\text{mm}$ . Figure 3.3 (a) is the measured SHG-FROG trace showing the power at the second harmonic as a function of time and wavelength. The temporal amplitude in Fig. 3.3 (b) implies a pulse duration of  $48\text{fs}$ , and the newly quadratic temporal phase profile suggests that the pulse has linear chirp. Similar data sets were recorded for the other seven fiber lengths tested in this experiment. For all of these cases the average output power is  $70 \pm 10\text{mW}$ .

Shown in Fig. 3.4 are typical optical spectra sampled from a FOPO incorporating a  $33 - \text{mm}$  long fiber and configured to output short wavelengths. Near the oscillation threshold there are sidebands centered at  $870\text{nm}$  and  $1270\text{nm}$ . When the average pump power increases to  $1.0\text{W}$  the output peak wavelength occurs at  $940\text{nm}$  while the long wavelength sideband broadens over a range from  $1100\text{nm}$  up to  $1450\text{nm}$ . Spectral behavior within the band labeled “Filter” in the diagram is in the transition region of the output mirror. The broad spectrum of the output is due to the broad parametric gain bandwidth [52].

## 3.2 Dispersive pulse broadening, walk-off, and gain-narrowing effects

For crystal OPOs based on second order nonlinearity, the formation of signal pulses over multiple passes through the system has been studied [60, 61]. Walk-off between the injected and generated pulses plays a major role in compression of the output pulses. A full understanding requires a series of careful simulations, but in

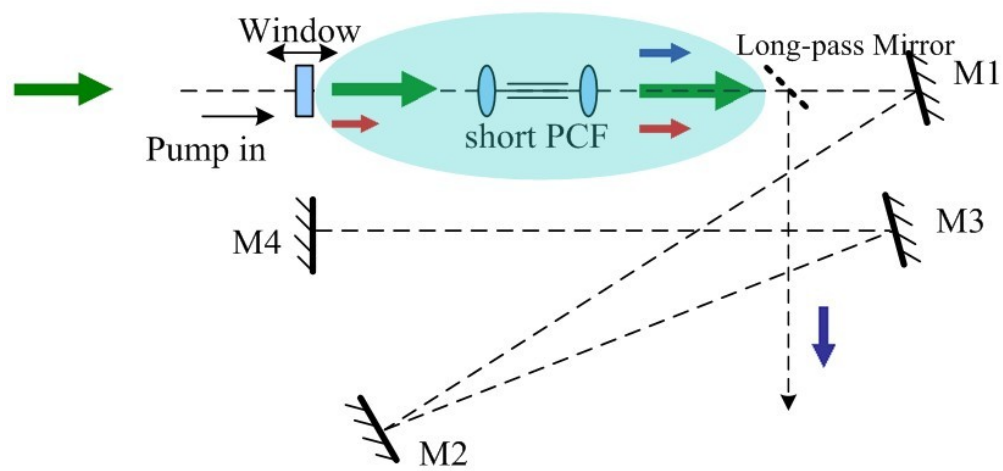
order to develop some intuition about this system, as illustrated in Fig. 3.5, we consider a single-pass optical parametric amplifier process and include dispersive pulse broadening of the idler, walk-off between the pump and idler pulses, and pulse narrowing due to enhanced gain near the peak of the pump pulse (gain narrowing effect). The idler is coupled out of the cavity immediately as it emerges from the fiber.

We define  $D(\lambda_i)$  as the dispersion parameter,  $\Delta\lambda_i$  is the spectral full width at half maximum (FWHM) of the idler pulse, and  $L$  is the length of fiber. The dispersive pulse broadening is given by:  $\Delta t = |D(\lambda_i)|\Delta\lambda_i L$ , as shown in Fig. 3.6 (a). The magnitude of the walk-off between the pump and idler pulses [49, 62], as shown in Fig. 3.6 (b), is given by:  $\Delta T = |D(\lambda_c)||\lambda_i - \lambda_p|L$ , where  $\lambda_i$  is the output wavelength,  $\lambda_p$  is the pump wavelength and  $\lambda_c = (\lambda_i + \lambda_p)/2$ .

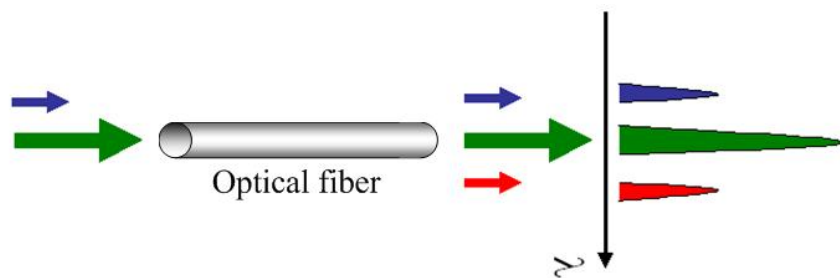
The signal and idler pulses propagate slightly slower through the fiber than the pump pulse does; so due to the amplification from parametric gain, the idler pulse will emerge longer in duration than would be the case for negligible walk-off. However, gain narrowing provides an upper limit to the amount of broadening. Gain narrowing occurs because the gain depends approximately exponentially on the pump power. The gain is much larger at the peak of the pump pulse leading to output pulses much narrower than the pump. For example, if a small CW signal interacts with a strong Gaussian pump pulse, the output is a Gaussian pulse with a temporal FWHM given by [52]:

$$\tau_{effective} = 2T_p \sqrt{-\frac{1}{2} \ln\left(1 - \frac{\ln 2}{2\gamma P_0 L}\right)} \quad (3.1)$$

where  $P_0$  is the peak power of the pump pulse and  $T_p$  is the pulse duration of the pump. Typically  $P_0 \approx 50kW$  and  $T_p \approx 400fs$  for these experiments. And  $\tau_{effective}$  is about  $40fs$  for the  $27mm$  fiber length. The whole process is illustrated in Fig. 3.6 (c).



(a)



(b)

**Figure 3.5:** (a) The setup of FOPO utilizing a short PCF3 within a Fabry-Perot cavity. (b) Single pass FOPO model.

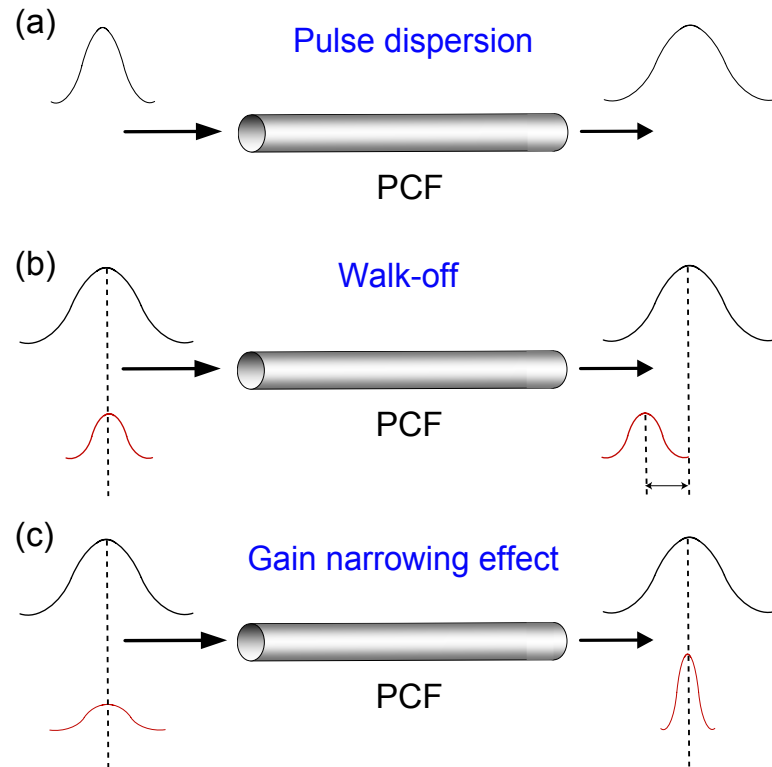


**Figure 3.6:** (a) Pulse dispersion:  $\Delta t_{dispersion} \approx |D(\lambda_i)|\Delta\lambda_i L$ . (b) The pump-to-signal walk-off:  $\Delta T_{walk-off} \approx |D(\lambda_c)||\lambda_i - \lambda_p|L$ . (c) Gain narrowing effect.

We consider the case of small walk-off ( $\Delta\tau < \tau_{effective}$ ) and large walk-off ( $\Delta\tau > \tau_{effective}$ ) separately. For small walk-off, the signal and idler pulses are almost always within the center region of pump pulse. In this case, the combined effects of walk-off and dispersive pulse broadening will stretch the output pulse in additive fashion according to  $\tau_{signal} = \Delta T + \Delta t$ . For the large walk-off situation, the signal and idler pulses pass quickly through the center region of pump pulse. The OPA process is most efficient over some reduced effective fiber length leading to an upper limit to the amount of observed pulse broadening. The limit is given by the gain narrowed pulse duration,  $\tau_{effective}$ . In total, the pulse duration for the large walk-off case is obtained by adding the gain-narrowed pulse duration and dispersion according to  $\tau_{signal} = \tau_{effective} + \Delta t$ .

### 3.3 Optimization of pulse duration for the sub-50fs generation

Plots of pulse duration as a function of fiber length are shown in Fig. 3.7 (a). For short wavelength operation, as the fiber length increases from  $17mm$  up to  $27mm$ , the pulse duration decreases at a linear rate of  $5fs/mm$ . The minimum pulse duration of  $48fs$  is obtained for a fiber length of  $27mm$ . From  $27mm$  up to  $61mm$  the pulse duration increases at a linear rate of  $1.4fs/mm$ . The system can be operated using fibers longer than  $61mm$  but measurements are unreliable due to a large amount of supercontinuum. For long wavelength operation where the pulse duration increases from  $132fs$  up to  $250fs$ , the results are also shown in Fig. 3.7 (a). Furthermore, plots of wavelength as a function of fiber length are shown in Fig. 3.7 (b). Fig. 3.8 shows detail temporal information (pulse profile and temporal phase) for some typical data points in Fig. 3.7 (a).

A comparison of our experimental data points with the model we discussed in section 3.2 is shown in Fig. 3.9. The central wavelength and FWHM are taken as input parameters, The output performance for short-wavelengths for all of the fibers tested corresponds to the case of small walk-off. The output at long-wavelengths corresponds to the case of large walk-off.

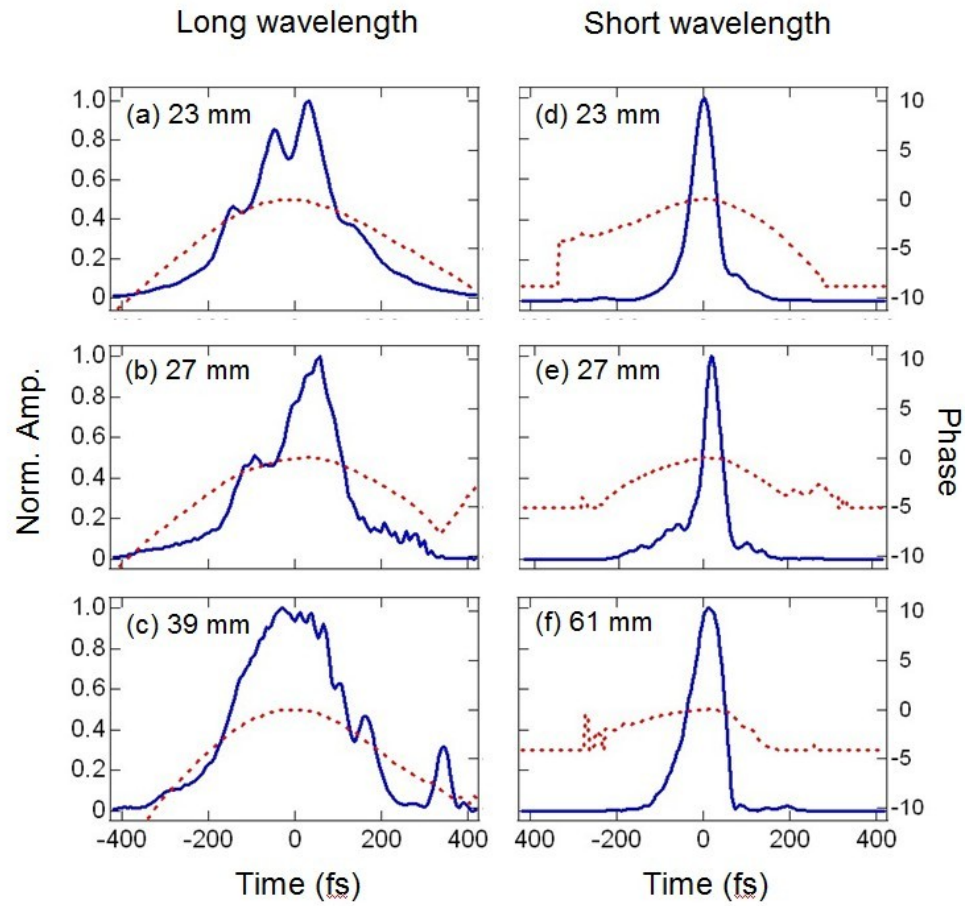
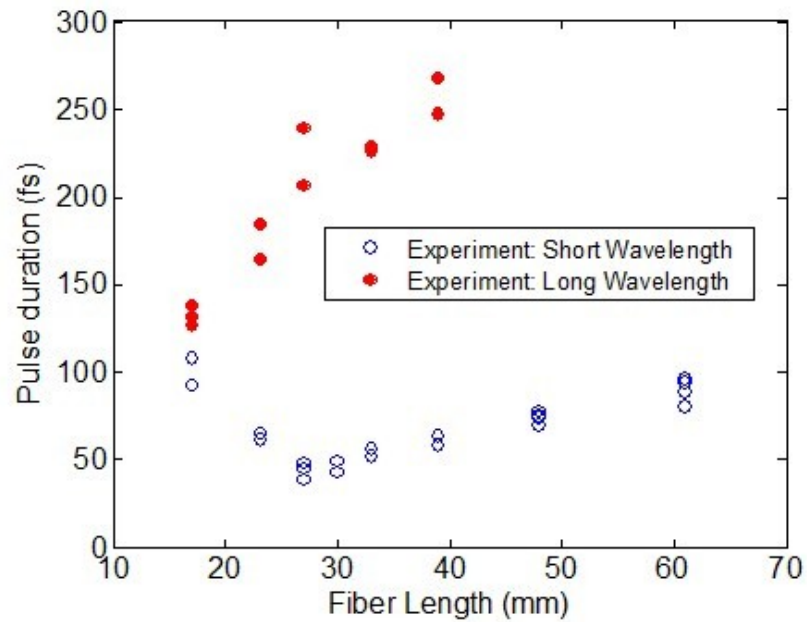
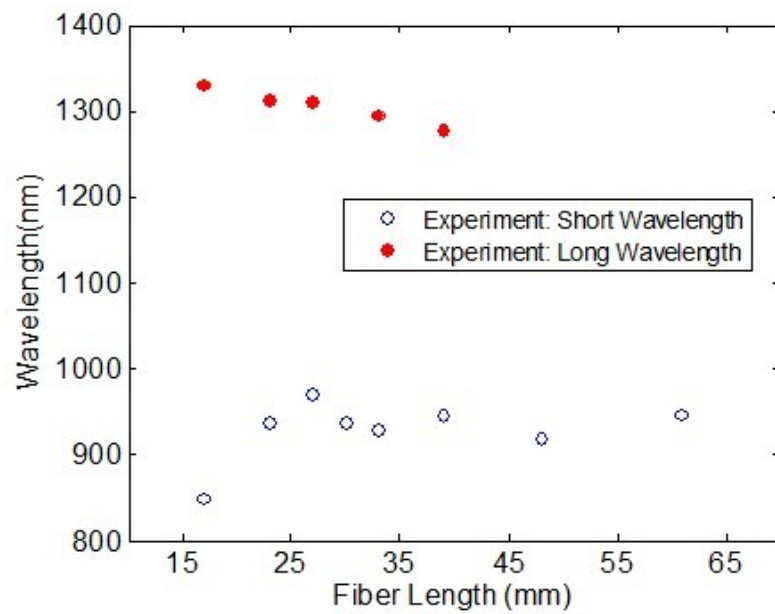


**Figure 3.7:** Reconstructed amplitude and phase in the time domain of the output of the FOPO measured on both sidebands for different fiber lengths.



(a)



(b)

**Figure 3.8:** (a) Measurement of pulse duration as a function of fiber length at both output wavelengths ranges. (b) Measurement of center wavelength as a function of fiber length.

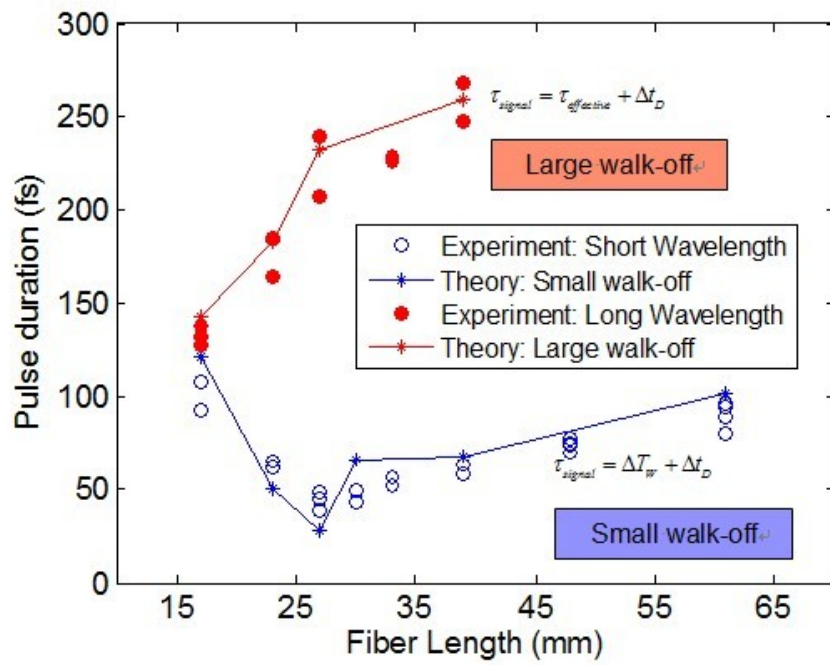


**Figure 3.9:** Measurement of pulse duration as a function of fiber length at both output wavelengths ranges.



There are three issues with the analyses given above. Firstly, the model indicates that a longer fiber length will lead to a smaller  $\tau_{effective}$ . However, for the case of a high gain FOPO incorporating a long fiber, the peak power,  $P_0$ , of the pump pulse decreases along the length of the fiber leading to a longer  $\tau_{effective}$ . Secondly, the calculation of  $\tau_{effective}$  assumes a Gaussian-shaped pump pulse. For pump pulses exhibiting a more complicated shape [49],  $\tau_{effective}$  may be longer. Thirdly, we have ignored the potential broadening or compression produced by the dichroic mirror used for output coupling. We experimentally find that a single reflection from this mirror generates less than  $5fs$  of pulse broadening of the idler.

Reconstructed amplitude and phase in the time domain of the output of the FOPO measured on both sidebands for different fiber lengths. (a) Measurement of pulse duration as a function of fiber length at both output wavelengths ranges. (b) Measurement of center wavelength as a function of fiber length.

In summary, we generate  $48fs$  pulses using a  $27mm$  fiber within a FOPO configuration. We propose a model for the output pulse duration including pump-to-output walk-off, intra-pulse dispersion and gain narrowing. Optimal pulse durations are obtained when walk-off and dispersion are minimized by choosing a suitable fiber length and output wavelength. We report on a FOPO capable of delivering pulses as short as 48 fs in duration. We explore the variation in system performance as a function of the length of fiber used in the oscillator. For short wavelength operation ( $840nm$  to  $970nm$ ) an optimal fiber length of  $27mm$  generates a pulse duration of 48 fs with a center wavelength at  $970nm$ . This optimal condition arises from the minimization of dispersion, and walk-off between the pulsed pump and output. In contrast, we do not observe an optimal fiber length when the system is configured for the output ranging from  $1250nm$  to  $1330nm$ .

# Chapter 4

## Picosecond operation of FOPOs

In this chapter, our discussion focuses on the generation of a few picoseconds pulses (duration of  $2 \sim 4ps$ ) using  $1.2m$  fiber based on the configuration of FOPO. The output ultrashort pulses are synchronized with pump pulses which are delivered by a mode-locked Nd:Vanadate fiber laser.

Our experiment also reveals that the spectral shape and width of the output pulses are determined by cross-phase modulation (XPM) and cavity synchronization. The spectral behavior is explained by a single pass pulse propagation model. The spectrum exhibits pump power dependent broadening which can be asymmetric with a red or blue shift depending on cavity synchronization. Moreover, the average power conversion efficiency is maximized by adjusting the cavity length to the long range of its operation. This leads to a blue shifted spectrum and conversion efficiency as high as 15% for  $80mW$  of output and a  $535mW$  of pump.

### 4.1 Performance in picosecond region

Figure 4.1 illustrates our experimental setup. The pump laser delivers transform-limited  $8ps$  pulses at a repetition rate of  $80MHz$ . It is a mode-locked Nd:Vanadate laser with a linearly polarized output centered at  $1064\text{ nm}$ . The maximum average pump power coupled through the PCF4 is  $535mW$ . A Fabry-Perot cavity is formed between the Fresnel reflection from the front cleave of the fiber and the end mirror mounted on a translation stage. We utilize the Fresnel reflection

because the system is stable and easy to align. However, this reflection is only 4%. Combining other loss and coupling efficiency, the round trip cavity loss is about 99%. The parametric gain needed to achieve threshold for oscillation should be about 100, corresponding to a nonlinear phase shift of  $\gamma P_p L \sim \pi$  [32]. The cavity length is adjusted to an optical path of 2 m, which corresponds to the repetition rate of the pump laser. A half-wave plate (HWP 1) and isolator are used for the input power control, while HWP 2 adjusts the polarization. A fiber polarization controller (FPC) is installed on the PCF in order to manage the beam polarization within the fiber, which is not polarization maintaining. By adjusting HWP 2 and the FPC one can optimize the output of the FOPO. The oscillating wavelength is tuned by rotating the end mirror where the mirror and prism combination leads to a 3-nm wide wavelength-dependent feedback. The output coupler can be either a long-pass mirror (for short wavelength output), or a short-pass mirror (for long wavelength output).

This piece of fiber (NKT Photonics; NL 5.0 1065), PCF4, has a nonlinear coefficient of  $11 (W \cdot km)^{-1}$  measured at  $1064nm$ , a mode field diameter of  $4.2 \pm 0.4 \mu m$ , and an attenuation of less than  $16dB/km$ . The group velocity dispersion, as shown in Fig. 4.2, indicates the zero group velocity dispersion wavelength is at  $1061nm$ .

$$\Delta T \approx \frac{1}{2} D \cdot \Delta \lambda \cdot L \quad (4.1)$$

where  $D$  is dispersion parameter,  $\Delta \lambda$  is the spectrum width in wavelength domain, and  $L$  is fiber length.

Figure 4.3 shows the calculated temporal walk-off between the pump and signal. For example, the wak-off is 0.8 ps at 1140 nm, which corresponds to  $\delta = 0.1$ . As the pump-to-signal wavelength spacing increases their effective interaction length decreases, thus reducing the parametric gain within the FOPO.

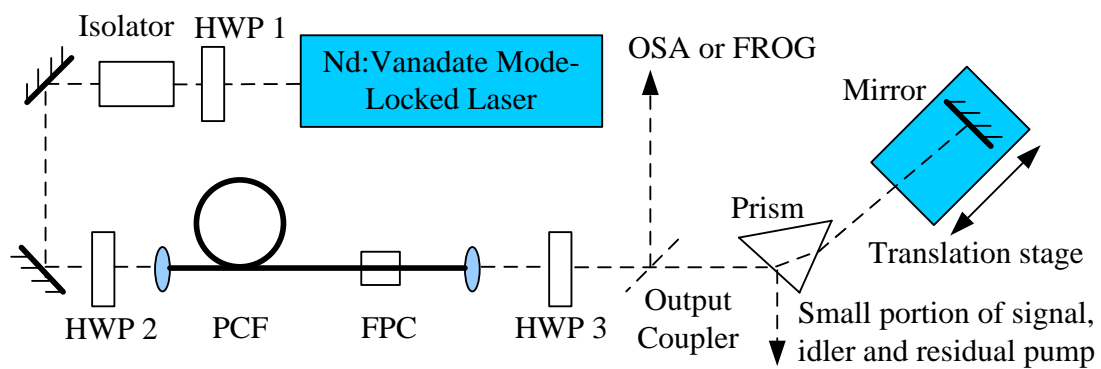


**Figure 4.1:** The setup of FOPO utilizing a 1.2m-long PCF.

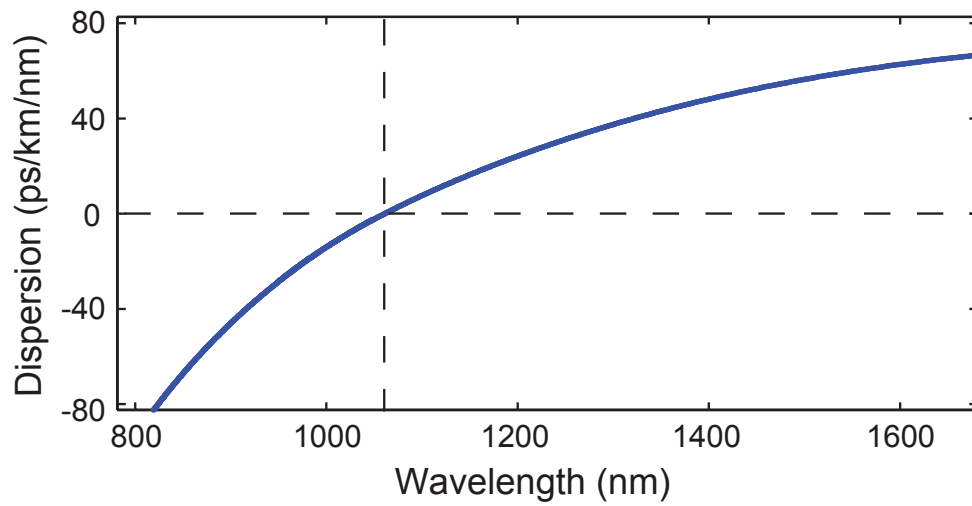


**Figure 4.2:** The group velocity dispersion of the PCF used in these experiments.

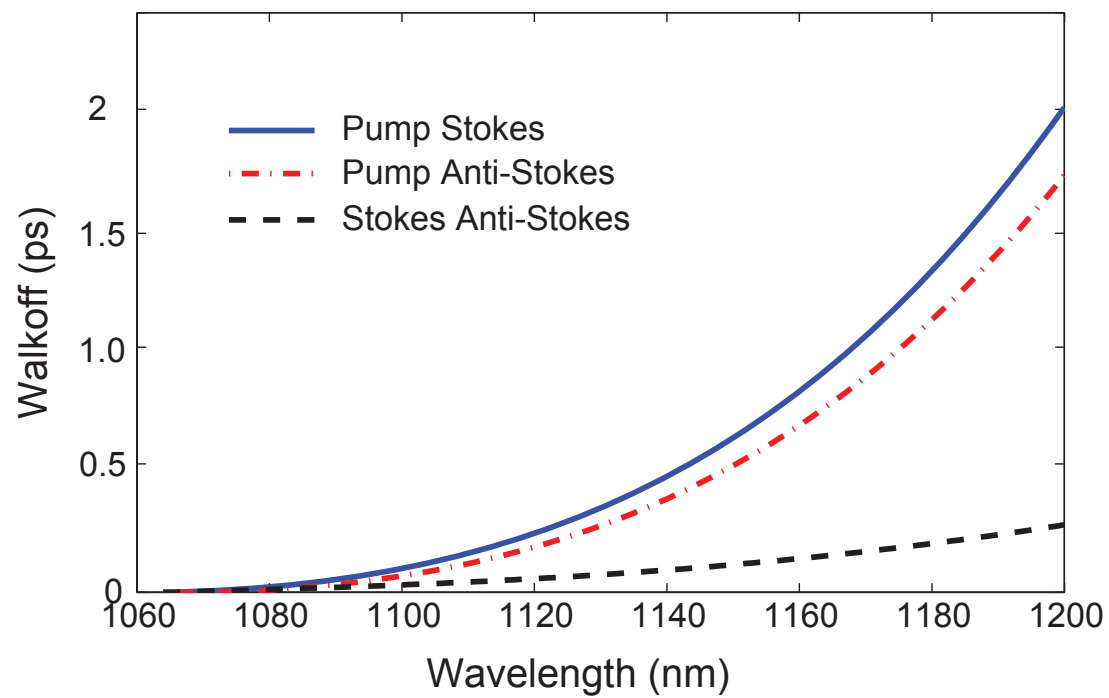


**Figure 4.3:** Calculated walk-off between pump and Stokes waves.

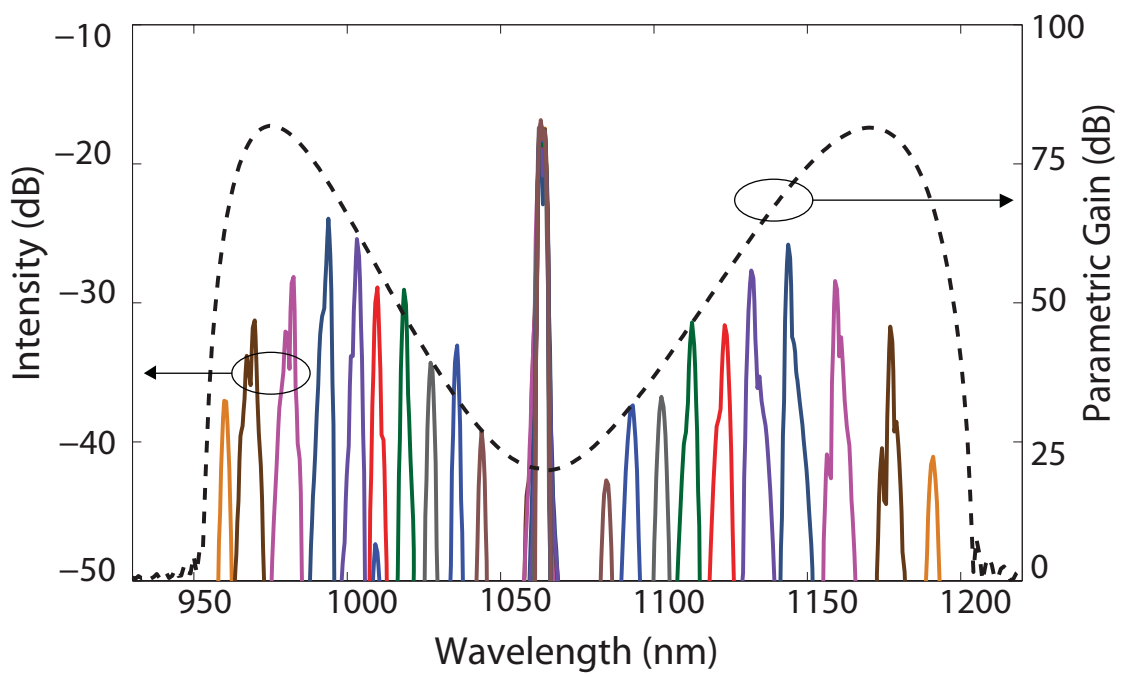
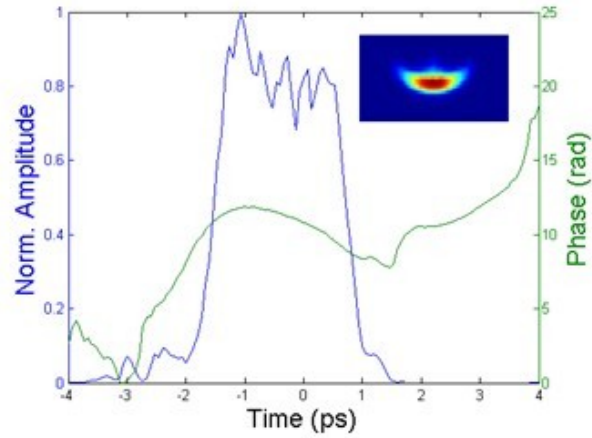


Figure 4.4: Measured spectra from the reflection of prism.



**Figure 4.5:** Retrieved output pulse from a FROG measurement .

Figure 4.4 shows the measured spectra from the reflection of the prism without an output coupler in the cavity. By adjusting the angle of end mirror and the position of the translation stage, one can select the wavelength for feedback. The tuning range is from 960 nm to 1044 nm on the anti-Stokes side and 1084 nm to 1191 nm on the Stokes side. The dashed line in Fig. 4.4 is a calculation of the parametric gain which considers phase matching, pump SPM and XPM for a continuous-wave undepleted pump [41, 52]. The wavelengths for peak operation are 990 nm and 1140 nm. The oscillation threshold is  $460 \pm 10$  mW for the peak power of pump. Shown in Fig. 4.5, a FROG measurement implies a pulse duration of 2.2 ps at 1140 nm.

Till now, we have briefly discussed the performance of FOPO in picosecond domain. Our demonstration clearly shows the feasibility of our FOPO as widely tunable light source. In next two sections, our study will focus on the output in the frequency domain and will show the experimental evidence and theoretical analysis of asymmetric spectrum with modulated peaks. This spectrum property depends on the pump power and cavity synchronization.



## 4.2 Asymmetric spectrum behavior

The high resolution spectra shown in Fig. 4.6 (a)- (c) are measured at long wavelength operation with a short pass dichroic mirror placed in the cavity as the output coupler. We gradually decrease the pump power from Fig. 4.6 (a) to (c) but fix the cavity length. The key conclusions drawn from these figures are: The spectral bandwidth of the output is determined by XPM spectral broadening. And the number of peak of the spectra is also determined by the power of the pump.

The spectral signature of XPM combined with cavity length detuning (synchronization of pump and signal pulses) is shown in Fig. 4.7 (a)- (c). The synchronization is adjusted the position of the end cavity mirror with the constant pump power. Although we will discuss the calculation of spectrum quantitatively in the next section, here we will first develop some qualitative understandings of this observation. One can simplify the performance of FOPO using a single pass optical parametric amplifier model: A weak signal is amplified by a strong pump, and meanwhile an idler is generated and amplified as well. The modulation and asymmetry are due to XPM-induced chirp combined with a delay between the pump and amplified two pulses, as shown in Fig. 4.8. Fig. 4.8 (a) - (c) are under situations with different initial pulse delay between pump and signal.

We explain the variations of spectrum as follows [63]. In the case of Fig. 4.7 (a), the signal pulse interacts mainly with the trailing edge of the pump pulse. As a result, the XPM-induced chirp is positive leading to red-shifted spectral components. Figure 4.7 (b) is a smooth spectrum. This arises from the fact that the pump pulse starts slightly behind the signal, but passes through the signal after the propagation of the fiber length. Due to the balance of interaction with the trailing edge and leading edge of the pump pulse, the spectrum of anti-Stokes wave is more like a simple peak. In the case of Fig. 4.7 (c), the pump pulse trails the signal by a larger amount than in Fig. 4.7 (b). The chirp is negative leading to blue-shifted spectral components.

In short, we find that the output of a picosecond-pumped FOPO in a low-finesse Fabry-Perot cavity exhibits a spectral width and distortion determined by XPM between the output and the pump pulses. The broadening is significant,

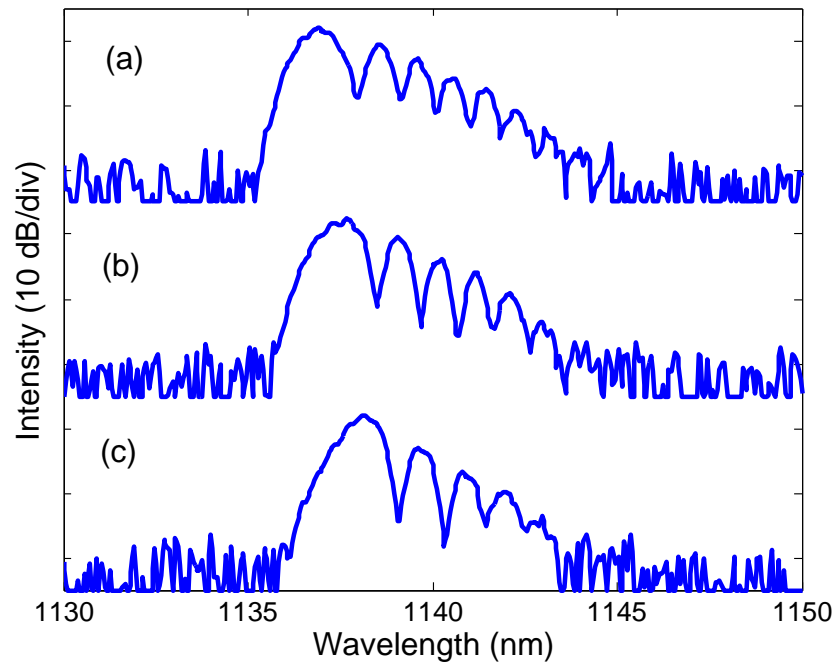


**Figure 4.6:** Measured output spectra at different pump power level. (a) Coupled pump at  $535mW$  and output at  $80mW$ . (b) Coupled pump at  $484mW$  and output at  $63mW$ . (c) Coupled pump at  $432mW$  and output at  $48mW$ .

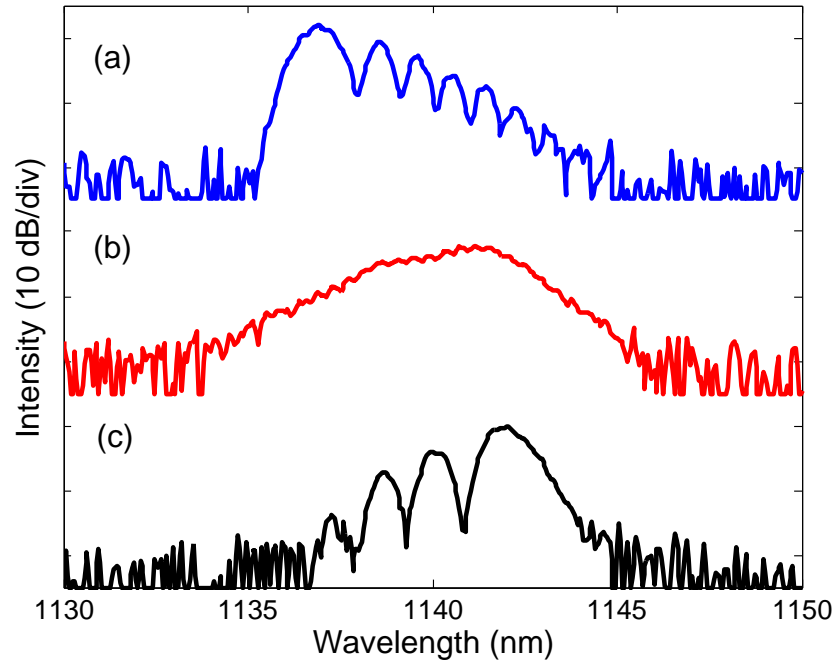


**Figure 4.7:** Measured output spectra at different cavity synchronizations (a) Maxima output power at  $80mW$ . (b) Shorten the cavity length by  $0.056cm$  to get the output power at  $60mW$ . (c) Shorten the cavity length by  $0.16cm$  to get the output power at  $45mW$ .

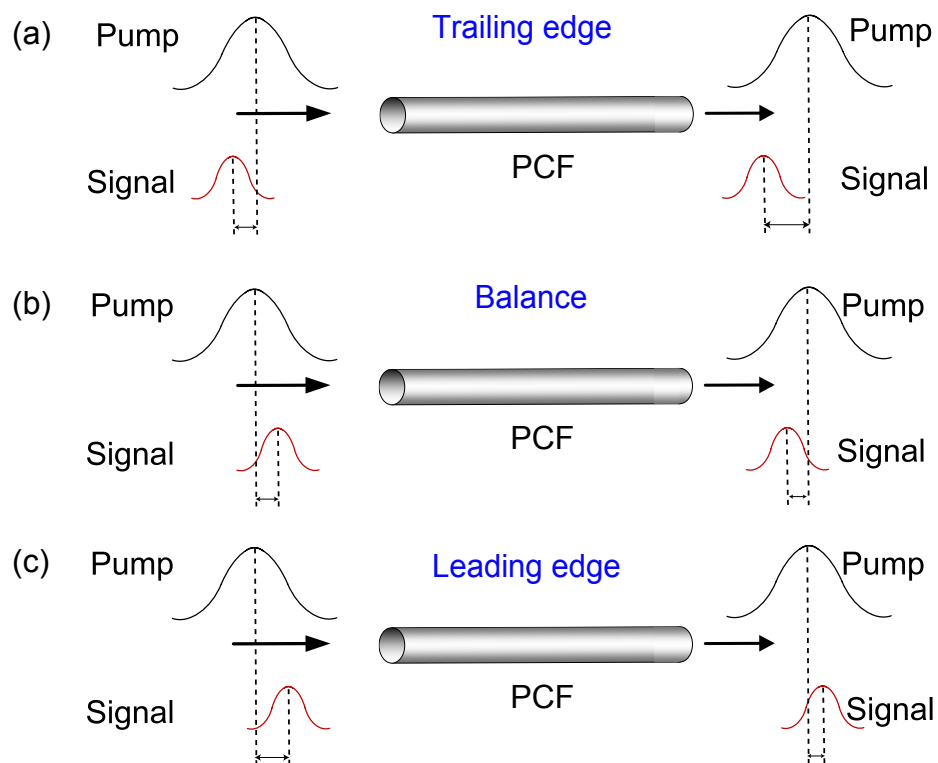


**Figure 4.8:** Single pass mode with different initial pulse delay between pump and signal.

leading to chirped pulses with time-bandwidth products greater than the factor of two. In order to use such a system in settings where a narrow spectral width is important, such as spectroscopy, one must reduce the spectral broadening. One way to achieve this is to improve the overall finesse of the cavity so that the system will operate at lower pump powers.

### 4.3 Cross-phase-modulation-induced spectral effects

Pulsed parametric amplification in fibers involves co-propagation of a strong pump pulse and one or more weak pulses. Due to the effect of XPM the spectrum of the weak pulse is influenced by the strong pump pulse. The combination of XPM and walk-off leads to a modulated and asymmetric spectrum [63, 64]. These effects have been reported previously in fiber Raman soliton lasers [64]. As shown in the previous section, we experimentally observed a similar phenomenon in optical parametric process. The generation of signal and idler pulses is due to the phase-matched FWM, stimulated by pump pulses. Although our system is an oscillator, we find that many aspects of its performance are described using a single pass of parametric amplification once operation at steady state is achieved [54]. This approximation is justified because the cavity is lossy and the output coupler is placed immediately after the beams exit the fiber. Intra-pulse dispersive broadening of the individual pump, signal and idler pulses through 1.2 m of fiber is insignificant [32]. The analysis below describes the single-pass evolution of a weak signal pulse in the presence of a strong pump pulse, including XPM and walk-off between them. We neglect small contributions from SPM of the signal and XPM arising from the idler. Therefore the time-dependent nonlinear phase shift arises only from the strong pump pulse. Despite these assumptions, our simplified theoretical analysis below still find remarkable agreement with experiments.

We begin with two pulses, pump and signal, propagating along the fiber. They are initially unchirped Gaussian shaped pulses with initial amplitudes,  $A_p(0, T) = \sqrt{P_p} e^{-\frac{(T+T_d)^2}{2T_p^2}}$  and  $A_s(0, T) = \sqrt{P_s} e^{-\frac{T^2}{2T_s^2}}$ , respectively [63]. Soliton shaped pulses

yield similar results [64]. The peak powers are given by  $P_p$  and  $P_s$  and their pulse durations are  $T_p$  and  $T_s$ .  $T$  is the time in the reference frame of the signal pulse. The initial delay between the peaks of the two pulses is given by  $T_d$ . Including walk-off and XPM, the amplitude of the signal pulse after propagating through the fiber of length  $L$  is given by  $A_s(L, T) = A_s(0, T - \Delta\beta_1 L) \exp(i\phi)$ . The resulting phase shift is

$$\phi(L, T) = 2\gamma \int_0^L |A_p(0, T + \Delta\beta_1 z)|^2 dz \quad (4.2)$$

where  $\Delta\beta_1 = \beta_1(\lambda_s) - \beta_1(\lambda_p)$  is the difference in the first order propagation coefficient of the pump and signal pulses. Equation (4.2) indicates that as the pulse propagates through the fiber its phase is modulated because of the intensity dependent refractive index, and this contribution changes along the fiber length due to group-velocity mismatch. The total contribution is [32, 63]

$$\phi = \frac{\gamma P_p L \sqrt{\pi}}{\delta} [\text{erf}(\tau + \tau_d) - \text{erf}(\tau + \tau_d - \delta)] \quad (4.3)$$

where  $\text{erf}(\tau) = \frac{2}{\sqrt{\pi}} \int_0^\tau e^{-t^2} dt$  stands for the error function,  $\tau = \frac{T}{T_p}$  is the normalized time frame,  $\tau_d = \frac{T_d}{T_p}$  is normalized delay, and  $\delta = \frac{\Delta\beta_1 L}{T_p}$  quantifies the walk-off relative to the pump pulse duration. The resulting spectrum is obtained through a Fourier transform [32]:

$$S(w) = \left| \int_{-\infty}^{\infty} A_s(0, T - \Delta\beta_1 z) \cdot e^{[i\phi(T) + i(w - w_s)T]} dT \right|^2. \quad (4.4)$$

Therefore, increasing the pump power introduces more phase modulation and generally broadens the output spectrum. Furthermore, the detailed calculation below will show that the spectrum can be asymmetric accompanied with red or blue frequency shift depending on  $\tau_d$ .

In section 4.2, we shown the measured spectra in Fig. 4.6 and 4.7. Here based on Eq. (4.4) and justified parameters, we show the calculated spectra plotted using the thin curve in Fig. 4.9. Accordingly, the thick curves are the measured output spectra of the FOPO, where the subfigures (a) - (e) are the same as Fig. 4.6

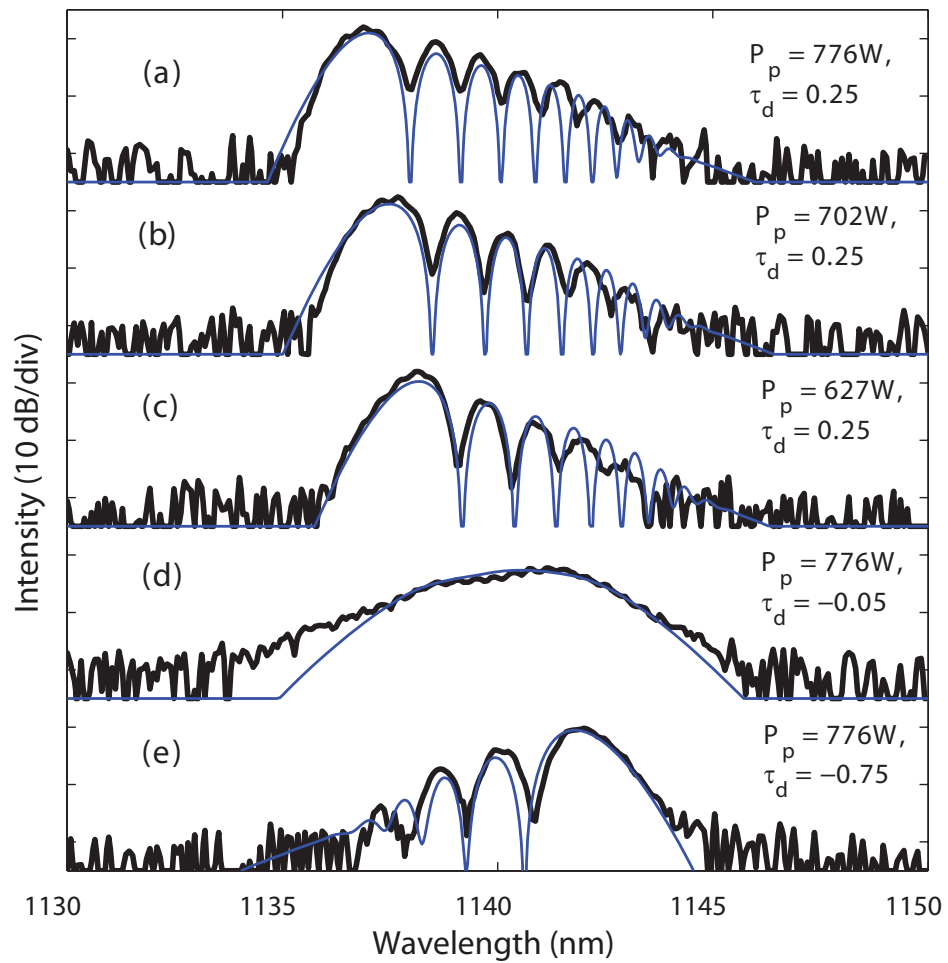


**Figure 4.9:** Spectra at different pump power and synchronization conditions: theory and experiment.

(a) (b) (c) and Fig. 4.7 (b) (c). First, let us take a look at the power dependent spectrum broadening. The synchronization is the same for Fig. 4.9 (a) (b) and (c) by fixing the cavity length and end mirror rotation. There is an asymmetric spectrum with a sequence of peaks and valleys extending towards longer wavelengths. As the pump power decreases from Fig. 4.9 (a) to (c), the spectral width narrows, the main peak moves to longer wavelengths and fewer cycles are visible.

The effect of time-dispersion tuning on the output spectrum is shown in Fig. 4.9 (a), (d) and (e). The pump power and rotational position of the end mirror are fixed but the cavity length is adjusted. The average output power is 80 mW for the case of Fig. 4.9 (a). Figure 4.9 (d) shows that after adjusting by 0.038 cm (2.4 ps round trip delay) the output spectrum becomes smooth. The average output power is 60 mW. Adjusting by another 0.089 cm (5.6 ps round trip delay) leads to asymmetric spectrum with modulations extending to short wavelengths relative to the main peak, shown in Fig. 4.9 (e). The average output power is 45 mW.

The thin curves in Fig. 4.9 are the theoretical calculations of the output spectrum using Eq. (4.4). For  $\tau_d = 0.25$ , corresponding to Fig. 4.8 (a), the signal pulse is launched behind the pump which makes it experiencing the trailing edge of pump. For the case in Fig. 4.9 (d),  $\tau_d = -0.05$ , corresponding to Fig. 4.8 (b), after one pass through the fiber, the signal pulse which was initially launched ahead of the pump pulse lags slightly behind the pump pulse at the output. As such, the signal walks through the center of the pump pulse. When  $\tau_d = -0.75$ , corresponding to Fig. 4.8 (c), the signal pulse is launched further ahead of the pump in comparison with Fig. 4.9 (d), as shown in Fig. 4.9 (e). Although it travels slowly, the signal pulse still leads the pump pulse after one pass.

By comparing Fig. 4.9 (a) (d) and (e), one can see that the spectrum is modulated and shifts towards shorter wavelength if the cavity length is adjusted to the long range of its operation. In its short range, the spectrum shifts towards longer wavelengths. Finally, in its middle range, the output spectrum becomes smooth. It is surprising that interaction with the trailing edge gives a higher output power. We believe this is due to the power-dependent phase mismatch [38].



In summary, we describe a ps-pumped FOPO which is more compact and stable compared with femtosecond systems [48, 54]. For a high power pulsed FOPO, the output spectral width is governed by XPM, pump power, and cavity synchronization. The spectrum exhibits pump power dependent broadening, and a red or blue shift depending on cavity synchronization. One can increase the spectral bandwidth for time-dispersion tuning by increasing the input pump power. This will lead to chirped output pulses with clear spectral modulation away from the center of the tuning range. Chirped pulses with a wide spectral bandwidth may be desirable if one plans to use extra pulse compressor. Alternatively, to reduce the spectral bandwidth of the output pulses one should use less pump power, for example, by reducing cavity losses. We explore the spectral effects due to cross-phase modulation and walk-off in picosecond fiber optical parametric oscillators. The output spectrum exhibits pump-power-dependent broadening, which can be quite asymmetric associated with a redshift or a blueshift depending on pump synchronization. By slightly increasing the cavity length, one obtains a blueshifted spectrum and a conversion efficiency as high as 15%.

# Chapter 5

## Theoretical analysis of fiber optical parametric processes

In chapter 3 and 4, we discussed two FOPOs which are operated in femtosecond and picosecond domain, respectively. In this chapter, we will focus on the theoretical analysis and physical dynamics in this configuration - fiber optical parametric process. First, we will model FWM at ultrafast situation, where three waves (pump, signal and idler) are all ultrashort pulses with broadband spectra rather than CW or long-pulsed situation which had been discussed in section 2.2 based on Eqs. (2.12) to (2.14). Second, we will show numerical results using justified parameters and compare with experimental data. Third, there exhibit an interesting physical phenomenon which is both experimentally and numerically observed. We call this phenomenon “spectral mirror imaging” (SMI) because two widely separated spectral sidebands can always behave as mirror images of one another with respect to the center frequency of the controlling pump beam.

### 5.1 Modeling ultrafast four-wave mixing

In chapter 3 and 4 we have discussed two FOPOs, and shown that both of their performance can be regarded as a single pass fiber optical parametric process after steady state operation. In this chapter, we will continue with this configuration but focus more on the theoretical analysis to compare with an interesting

experimental result we observed. As shown in Fig. 5.1, the key elements of this FOPO configuration are similar to the previous one we used in chapter 3 and 4, except that an extra prism is used inside the cavity. This FOPO system consists of a mode-locked laser, a piece of highly nonlinear fiber, a prism and an adjustable end mirror. The fiber is placed within an optical cavity so as to resonantly enhance a signal wave built up from noise in the presence of the strong pump wave. Since the pump is pulsed, the generated signal and idler are also pulsed and synchronous with the pump. As illustrated in Fig. 5.1 (b), a Fabry-Pérot cavity is formed between the cleave at the input end of the fiber and the end mirror. The rotatable end mirror determines the center wavelength of the resonant signal field. Neither the pump nor idler fields are resonant in the cavity. Once steady-state is achieved the signal oscillates within the cavity and is synchronous with a refreshed pump for each pass through the fiber. The nonlinear wave-mixing leads to the generation of an idler within each pass. Therefore once oscillate, each pass can be modeled as a single pass fiber optical parametric process where a portion of the output signal is fed back as the input to the next pass.

In section 2.2, the simplified analysis is based on Eqs. (2.12) to (2.14) that assume a CW or quasi-CW regime so that GVD and even higher order dispersions can be neglected. Here, to be precise, in the femtosecond or a few picosecond domain, the effects of GVD can be included by allowing  $A_j(z)$  to be a slowly varying function of time and following the analysis of section 2.1. Assuming that all three waves are polarized the same along the fiber (polarization effects are neglected), and our concern of dispersion only extend to the second-order coefficient so that the inclusion of GVD effects amounts to replacing the derivative  $dA_j/dz$  with

$$\frac{dA_j}{dz} \rightarrow \frac{\partial A_j}{\partial z} + \beta_{1j} \frac{\partial A_j}{\partial t} + \frac{i}{2} \beta_{2j} \frac{\partial^2 A_j}{\partial t^2} \quad (5.1)$$

for all three waves (i.e.,  $j = 0$  to  $2$ , for pump, signal and idler) in analogy with

Eqs. (2.12) to (2.14), as shown below [65]:

$$\frac{\partial A_0}{\partial z} - i\gamma [|A_0|^2 + 2|A_1|^2 + 2|A_2|^2] A_0 + 2i\gamma A_1 A_2 A_0^* e^{i\Delta\beta z} = 0, \quad (5.2)$$

$$\frac{\partial A_1}{\partial z} + \Delta\beta_{11} \frac{\partial A_1}{\partial T} + \frac{i}{2} \beta_{21} \frac{\partial^2 A_1}{\partial T^2} - i\gamma [|A_1|^2 + 2|A_2|^2 + 2|A_0|^2] A_1 + i\gamma A_0^2 A_2^* e^{-i\Delta\beta z} = 0, \quad (5.3)$$

$$\frac{\partial A_2}{\partial z} + \Delta\beta_{12} \frac{\partial A_2}{\partial T} + \frac{i}{2} \beta_{22} \frac{\partial^2 A_2}{\partial T^2} - i\gamma [|A_2|^2 + 2|A_1|^2 + 2|A_0|^2] A_2 + i\gamma A_0^2 A_1^* e^{-i\Delta\beta z} = 0. \quad (5.4)$$

These three coupled NLS eqs. above consider the co-propagation of three waves in the moving frame of pump pulse, where  $A_0$   $A_1$   $A_2$  represent pump, signal and idler respectively. The pump wavelength is near the ZDW of fiber ( $\beta_{20} = 0$ ),  $\gamma$  is the nonlinearity of fiber and the fiber loss is negligible. The difference in group velocity between the pump and signal pulses is defined as  $\Delta\beta_{11} = \beta_1(\omega_1) - \beta_1(\omega_0)$ , and the difference in group velocity between the pump and idler is defined as  $\Delta\beta_{12} = \beta_1(\omega_2) - \beta_1(\omega_0)$ . The GVD of signal and idler are described by  $\beta_{21}$  and  $\beta_{22}$ , while the propagation mismatch is described by  $\Delta\beta = \beta(\omega_1) + \beta(\omega_2) - 2\beta(\omega_0)$ .

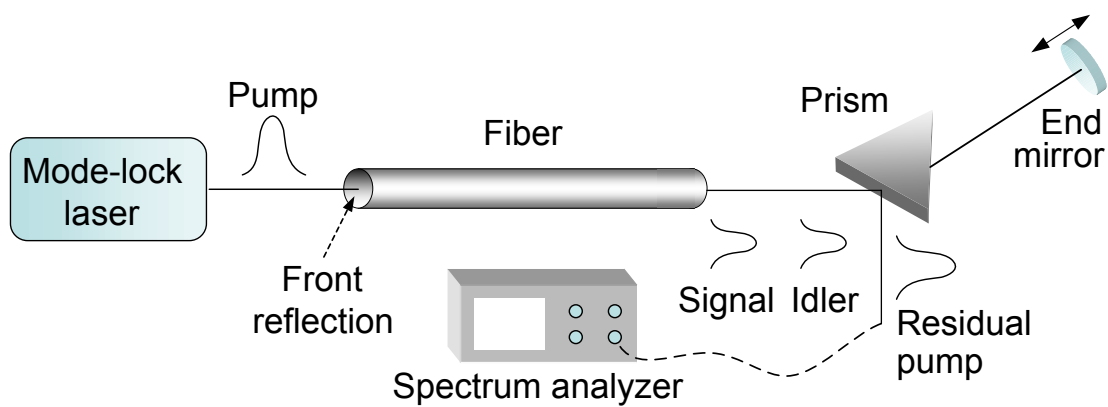


**Figure 5.1:** Schematic of a generalized FOPO for both femtosecond and picosecond operation.

In Eqs. (5.3) and (5.4) for the signal and idler, the second term represents walk-off and the fourth term represents self-phase modulation and cross-phase modulation. Their combined contributions, nonlinear phase shift as a function of walk-off, lead to an asymmetric multiple-peaked spectrum [66]. We will show later that the third term, representing GVD of pulses, and the last term, representing parametric gain, are responsible for SMI.

The resulting three coupled NLS equations (5.2) - (5.4) describe FWM of ultrashort optical pulses and include the effects of GVD, SPM, and XPM. It is generally difficult to solve the coupled NLS equations analytically, therefore numerical approaches are usually used in practice. Furthermore, as the group velocity of three pulses participating in the FWM process can be quite different, efficient FWM requires not only phase matching but also matching of the group velocities. Our simulations on the performance of FOPO are based on the three coupled nonlinear Schrödinger Eqs. (5.3) and (5.4). We start with a transform-limited pump pulse and a chirped signal pulse as the input where the initial delay between the pump and signal,  $\tau$ , can vary. The signal pulse is ahead of the pump pulse if  $\tau < 0$ . Adding chirp to the input signal pulse is necessary as a result of the prism inside the cavity as shown in Fig. 5.1. For the femtosecond case, the pump pulse is an unchirped Gaussian shape having a pulse duration of 400 fs and a peak power of 30 kW. The input signal pulse is a chirped hyperbolic secant shape with a pulse duration of 80 fs and peak power of 10 W. For the picosecond case, the pump pulse is an unchirped Gaussian shape having a pulse duration of 8 ps and a peak power of 780 W. The input signal pulse is a chirped hyperbolic secant shape with a pulse duration of 2 ps and peak power of 5 W. Based on these parameters, our simulations show a notable symmetric feature between two spectral sidebands. Simulation results of two sideband spectrograms, i.e. spectra as a function of the initial delay, are shown in Fig. 5.2 and 5.3.

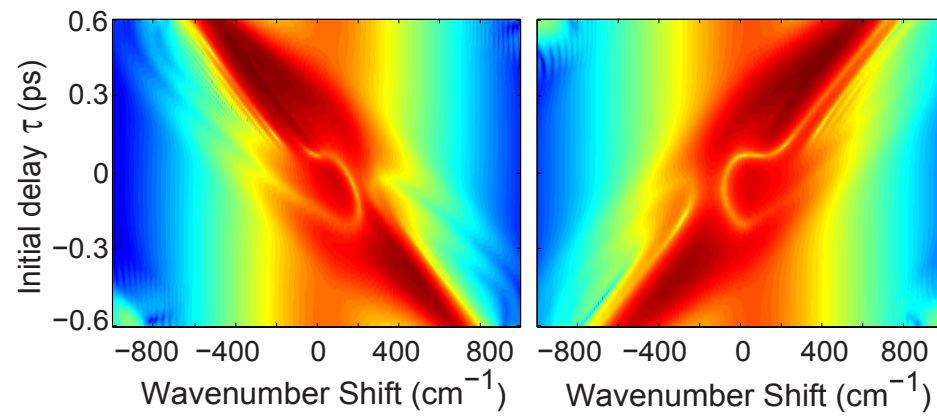


**Figure 5.2:** Simulations of two sideband spectrograms in femtosecond domain.

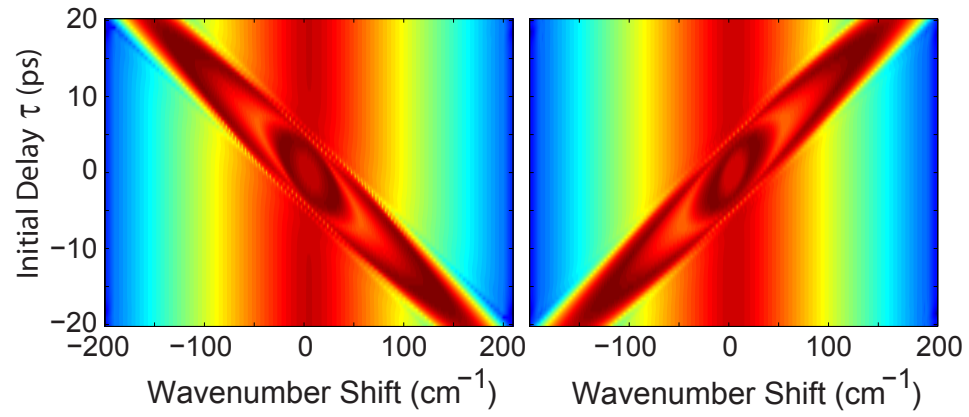


**Figure 5.3:** Simulations of two sideband spectrograms in picosecond domain.



## 5.2 Simulation and experimental results

To compare with the simulations in section 5.1, we use two setups incorporating different pump lasers and fibers whose ZDWs match the pump wavelength. The femtosecond FOPO is pumped by a mode-locked Yb-doped fiber laser which delivers a pulse duration of 400 fs with a repetition rate of 50 MHz. It is linearly polarized with center wavelength at 1032 nm. The average pump power launched into the fiber is 620 mW. In the femtosecond case, the fiber is 3 cm long with a ZDW at 1030 nm. For other parameters of fiber, please refer to chapter 3 and Ref. [54]. The picosecond FOPO is pumped by a mode-locked Nd:Vanadate laser which delivers transform-limited 8 ps pulses at a repetition rate of 80 MHz. It is linearly polarized with center wavelength at 1064 nm. The average pump power coupled into the fiber is 525 mW. In the picosecond case, the fiber is 1.2 m long with ZDW at 1061 nm. For other parameters of fiber, please refer to chapter 4 and Ref. [66].

The spectra plotted in Fig. 5.4 (a) are for the output of the femtosecond system where traces 1, 2, and 3 correspond to three different end mirror translation settings. Trace 1 is obtained when the FOPO is operated at its highest output power. We acquire trace 2 and trace 3 by reducing 15  $\mu\text{m}$  and 30  $\mu\text{m}$  of cavity length (corresponding to 0.1 ps and 0.2 ps round-trip delay), respectively. In these three traces one observes two distinct sidebands located at about  $7880\text{ cm}^{-1}$  and  $11500\text{ cm}^{-1}$  which are equally spaced from the pump at  $9690\text{ cm}^{-1}$ . For trace 1 each sideband includes three peaks. As the cavity length becomes shorter, in trace 2 each sideband has two peaks. Finally, for trace 3 there is only one peak on each sideband. In all cases, the two sidebands behave as mirror images of one another illustrating the SMI features. Simulations for the femtosecond case, shown in Fig. 5.4 (b), support our experimental observations.

Figure 5.5 (a) shows the experimental observations of SMI for the picosecond system. Two distinct sidebands, located at about  $8750\text{ cm}^{-1}$  and  $10050\text{ cm}^{-1}$ , are equally separated from the pump at  $9400\text{ cm}^{-1}$ . Trace 1 in Fig. 5.5 (a) shows the expected sidebands on either side of the pump spectrum. The signal exhibits a blue shift with four decaying peaks, while the idler features the mirror image- a red

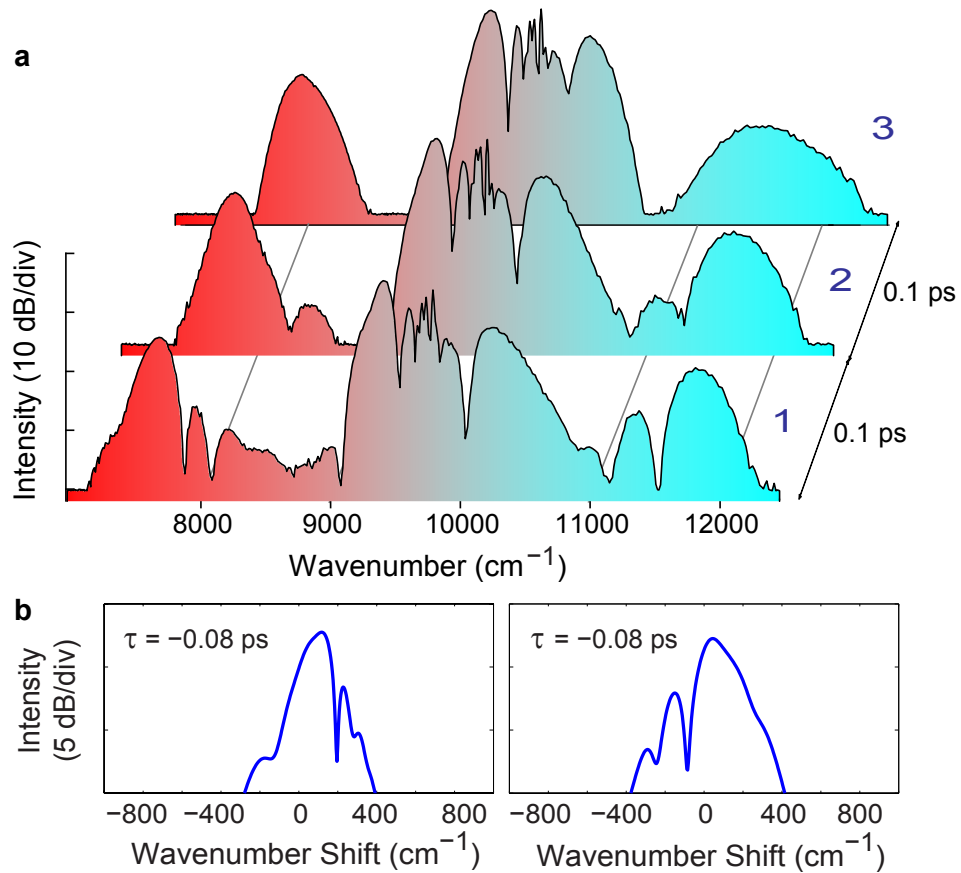


**Figure 5.4:** Demonstration of SMI in the femtosecond domain. (a) Measured output spectrum from the femtosecond FOPO. From trace 1 to trace 3 one reduces the round-trip delay by 0.1 ps per step. From left to right, the broadband spectra for each trace includes a signal sideband, a residual pump and an idler sideband. (b) Simulations of two spectral sidebands in the presence of a femtosecond pump pulse where  $\tau$  is an initial delay between the pump and signal. The resulting spectra at  $\tau = -80$  fs resemble the experimental measurement in trace 1.

shift with four decaying peaks. Trace 2 in Fig. 5.5 (a) is obtained by increasing the cavity length by 1.25 mm (8.3 ps round-trip delay). In this case the signal exhibits a red shift with five peaks, while idler exhibits the mirror image- a blue shift with five peaks. Simulations for the picosecond case are shown in Fig. 5.5 (b).

### 5.3 Further discussions

An interesting insight from our simulation is that for the picosecond case as shown in Fig. 5.5 (b), the spectrogram of each sideband exhibits the “180 degree rotational symmetry”. This indicates that by adjusting the delay, one can obtain a blue-shifted peak with a tail extending towards the red, or a red-shifted peak with a tail extending towards the blue. We acquire this experimentally as well (see two traces in Fig. 5.5 (a)). This symmetry feature is less pronounced in the femtosecond case shown in Fig. 5.4 (b) where only a red-shifted tail is observable. The difference rises from GVD-induced pulse broadening. Pulse broadening is much smaller for the picosecond case (2% pulse broadening in 1.2 m of fibre) [66] than the femtosecond case (25% pulse broadening in 3 cm of fibre) [54].

Our study also provides insight into optimization of the time-dispersion tuning of fibre optical parametric processes. Figure 5.5 (b) shows that one can shift the wavelength of output signal by adjusting the initial delay between the pump and signal. Based on an 8-ps pump pulse, our simulation predicts that more than 100 nm of tunability is possible for a single pass fibre optical parametric process. This is much bigger than the previous result of 0.25 nm which relied exclusively on a cross-phase modulation induced shift [67]. The potential increase in tunability occurs because in our case the wavelength difference between the pump and signal pulse is relatively small leading to a large interaction length. Experimentally we have not found such large frequency shifts. The reason is the limited range of temporal delay settings over which the FOPO will oscillate. Near the edge of this range, the pulse energy of input signal (the feedback from the output of fibre optical parametric process) are much lower than in the center. The simulations, on the other hand, rely on a single pass process with the fixed energy

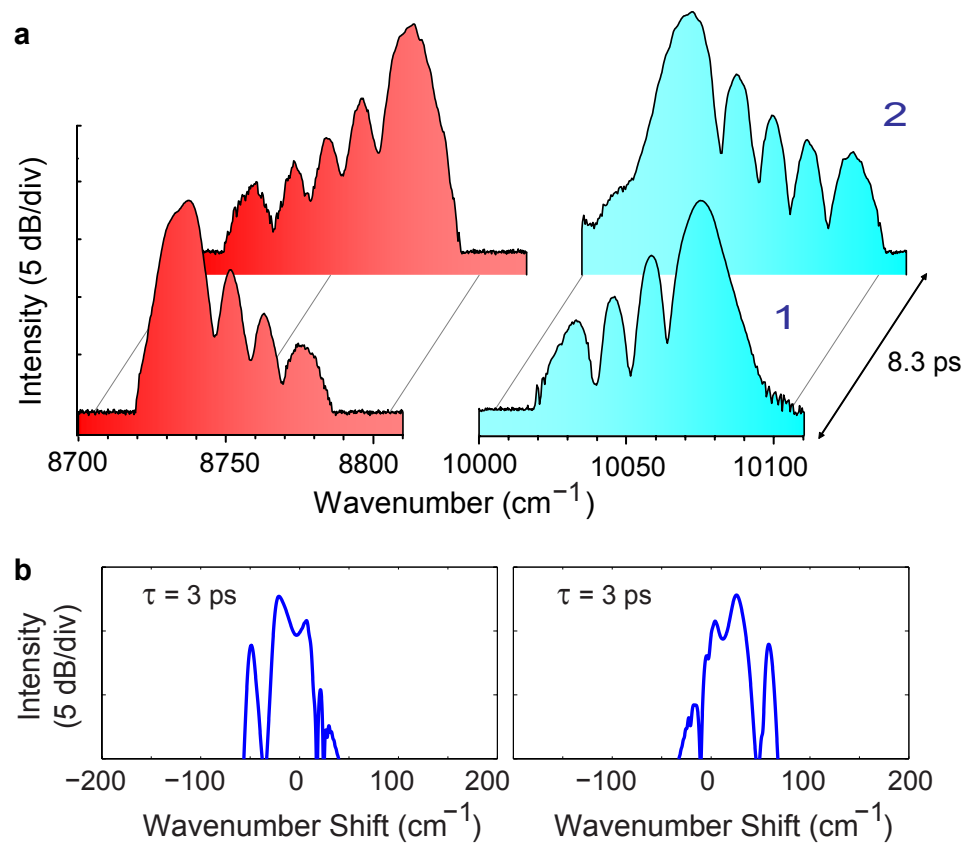


**Figure 5.5:** Demonstration of SMI in the picosecond domain. (a) Measured output spectrum from the picosecond FOPO. From trace 1 to trace 2 one reduces the round-trip delay by 8.3 ps. (b) Simulations of two spectral sidebands in the presence of a picosecond pump pulse where  $\tau$  is an initial delay between the pump and signal. The signal is the left trace and the idler is the right trace. The resulting spectra at  $\tau=3$  ps resemble the experimental measurement in trace 1.

at the input end regardless of the delay setting.

Our experimental observations shown in Fig. 5.4 (a) and simulations shown in Fig. 5.2, indicate the signal has a narrower spectral width than the idler for the femtosecond case. This is because the frequency difference between the pump and signal,  $\Delta\omega$ , is quite large ( $1700 \text{ cm}^{-1}$ ). The GVD curve for the fibre is no longer in the linear region which invalidates the assumption of  $\beta_{21} = -\beta_{22} = \beta_2$ , leading to  $|\beta_{21}| < |\beta_{22}|$ . We will show in section 6.2 that this relation, the opposite vale of GVD, is one of key physical mechanisms of SMI. Since the magnitude of GVD for the signal is smaller than idler, the signal will introduce less chirp during its dispersive propagation. For the picosecond case as shown in Fig. 5.5 (a) and 5.3, the signal and idler have nearly the same spectral width because  $\Delta\omega$  is much smaller ( $650 \text{ cm}^{-1}$ ) and the assumption of a linear GVD curve is justified.

The agreement between simulation and experiment is good for the femtosecond case (see Fig. 5.4 (a) and Fig. 5.2). However, for the picosecond case simulations of spectra shown in Fig. 5.3 do not reveal the same sequence of decaying peaks for trace 1 in Fig. 5.5 (a). This discrepancy arises from using a single-peaked spectrum as the input signal pulse. This choice is justified for the femtosecond case because the output spectrum is wide and the prism filtering effect within the FOPO leads to a relatively narrow feedback on the order of 2 nm [66]. As such, only a single spectral peak is resonating. However, for picosecond case the feedback spectral width is comparable to the whole multiple-peaked spectrum. One can retrieve simulation results comparable to the experimental results by using a chirped pulse with specified multiple-peaked spectrum as the input signal.

We have not included third or other higher order dispersion, self-steepening, and intra-pulse Raman scattering [32] within our simulation. Nevertheless, the simulations replicate the key elements of the experiments in both femtosecond and picosecond cases.

# Chapter 6

## Spectrum reversal and temporal phase conjugation

In chapter 5, our simulation verified a tunable spectrum reversal which we experimentally observed. In this chapter, besides numerical calculations, to elucidate the principles of SMI we will theoretically explore the physical mechanisms.

To begin with, we discuss a similar reversal behavior in the time domain which has already been revealed as spatial phase conjugation of counterpropagating optical beams.

Then, concerning our spectral reversal a simple analytical expression for the coupled governing equations of two sideband spectra is obtained, which reveals that the opposite values of group-velocity dispersion and the complex-conjugated parametric gain are the physical mechanisms responsible for this phenomenon.

As an analogy to the time reversal via spatial phase conjugation of counterpropagating optical beams, here we demonstrate a tunable non-degenerate spectrum reversal technique based on temporal phase conjugation of co-propagating ultrashort pulses. This spectral imaging technique is a spectral realization of phase conjugation, and provides a new measurable connection between the temporal and spectral properties of correlated fields.

Our exploration of SMI, while fundamentally interesting and important, also has enormous potential for applicability. For examples, these “spectral mirrors”, when combined with “time lenses”, will complete a set of optical components

for manipulating temporal and spectral information in ways analogous to traditional imaging. We anticipate these fundamental interests to be the starting point for advancements in diverse applications.

## 6.1 Introduction to phase conjugation and time reversal

Here we will first give an introduction to optical phase conjugation, which generally refers to spatial phase conjugation of counterpropagating optical beams. Before we go to the theoretical detail of optical phase conjugation, in order to better understand the concept, let us first take a look at an example of its application: this process can be used to remove the effects of aberrations from certain types of optical systems [68, 69, 70, 71]. The key elements of this process is shown in Fig. 6.1 (a), showing an optical wave which incidents onto a normal mirror. We see that the advanced portion of the incident wavefront remains the same after reflection. As a comparison, Fig. 6.1 (b) shows the same wavefront falling onto a phase-conjugate mirror (PCM). In this case the advanced portion turns into the retarded portion in the reflection process. Note that the generated wavefront exactly replicates the incident wavefront but propagates in the opposite direction. For this reason, optical phase conjugation is sometimes referred to as the generation of a time-reversed wavefront.

Let us take a detailed look at the physics of this incident wavefront reversal process as illustrated in Fig. 6.1 (b). The reason why it is also named as phase conjugation can be understood by introducing a mathematical description as follows. The incident wave that hits on the PCM can be written as

$$\tilde{\mathbf{E}}_1(\mathbf{r}, t) = \mathbf{E}_1(\mathbf{r})e^{-i\omega t} + c.c., \quad (6.1)$$

On the other hand, illuminating by such a wave, the PCM produces a reflected wave, called the phase-conjugate wave, described by

$$\tilde{\mathbf{E}}_2(\mathbf{r}, t) = r\mathbf{E}_1^*(\mathbf{r})e^{-i\omega t} + c.c., \quad (6.2)$$

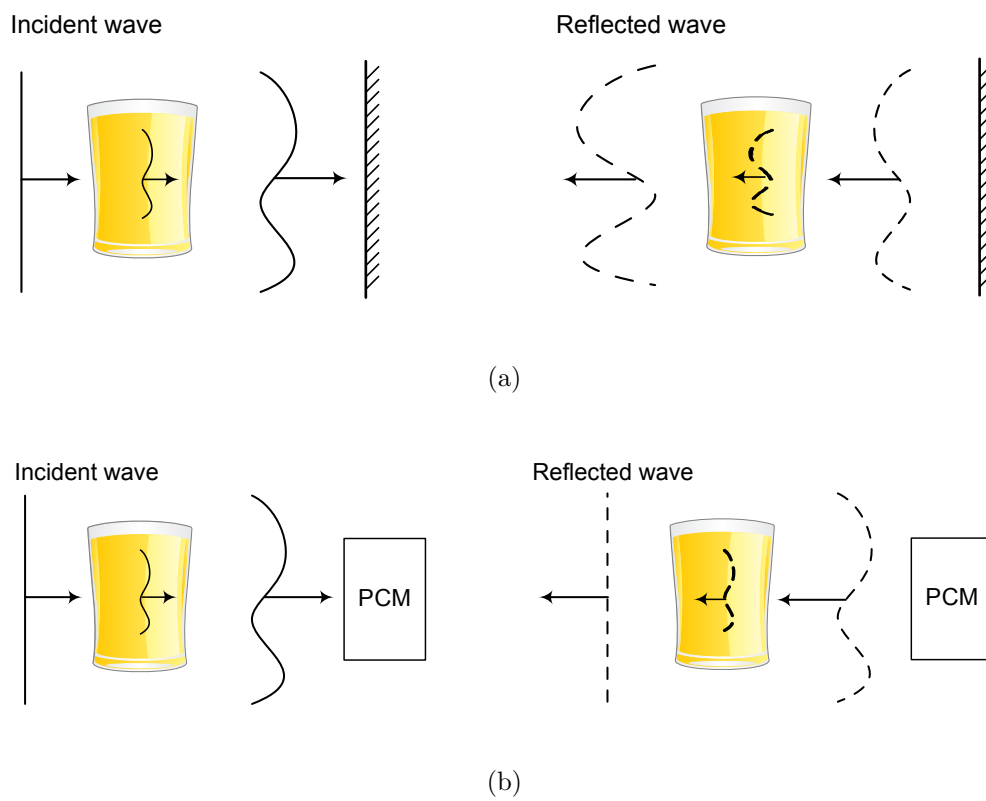


**Figure 6.1:** Reflections (a) an ordinary mirror and (b) a phase-conjugate mirror.



where  $r$  is a real constant representing the amplitude reflection coefficient of the PCM. Furthermore, since  $\mathbf{E}_1(\mathbf{r})$  is a vector function, we can represent it as the product as below:

$$\mathbf{E}_1(\mathbf{r}) = \hat{\epsilon}_1 A_1(\mathbf{r}) e^{i\mathbf{k}_1 \cdot \mathbf{r}}, \quad (6.3)$$

where the polarization unit vector is  $\hat{\epsilon}_1$ , the slowly varying field amplitude is  $A_1(\mathbf{r})$ , and the wavevector of the incident light is  $\mathbf{k}_1$ . Accordingly, the complex conjugate of Eq. (6.3) is given explicitly by

$$\mathbf{E}_1^*(\mathbf{r}) = \hat{\epsilon}_1^* A_1^*(\mathbf{r}) e^{-i\mathbf{k}_1 \cdot \mathbf{r}}, \quad (6.4)$$

From this expression above, we can identify that the action of a PCM has two important properties: First, by replacing  $A_1(\mathbf{r})$  with  $A_1^*(\mathbf{r})$ , Eq. (6.2) implies the reversal of wavefront as illustrated in Fig. 6.1 (b). Second, by comparing Eq. (6.3) with Eq. (6.4), one can identify that  $\mathbf{k}_1$  is replaced by  $-\mathbf{k}_1$ , showing that the incident wave is reflected back into its direction of incidence. This result means that each ray of the incident beam is precisely reflected back onto itself.

By combining Eq. (6.1) and Eq. (6.2), one can easily identify the important relation:

$$\tilde{\mathbf{E}}_2(\mathbf{r}, t) = r \tilde{\mathbf{E}}_1(\mathbf{r}, -t). \quad (6.5)$$

This result shows that the phase conjugation process can be regarded as the generation of a time-reversed wavefront.

Let us now consider a physical process that performs the function of PCM. Pioneered by Prof. Yariv, the phase conjugate of an incident wave can be created by the process of degenerate FWM using the geometry shown in Fig. 6.2 [70]. This process is degenerate in the sense that all the four interacting waves have the same frequency. In this process, a lossless nonlinear medium characterized by a third-order nonlinear susceptibility,  $\chi^{(3)}$ , is illuminated by two strong counterpropagating pump waves  $E_1$  and  $E_2$  and an additional signal wave  $E_3$ . The pump waves are usually taken to be plane waves<sup>1</sup>. The signal wave can be an arbitrary wavefront. Later we will show that, as a result of the nonlinear coupling between these waves, a new wave  $E_4$  is created that is the phase conjugate of  $E_3$ .

---

<sup>1</sup>In principle, they can possess any wavefront structure as long as their amplitudes are complex conjugates of one another [72]

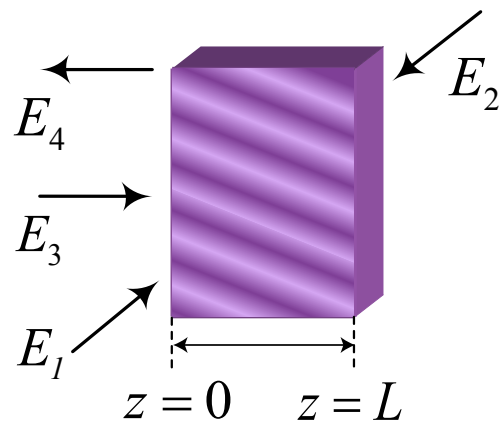


**Figure 6.2:** Geometry of phase conjugation by degenerate four-wave mixing.

First, the electric field of four interacting waves can be represented as

$$\begin{aligned}\tilde{E}_i(\mathbf{r}, t) &= E_i(\mathbf{r})e^{-i\omega t} + c.c. \\ &= A_i(\mathbf{r})E^{i(\mathbf{k}_i \cdot \mathbf{r} - \omega t)} + c.c.\end{aligned}\quad (6.6)$$

for  $i = 1, 2, 3, 4$ . The nonlinear polarization produced within the medium by the three input waves will have, a term of the form [72]

$$\begin{aligned}P_{NL} &= 6\epsilon_0\chi^{(3)}E_1E_2E_3^* = 6\epsilon_0\chi^{(3)}A_1A_2A_3^*e^{i(\mathbf{k}_1+\mathbf{k}_2-\mathbf{k}_3)\cdot\mathbf{r}} \\ &= 6\epsilon_0\chi^{(3)}A_1A_2A_3^*e^{-i\mathbf{k}_3\cdot\mathbf{r}}\end{aligned}\quad (6.7)$$

Here the simplification is based on the assumption that the wavevectors of counterpropagating the pump waves  $E_1$  and  $E_2$  are related by  $\mathbf{k}_1 + \mathbf{k}_2 = 0$ . From the expression above, we see that the contribution to the nonlinear polarization has a spatial dependence that allows it to act as an automatically phase-matched source term for a conjugate wave,  $E_4$ , with the wavevector  $\mathbf{k}_3$ . Thus, the wavevectors of the signal and conjugate waves are related by  $\mathbf{k}_3 = -\mathbf{k}_4$ . Furthermore, this expression also implies that the field amplitude of the wave generated by the nonlinear polarization will be proportional to  $A_1A_2A_3^*$ . This wave,  $A_4$ , will be the phase conjugate of  $A_3$  whenever the phase of the product  $A_1A_2$  is spatially invariant<sup>2</sup>.

We can also understand this process, the generation of conjugated wave, from the following point of view. The incoming signal wave of amplitude  $A_3$  interferes with one of the pump waves, say  $A_1$ , to form a spatially varying intensity distribution. As a consequence of the nonlinear response of the medium, a refractive index variation accompanies this interference pattern. This variation acts as a volume diffraction grating, which scatters the other pump wave, say  $A_2$ , to form the outgoing conjugate wave of amplitude  $A_4$ .

Assuming that the fields  $E_3$  and  $E_4$  are much weaker than the pump fields  $E_1$  and  $E_2$ , the governing eqs. for two pump waves can be obtained as [72],

$$\frac{dA_1}{dz'} = \frac{3i\omega}{2nc}\chi^{(3)}[|A_1|^2 + 2|A_2|^2]A_1 \equiv i\kappa_1A_1. \quad (6.8)$$

---

<sup>2</sup>This can be understood by the assumption of plane waves we previously made. Both  $A_1$  and  $A_2$  represent plane waves. Or if,  $A_1$  and  $A_2$  are phase conjugates of one another, then  $A_1A_2$  will be proportional to the real quantity  $|A_1|^2$ .

$$\frac{dA_2}{dz'} = \frac{-3i\omega}{2nc} \chi^{(3)} [ |A_2|^2 + 2|A_1|^2 ] A_2 \equiv i\kappa_2 A_2. \quad (6.9)$$

Furthermore, if the two pump beams have equal intensities so that  $\kappa_1 = \kappa_2 = \kappa$ , the product  $A_1 A_2$  becomes spatially invariant, so that  $A_1(z') A_2(z') = A_1(0) A_2(0)$ .

$$\frac{dA_3}{dz} = \frac{3i\omega}{nc} \chi^{(3)} [ (|A_1|^2 + 2|A_2|^2) A_3 + A_1 A_2 A_4^* ]. \quad (6.10)$$

$$\frac{dA_4}{dz} = \frac{-3i\omega}{nc} \chi^{(3)} [ (|A_1|^2 + 2|A_2|^2) A_4 + A_1 A_2 A_3^* ]. \quad (6.11)$$

By defining  $A_3 = A'_3 e^{i\kappa_3 z}$ , and  $A_4 = A'_4 e^{-i\kappa_3 z}$ , where  $\kappa_3 = \frac{3\omega}{nc} \chi^{(3)} (|A_1|^2 + |A_2|^2)$ , we can simplified the coupled equations above as

$$\frac{dA'_3}{dz} = i\kappa A'_4, \quad (6.12)$$

$$\frac{dA'_4}{dz} = -i\kappa_3 A'_3. \quad (6.13)$$

From these two coupled Eqs. above, we can easily identify the reason for the phase conjugation via degenerate FWM: The generated field  $A'_4$  is driven only by the complex conjugate of the input field amplitude  $A'_3$ . It is interesting that the transformation we made by defining  $A'_3$  and  $A'_4$  is equivalent to remove the energy from two pump waves [72].

In order to obtain the analytic solution of Eqs. (6.12) and (6.13), let us consider the practical situation for the initial conditions of optical phase conjugation via FWM. Usually there is no conjugate wave initially injected into the medium at  $z = L$ , i.e.,  $A'_4(L) = 0$ . Therefore, the solution of two interacting fields amplitudes are then given by [73]

$$A'_3(L) = \frac{A'_3(0)}{\cos |\kappa| L}, \quad (6.14)$$

$$A'_4(0) = \frac{i\kappa}{|\kappa|} (\tan |\kappa| L) A'_3(0). \quad (6.15)$$

From the expressions above, we can have two interesting conclusions: First, note that the transmitted signal wave  $A'_3(L)$  is always stronger than the incident wave  $A'_3(0)$ . Second, depending on the value of  $|\kappa|L$ , the output conjugate wave

$A_4(0)$  can be infinity. This means the reflectivity of PCM based on degenerate FWM can exceed 100% as this “mirror” is supplied by the energy from the pump waves.

## 6.2 Concept of spectral mirror imaging and analytic theory

In section 5.2, both our simulations and experiments captured the symmetric properties of two sideband spectra. In this section, we will discuss the physics of this interesting notable phenomenon. Not just limited to SMI that one can see visually on optical spectrum analyzer, but we will also introduce another related concept called “temporal phase conjugation” (TPC) which is difficult to capture directly in the time domain. Figure 6.3 illustrate the relationship between SMI and TPC. After passing through an SMI system, the electric fields of two co-propagating optical pulses ( $k = 1, 2$ ) are given by

$$E_k(t) = A_k(t) \cdot e^{-i\omega_k t} \quad (6.16)$$

where  $A_k(t)$  are the slowly-varying complex envelopes independent of the rapidly varying carrier waves  $e^{-i\omega_k t}$ . In the frequency domain, the spectra of these two pulses are given by the Fourier transform

$$\mathcal{F}\{A_k(t)\} = \tilde{A}_k(\omega) = \tilde{E}_k(\omega + \omega_k) \quad (6.17)$$

where  $\tilde{A}_k(\omega)$  represent the spectra of each pulse centered on its own reference frame. Spectral mirror imaging implies that the spectral amplitudes are reversed relative to one another, i.e.,

$$|\tilde{A}_2(\omega)| = |\tilde{A}_1(-\omega)|. \quad (6.18)$$

Since the carrier frequencies of the two waves are often different, these two spectra are distributed as mirror images of one another with respect to the mean of two carrier frequencies, i.e.  $(\omega_1 + \omega_2)/2$ . We refer to the *signal* as the long-wavelength sideband and the *idler* as the short-wavelength sideband.

In comparison, TPC implies that the temporal phase profiles of two pulses are inverted, i.e.,

$$\arg\{A_2(t)\} = \varphi_0 - \arg\{A_1(t)\}, \quad (6.19)$$

where  $\varphi_0$  is a constant arbitrary absolute phase. Furthermore, if the amplitudes of two pulses equal, their complex envelopes are related as

$$A_2(t) = A_1^*(t) \cdot e^{i\varphi_0}. \quad (6.20)$$

The relationship between SMI and TPC follows from the Fourier transform:

$$\tilde{A}_2(\omega) = \mathcal{F}[A_2(t)] = \mathcal{F}[A_1^*(t) \cdot e^{i\varphi_0}] = \tilde{A}_1^*(-\omega)e^{i\varphi_0}. \quad (6.21)$$

Therefore SMI is a spectral realization of TPC. To fully characterize the ultrashort pulses in the time domain is difficult. Alternatively, it is convenient to capture the spectral amplitudes in the frequency domain as such pulses carry broad spectra.

The overall concept is similar to low sideband modulation in communications and signal processing, where the generated spectrum is inverted with respect to the baseband spectrum. This concept also resembles radio frequency conversion mixing, where an inverted spectrum is achieved by using high-side local oscillation injection [74]. In the optical frequency regime, our demonstration of SMI involves a nonlinear-optical medium with an instantaneous response and nonlinear wave-mixing [72]. In particular, using nonlinear optical fibers [52], the third-order nonlinearity based optical parametric process can be modeled as the interaction among three waves (pump, signal and idler) by three coupled nonlinear Schrödinger equations [32], as shown in Eq. (5.2) to (5.4). In a suitable operational regime, we can obtain the simplified governing equations for the signal  $\mathcal{A}_1$  and idler  $\mathcal{A}_2$ . Suppose the long-pulsed pump is undepleted and the phase-matching condition ( $\Delta\beta + 2\gamma P_0 z = 0$  where  $P_0 = |A_0|^2$  is the peak power of pump coupled into the fiber) is met [32], Eqs. (5.2) - (5.4) can be simplified to two governing equations for the signal and idler. If the wavelength shift between two sidebands is small, the variation of GVD is approximately linear as a function of wavelength within this region. Furthermore, as we set the pump wavelength close to the ZDW of fiber, the magnitudes of the GVD for signal and idler are approximately the same but

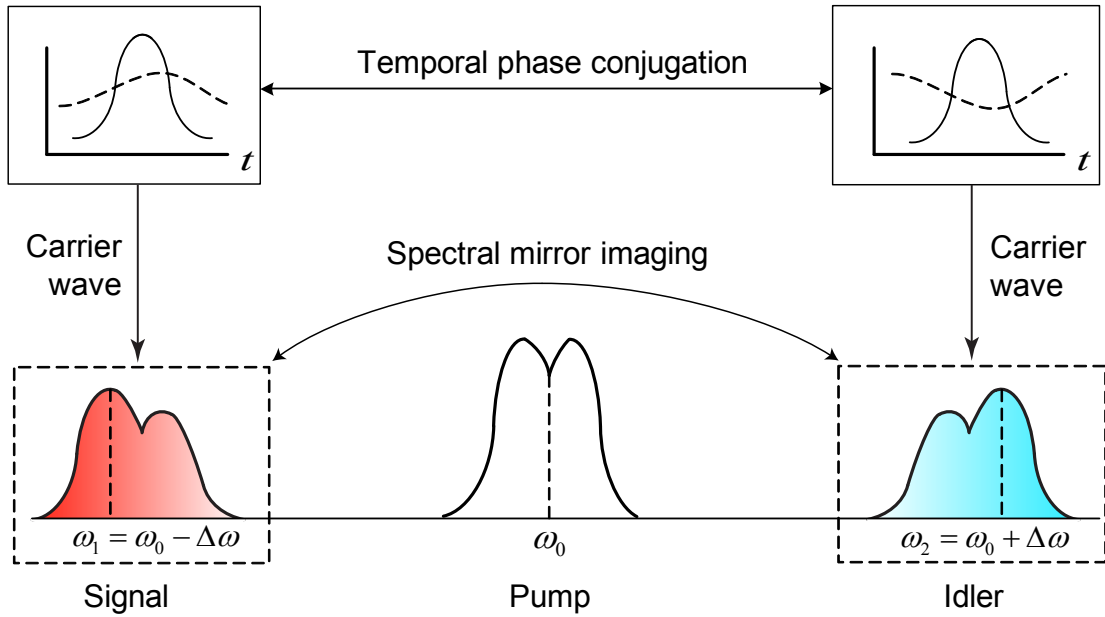


**Figure 6.3:** The concept of SMI. Two pulses, signal and idler, are depicted at the top left and right respectively, where the solid lines are the temporal amplitudes  $|A_{1,2}(t)|$  and dashed lines are the temporal phase profiles  $\arg\{A_{1,2}(t)\}$ . Their spectral amplitudes  $|\tilde{A}_{1,2}(\omega)|$  are depicted at the bottom left and right with different center frequencies  $\omega_{1,2}$ . The demonstration of SMI involves an additional pump pulse serving as the “mirror”. Two spectral sidebands appear as mirror images of one another about the center frequency of pump  $\omega_0$ .

signs are the opposite [65], i.e.,

$$\beta_{21} = -\beta_{22} = \beta_2. \quad (6.22)$$

Furthermore, this assumption also results in  $\Delta\beta_{11} = \Delta\beta_{12}$  in Eqs. (5.3) and (5.4). Defining  $A_1 = \mathcal{A}_1 \cdot e^{2i\gamma P_0 z}$  and  $A_2 = \mathcal{A}_2 \cdot e^{2i\gamma P_0 z}$ , we obtain the governing equations for the signal  $\mathcal{A}_1$  and idler  $\mathcal{A}_2$  as follows:

$$\frac{\partial \mathcal{A}_1}{\partial z} + \frac{i}{2}\beta_2 \frac{\partial^2 \mathcal{A}_1}{\partial T^2} = i\gamma P_0 \mathcal{A}_2^*, \quad (6.23)$$

$$\frac{\partial \mathcal{A}_2}{\partial z} - \frac{i}{2}\beta_2 \frac{\partial^2 \mathcal{A}_2}{\partial T^2} = i\gamma P_0 \mathcal{A}_1^*, \quad (6.24)$$

where  $\beta_2$  is the magnitude of GVD for both signal and idler. Equations (6.23) and (6.24) appear similar but have two major differences. Firstly, there is a negative sign on the left side of Eq. (6.24) indicating that the GVD for signal and idler are the opposite in sign, although the same in magnitude. The signal propagates in anomalous dispersion while the idler propagates in normal dispersion [65]. Secondly, the evolution of  $\mathcal{A}_1$  involves the complex conjugate of  $\mathcal{A}_2$  on the right side of Eq.(6.23), and vice versa. Thus in fiber optical parametric processes, the gain in one field is proportional to the complex conjugate of the other field. This complex conjugate relationship distinguishes our work from others using Yb-doped or Er-doped fiber amplifiers [75]. For ultrashort pulses in the femtosecond domain, both mechanisms contribute to SMI. When the pulses become longer, in the picosecond domain, the complex-conjugated gain plays the major role in SMI.

Interestingly, by inspecting Eqs. (6.23) and (6.24) one can deduce a self-consistent relation,  $\mathcal{A}_2(t, z) = i\mathcal{A}_1^*(t, z)$ , which exhibits TPC. Furthermore, the analytical solution is obtained in the Fourier domain. Transforming Eqs. (6.23) and (6.24) into Fourier domain gives

$$\tilde{\mathcal{A}}_{1,z} - \frac{i}{2}\beta_2 \omega^2 \tilde{\mathcal{A}}_1 = i\gamma P_0 \tilde{\mathcal{A}}_2^*(-\omega, z), \quad (6.25)$$

$$\tilde{\mathcal{A}}_{2,z} + \frac{i}{2}\beta_2 \omega^2 \tilde{\mathcal{A}}_2 = i\gamma P_0 \tilde{\mathcal{A}}_1^*(-\omega, z). \quad (6.26)$$

We define  $\mu(\omega, z) \doteq e^{-\frac{i}{2}\beta_2 \omega^2 z}$  as the integrating factor then two coupled eqs. are solvable. Since we use ultrashort pulses with high peak power and



fiber with high nonlinearity, the parametric gain  $\gamma P_0$  is extremely high for both femtosecond and picosecond cases. This leads to  $\gamma P_0 L \gg 1$  even after short propagation distance  $L$ . Furthermore, as generally only one of the fields is present at the input, say  $\tilde{\mathcal{A}}_1(\omega, 0) \neq 0$  and  $\tilde{\mathcal{A}}_2(\omega, 0) = 0$ , the solution is given by:

$$\begin{aligned}\tilde{\mathcal{A}}_2(\omega, L) &= \frac{i}{2} e^{\gamma P_0 L} \tilde{\mathcal{A}}_1^*(-\omega, 0) e^{-\frac{i}{2} \beta_2 \omega^2 L} \\ &= i \tilde{\mathcal{A}}_1^*(-\omega, L).\end{aligned}\tag{6.27}$$

Two fields in the frequency domain exhibit the feature of *spectrum reversal*, as shown in Eq. (6.27). This is the counterpart to the self-consistent relation in the time domain. Note that the two fields centered at  $\omega_1$  and  $\omega_2$  are expressed for the relative frequency space in Eq. (6.27). Due to photon energy conservation in optical parametric processes [72], the center frequencies of two sidebands and the center frequency of pump are related as  $\omega_1 + \omega_2 = 2\omega_0$ . Therefore, as shown in the bottom of Fig. 5.1, in absolute frequency space two spectral sidebands are equally separated with respect to the center frequency of pump. Although the exponentially growing fields expressed in Eq. (6.27) quickly saturate in the practical experimental situation [52], our simplified theory gives a simple but clear interpretation of SMI.

The theoretical analysis above shows that SMI occurs naturally in fiber optical parametric processes. However, if the spectrum of the input field is symmetric according to its center frequency, its mirror image spectrum will be identical to the input which makes SMI less evident. In order to better appreciate SMI one needs the spectrum of input to be asymmetric. Fortunately, in most experimental situations there always exist some parasitical effects leading to spectral asymmetry in the frequency domain. The nonlinear phase shift as a function of walk-off leading to an asymmetric multi-peaked spectrum is one such example [66] which we already had discussed in chapter 4.

### 6.3 Analogy between spectral reversal and time reversal

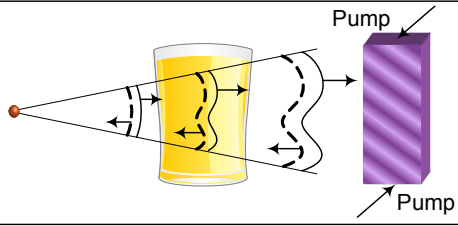
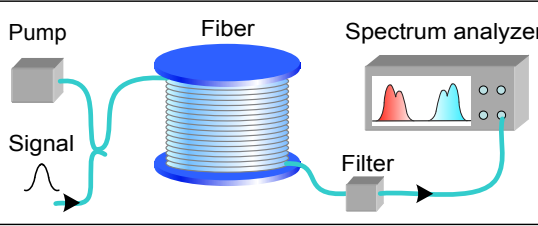
In the previous sections, we discussed the physics of an interesting phenomenon - SMI in the frequency domain. This is a tunable nondegenerate spectrum reversal. Here in this section, we will use this newly observed phenomenon to make a comparison with its counterpart, time reversal, which we briefly discussed in section 6.1.

Time reversal symmetry is based on the reciprocal feature of the wave equation. If a given solution satisfies the wave equation, its time-reversed expression ( $t \rightarrow -t$ ) is also a solution to the original equation. In the optical frequency regime, the time-reversal technique has recently been used in controlling correlated fields for the applications such as turbidity suppression in biological samples [76] and light absorption control in cavities [77]. The fundamental aspect of these schemes is the generation of time-reversed waves, a direct consequence of phase conjugation in the backward geometry for optical beams [78]. Several established nonlinear optical techniques [78, 79] can be used to demonstrate optical phase conjugation, which has emerged as a powerful tool for correcting image distortions [71]. These techniques traditionally involve a bulk photorefractive or third-order nonlinear optical material and a backward degenerate four-wave mixing (FWM) process leading to the time-reversal of optical waves.

Alternatively, it is desirable to perform phase conjugation in a collinearly forward-propagating scheme, which offers long interaction lengths and wavelength tunability. This is especially important for characterizations of the spectral and temporal properties of ultrashort pulses [80, 81, 82]. Here we address the *spectral* and *temporal* properties of the fields in a forward geometry, in contrast to the *spatial* and *temporal* properties in a backward geometry (Summarized in Fig. 6.4). Due to the requirement of sophisticated diagnostic techniques [83, 84] comprehensive experimental studies of temporal phase conjugation (TPC) have not been undertaken till now, although the concept of TPC was used to compensate chromatic dispersion in optical fibers [85]. However, it is convenient to characterize

ultrashort pulses in the frequency domain because such pulses carry broad spectra. Here we demonstrate a tunable nondegenerate spectrum reversal technique which is a spectral realization of optical phase conjugation. This spectral imaging technique provides a new measurable connection between the temporal and spectral properties of correlated fields.

Our demonstration of SMI, while fundamentally interesting, also has enormous potential for applicability. Recently, advanced temporal imaging systems have been demonstrated based on forward partially degenerate FWM processes in fibers and silicon waveguides. These systems perform all-optical ultrafast waveform characterization tasks such as time-to-frequency conversion [80], temporal waveform magnification [81] and packet compression [82]. The key component is the time lens [86], which imparts a quadratic phase modulation onto the input signal pulse. In one realization of a time lens, the nonlinear wave-mixing between a linearly-chirped (i.e., a quadratic variation of the temporal phase) pump pulse and an input signal pulse leads to the generation of an idler pulse with a quadratic temporal phase. The time lens, when combined with dispersive optical fibers for pulse propagation, completes a temporal imaging system. For example, one can construct a system which produces an output idler field with a temporally reversed pulse shape compared with the input signal pulse [81]. Our study generalizes these concepts to the frequency domain. Without the time lens, using an un-chirped pump pulse we demonstrate spectral imaging systems in which two spectral sidebands are mirror images of one another with respect to the center frequency of the pump, i.e., spectral mirror imaging.

Time reversal	Spectrum reversal
	
Narrowband optical beams	Broadband ultrashort pulses
Spatial phase conjugation: $A_2(\vec{r}) \propto A_1^*(\vec{r})$	Temporal phase conjugation: $A_2(t) \propto A_1^*(t)$
Counterpropagation: $\vec{k}_2 = -\vec{k}_1$	Copropagation: $\beta(\omega_2) \approx \beta(\omega_1)$
Degenerate FWM: $\omega_1 = \omega_2 = \omega_0$	Partially degenerate FWM: $\omega_1 + \omega_2 = 2\omega_0$
Wavefront reversal: $E_2(t) \propto E_1(-t)$	Spectral mirror imaging: $ \tilde{A}_2(\omega)  =  \tilde{A}_1(-\omega) $

**Figure 6.4:** Analogy between time reversal and spectrum reversal. The complex wavefunctions of electric fields are  $E_{1,2}$  (the actual electric fields are the real parts  $E_{1,2} = \text{Re}[E_{1,2}]$ ), the complex envelopes are  $A_{1,2}$  and their center frequencies are  $\omega_{1,2}$ . The center frequency of pump is  $\omega_0$ . The wavevectors for optical beams are  $\vec{k}_{1,2}$ . The propagation constants for optical pulses are  $\beta(\omega_{1,2})$ .

Ideally, TPC in the backward geometry [70] could also result in spectrum reversal but the interaction length is limited due to the counterpropagation. One then requires long-pulsed or continuous-wave light sources. Such narrowband light sources make frequency domain measurements difficult [87] and broad wavelength tunability challenging [88]. Therefore, as summarized in Fig. 6.4, the traditional approaches based on counter-propagating narrow-band optical beams lead to time reversal. Here we demonstrate a new technique based on co-propagating optical pulses that offers tunable nondegenerate spectrum reversal.

In summary, we explore SMI features in both femtosecond and picosecond domains and highlight that the opposite values of GVD for signal-idler (two spectral sidebands) and the complex-conjugated gain are the two key physical mechanisms responsible for SMI. As a spectral realization of phase conjugation, SMI offers a measurable connection between the temporal and spectral properties of correlated optical fields. Interestingly, SMI functioned as *spectral mirrors*, when combined with time lenses [80, 81, 82] will complete a set of novel optical components for manipulating temporal and spectral information in ways analogous to traditional imaging. We anticipate these fundamental interests to be the starting point for advancements in diverse applications.

# Chapter 7

## Future studies

During the course of our study, several new interesting directions are identified but have not been detailedly explored in this thesis. We briefly give an introduction to some of them below.

First, in chapter 4 our measurements of output power levels according to the different cavity synchronizations indicated a surprising result: For the signal pulse evolution, its interaction with the trailing edge of pump actually gives highest output power. We believe this is due to the power-dependent phase mismatch [38]. But we would suggest to do an experiment based on a single-pass fiber optical parametric amplifier to verify this guess.

Second, in chapter 5 we did numerical computations of pulse propagation in fiber optical parametric process. Some earlier theories suggest that based on the diode-pumped fiber amplifier it is possible to have a pulse propagating in the self-similar region [89, 90]. We believe that a similar self-similar region exist in fiber optical parametric process. Although have not included in this thesis, we had already performed some preliminary theoretical analyses. More detailed simulation and experimental studies need to be taken in order to verify the existence of this self-similar region.

Furthermore, during the action of numerical computations, we found at certain operational region for fiber optical parametric processes the temporal amplitude (pulse shape) and spectral amplitude of the signal-idler can be surprisingly identical. After the detailed investigation of what had been previously published,

there is a similar method already been demonstrated based on Raman amplifier named as amplified frequency-to-time conversion for real-time spectroscopy [91]. Our theory indicate a similar approach is possible by using parametric gain as well. And we believe this new approach will be more promising as the wider bandwidth from the gain profile and the instantaneous response in comparison with Raman approach.

# Appendix A

## Simulations of ultrashort pulse dynamics using split-step Fourier method

The split-step Fourier method<sup>1</sup> is a numerical calculation tool to solve partial differential equations (PDEs) with nonlinear terms. In particular, this method is widely used to solve the nonlinear Schrödinger equations. It treats the linear and nonlinear terms separately for the contribution of each small step. The linear step is calculated in the frequency domain, and the nonlinear step is calculated in the time domain. Therefore, one needs to apply Fourier transform back and forth to switch between the time domain and frequency domain. To analytical solve PDEs is generally difficult as both linear and nonlinear terms are involved in the equations. However, it is convenient to obtain a numerical solution using the split-step method.

The split-step Fourier method has been applied to a wide variety of optical problems including wave propagation in atmosphere [92], semiconductor lasers [93], unstable resonators [94], and waveguide couplers [95]. Here as an example, we use the split-step Fourier method to simulate the ultrashort pulse propagation in

---

<sup>1</sup>For detail information, please refer to Ref. [32]



optical fibers. We rewrite Eq. (2.8) as:

$$\frac{\partial A}{\partial z} = (\hat{D} + \hat{N})A. \quad (\text{A.1})$$

$$\hat{D} = -\frac{i\beta_2}{2} \frac{\partial^2}{\partial T^2} + \frac{\beta_3}{6} \frac{\partial^3}{\partial T^3} - \frac{\alpha}{2}, \quad (\text{A.2})$$

$$\hat{N} = -i\gamma(|A|^2 + \frac{i}{\omega_0} \frac{1}{A} \frac{\partial}{\partial T} (|A|^2 A - T_R \frac{\partial |A|^2}{\partial T})). \quad (\text{A.3})$$

where  $\hat{D}$  is a linear operator accounting for dispersion and loss, and  $\hat{N}$  is a nonlinear operator that governs various kinds of nonlinear effects. The effects of dispersion and nonlinearity will act together during the pulse propagation. The split-step Fourier method is based on two assumptions. First, the evolution of optical fields is over a tiny small distance  $h$ . Second, the linear and nonlinear effects can be treated independently, i.e., the propagation from  $z$  to  $z + h$  is carried out in two steps. In the first step, the nonlinearity acts alone, i.e., set  $\hat{D}$  to 0 in Eq. (A.1). In the second step, dispersion acts alone, i.e., set  $\hat{N}$  to 0 in Eq. (A.1). Thus the optical field can be written as:

$$\begin{aligned} A(z+h, T) &\approx \exp(h\hat{D}) \exp(h\hat{N})A(z, T) \\ &\approx \exp(\frac{h}{2}\hat{D}) \exp(\int_z^{z+h} \hat{N}(z') dz') \exp(\frac{h}{2}\hat{D})A(z, T). \end{aligned} \quad (\text{A.4})$$

Here, the exponential operator  $\exp(h\hat{D})$  can be evaluated in the Fourier domain as follows

$$\exp(\frac{h}{2}\hat{D})A(z, T) = \mathcal{F}^{-1}\{\exp[\frac{h}{2}\hat{D}(-i\omega)]\}\mathcal{F}\{A(z, T)\}, \quad (\text{A.5})$$

where  $\mathcal{F}$  denotes the Fourier-transform operation,  $\hat{D}(-i\omega)$  is obtained from Eq. (A.2) by replacing the operator  $\partial/\partial T$  by  $-i\omega$ , and  $\omega$  is the frequency in the Fourier domain. The calculation in linear step, i.e., the numerical evaluation of Eq. (A.5), is usually carried out using the Fast Fourier Transform (FFT) algorithm.

The discussion above in Eq. (A.4) - (A.5) is only for each small step, the detailed procedure for the simulation of pulse propagation along a piece of long fiber using the split-step Fourier method is as follows. We need to divide the whole length of fiber into a large number of small segments. First, the optical field  $A(z, T)$  initially propagates for a distance  $h/2$  with dispersion based on Eq. (A.5).

Second, in the middle, the field is multiplied by a nonlinear term <sup>2</sup> that represents the effect of nonlinearity over the entire segment length  $h$ . The pulse propagates from one segment to the next following the evolution by Eq. (A.4), which considers nonlinear effect only. Third, the field propagates for the remaining distance  $h/2$  with dispersion only to obtain  $A(z + h, T)$ .

Suppose the number of steps is  $M$ , i.e.,  $L = Mh$ . The expression of optical fields after the propagation of whole length of fiber is [32]:

$$A(L, T) \approx e^{-\frac{1}{2}h\hat{D}} \left( \prod_{m=1}^M M e^{h\hat{N}} e^{h\hat{D}} \right) e^{-\frac{1}{2}h\hat{D}} A(0, T). \quad (\text{A.6})$$

Therefore, except for the first and last linear steps, all intermediate steps can be carried over the whole segment length  $h$ .

Imposing periodic boundary conditions when using FFT algorithm is justified, as the temporal window used for simulations is usually made much wider than the pulse width. Typically, window size is chosen to be 10 to 20 times of the pulse width.

---

<sup>2</sup>Note that this simplified approach is valid for the contribution of SPM only. For more complex nonlinear effects, the Runge-Kutta methods are used for steps in the time domain.

# Appendix B

## Characterization of ultrafast optical pulses

A pulsed light, or an optical pulse, is usually described by an electromagnetic field of finite time duration. Similar to the approach in Chapter 5, we use normalized complex wavefunction  $E(\mathbf{r}, t)$  to characterize the optical fields. The optical intensity is represented as  $P(\mathbf{r}, t) = |E(\mathbf{r}, t)|^2(W/m^2)$ . Since our major concern is the temporal and spectral properties of an optical pulse at a fixed position  $\mathbf{r}$ , we will rewrite the functions as  $E(t)$  and  $P(t)$  for simplicity.

Except in the few-cycle regime, the complex wavefunction can be written as  $E(t) = A(t)e^{i\omega_0 t}$ , where  $A(t)$  is the complex envelope and  $\omega_0$  is the center frequency. Furthermore, the complex envelope is characterized by its magnitude  $|A(t)|$  and phase  $\varphi(t) = \arg\{A(t)\}$ , so that  $E(t) = |A(t)|e^{i[\omega_0 t + \varphi(t)]}$ . And the integration of the intensity function  $\int P(t)dt$  over the whole pulse duration is the energy density ( $J/m^2$ ). Some typical pulse profiles are the Gaussian function,  $P(t) \propto e^{(-2t^2/\tau^2)}$ , the Lorentzian function  $P(t) \propto 1/(1+t^2/\tau^2)$ , and the hyperbolic secant function  $P(t) \propto \text{sech}^2(t/\tau)$ . For each profile (pulse shape) above, the pulse width is proportional to the time constant  $\tau$ . However, these profiles are only for ideal situations. In practice, the shapes of pulses are complex and difficult to measure.

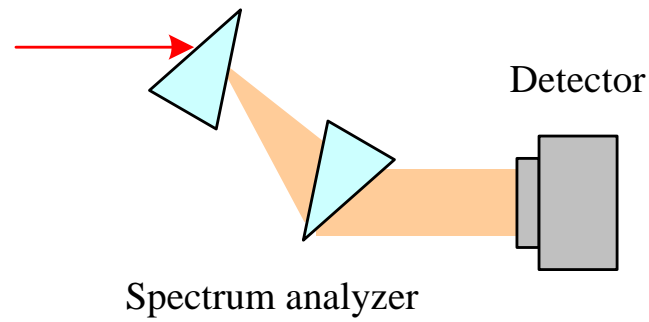
Similarly in the spectral domain, the pulse is described by  $\tilde{E}(\omega) = \int E(t)e^{-i\omega t}dt = |\tilde{E}(\omega)|e^{i\psi(\omega)}$ , where  $\psi(\omega)$  is the spectral phase and  $\tilde{E}(\omega)$  is the spectral amplitude.

Since the function  $\tilde{E}(\omega)$  is centered at  $\omega_0$ , the Fourier transform of the complex envelope  $\tilde{A}(\omega) = \int A(t)e^{-i\omega t}dt = \tilde{E}(\omega - \omega_0)$  is centered at  $\omega = 0$ . By using this expression, we separate slowly-varying complex envelopes  $A(t)$  from fast-varying carrier waves  $e^{-i\omega_0 t}$  as generally our concern is the pulse shape,  $|A(t)|$ . In section B.1, we will first discuss how to characterize an optical pulse in the frequency domain by its spectral intensity  $\tilde{P}(\omega) = |\tilde{E}(\omega)|^2$ .

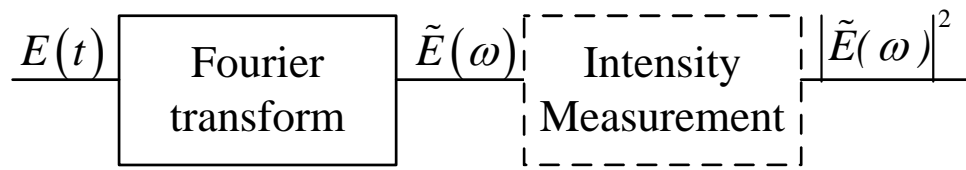
To fully characterize the temporal information of an ultrashort optical pulse is a challenging problem since the fastest available photodetector to date is still too slow. Therefore, most available techniques rely on the use of an ultrafast optical shutter, i.e., time gate, rather than electric or mechanical gate. This time gate, as a reference pulse, should be equal to or shorter than the original pulse for measurement. So in most of the cases, one use part of the energy from the original pulse as the reference for itself. For example, by using beam splitter one can divide the original pulse into two and introduce a controllable delay to one of them. The generation of extra optical field based on nonlinear wave mixing is controlled by an adjustable delay between the reference and the original pulse. Repeated measurements are taken according to the spectral intensity. In section B.2, we will also briefly discuss how to retrieve the temporal information based on the measured results.

## B.1 Optical spectrum analyzer

To fully capture the temporal information, e.g. pulse profile, temporal phase, et al., of ultrashort pulses is usually difficult. However, it is relatively easy to measure the spectral intensity. The spectral intensity  $\tilde{P}(\omega) = |\tilde{A}(\omega)|^2$  of an optical pulse with complex envelope  $A(t)$  may be measured by using an instrument called optical spectrum analyzer. The scheme is summarized in Fig. B.1 (a). This kind of analyzer can be simplified as a set of spectral filters to spatially separate optical fields according to different frequencies or wavelengths. Thus, the “slow” detectors can be used to detect the energy in each of the spectral components, i.e., the spectral intensity  $\tilde{P}(\omega)$ .



(a)



(b)

**Figure B.1:** Measurement of spectral intensity with an optical spectrum analyzer. (a) Schematic of optical implementation using prisms. (b) System.

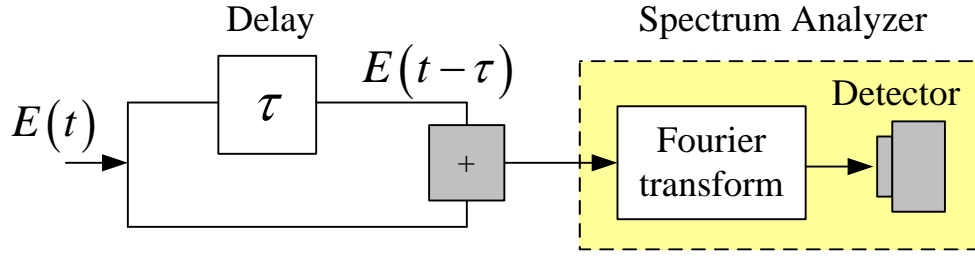


**Figure B.2:** A spectral “interferometer” based on nonlinear effects generates an spectrogram in the frequency domain.

Note, as shown in Fig. B.1 (b), the measurement of spectral intensity will lose the information of spectral phase  $\psi(\omega)$ . Furthermore, it is impossible to retrieve a function  $A(t)$  from the magnitude of its Fourier transform  $\tilde{A}(\omega)$  in the absence of phase information [59].

## B.2 Spectrogram and frequency-resolved optical gating (FROG)

The spectrogram of an optical pulse is a set of time-delay gates in the frequency representation. It equals to the squared magnitude of the Fourier transform of the pulse as seen through a “moving window”, i.e., gating function  $W(t)$ :

$$\Phi(\omega, \tau) = \int E(t)W(t - \tau)e^{-i\omega t} dt \quad (\text{B.1})$$

by defining  $\tilde{P}(\omega, \tau) = |\Phi(\omega, \tau)|^2$ . The spectrogram  $\tilde{P}(\omega)$  can be measured by transmitting the pulse  $E(t)$  through an optical gate controlled by a time-delayed gating function  $W(t - \tau)$ . As depicted schematically in Fig. B.2, the measurement is based on the spectrum of the product  $E(t)W(t - \tau)$  at each time delay  $\tau$ . An optical implementation relies on a pair of moving mirrors to introduce the time delay, and a spectrum analyzer as shown in Fig. B.1, functioned as Fourier transform. This technique is known as frequency-resolved optical gating (FROG).

Since a sufficiently short gating function  $W(t)$  for the measurement of an ultrashort pulses is usually unavailable, one can use the pulse  $E(t)$  itself for the

purpose of time gate. Furthermore, the product function  $E(t)E(t - \tau)$  is usually achieved by using nonlinear optical techniques, where a popular approach is based on second-harmonic generation (SHG). For a SHG gate with input waves  $E(t)$  and  $E(t - \tau)$  at the fundamental frequency, the wave at the second-harmonic frequency is proportional to the product  $E(t)E(t - \tau)$ . Then the function is given as

$$\Phi(\omega, \tau) = \int E(t)E(t - \tau)e^{-i\omega t} dt. \quad (\text{B.2})$$

The overall optical system known as the SHG-FROG is depicted in Fig. B.3.

As we previously mentioned, the spectrogram  $\tilde{P}(\omega, \tau)$  is a 2D “picture” that can be used to characterize optical pulses. Based on this spectrogram, one can retrieve the temporal information of original pulse, i.e., the temporal amplitude and phase of complex wavefunction  $E(t)$ . However, the retrieval procedure is not straightforward. and here we will have a briefly discussion.

A general expression for  $\tilde{P}(\omega, \tau)$ , measured by the nonlinear optical gating systems, can be written in the form

$$\Phi(\omega, \tau) = \int g(t, \tau)e^{-i\omega t} dt, \quad (\text{B.3})$$

where  $g(t, \tau) = E(t)W(t - \tau)$ .

Suppose the complex function  $\Phi(\omega, \tau)$  were known, one can take the inverse Fourier transform of  $\Phi(\omega, \tau)$  with respect to  $\omega$  at each  $\tau$ ,

$$g(t, \tau) = \int \Phi(\omega, \tau)e^{i\omega t} d\omega. \quad (\text{B.4})$$

Then the wavefunction  $E(t)$  may be computed by integration over  $\tau$ , and we can derive a proportional relation as

$$\int g(t, \tau) d\tau = \int E(t)W(t - \tau) d\tau = E(t) \int W(t - \tau) d\tau \propto E(t). \quad (\text{B.5})$$

This indicates the proportional constant is the same as the area of the window function. Till now, it seems that we have solved this “problem” - to retrieve the temporal information of optical pulse. But actually the phase of complex function  $\Phi(\omega, \tau)$  is unknown in the beginning. Therefore, the problem of estimating  $\Phi(\omega, \tau)$  from the measured  $\tilde{P}(\omega, \tau) = |\Phi(\omega, \tau)|^2$  is a “missing-phase” problem. The

real procedure is as follows. First, we need to have an initial guess of the phase  $\arg\{\Phi(\omega, \tau)\}$  to get the  $E(t)$ . Second, we calculate the spectrogram  $\tilde{P}(\omega, \tau)$  based on  $E(t)$ . Third, by comparing this calculated spectrogram with the measured one, we can have a better guess of the phase  $\arg\{\Phi(\omega, \tau)\}$ . The process is repeated until it converges to a pulse wavefunction  $E(t)$  that is consistent with the measured spectrogram<sup>1</sup>.

Here we show two examples which present the detailed information in section 3.3. Figure B.4 is a screenshot of a commercial software for FROG simulation-Femtosoft Technologies 3.2.2. The top left window shows the original measured spectrogram. Two windows on the right side show the calculated optical field in the time domain and frequency domain. Based on these calculations above, the reconstructed spectrogram is shown on the bottom left corner. The window in the middle shows the parameters used in the computation. By clicking “start”, the software starts to run. After a while, when we click the “stop” button, the software will display the result with smallest error and save the retrieved results. The data in Fig. B.4 is about the temporal and spectral information of output pulses from FOPO, corresponding to the data points shown in Fig. 3.8 (a) with the PCF length at 61 mm.

As shown in Fig. B.5, the retrieved temporal information of optical pulses in the right column is based on the original spectrograms in the left column. All the results are the detail information of the experimental data points in Fig. 3.8 (a), when the operation of FOPO is at long wavelength.

---

<sup>1</sup>For detail information, please refer to [59].



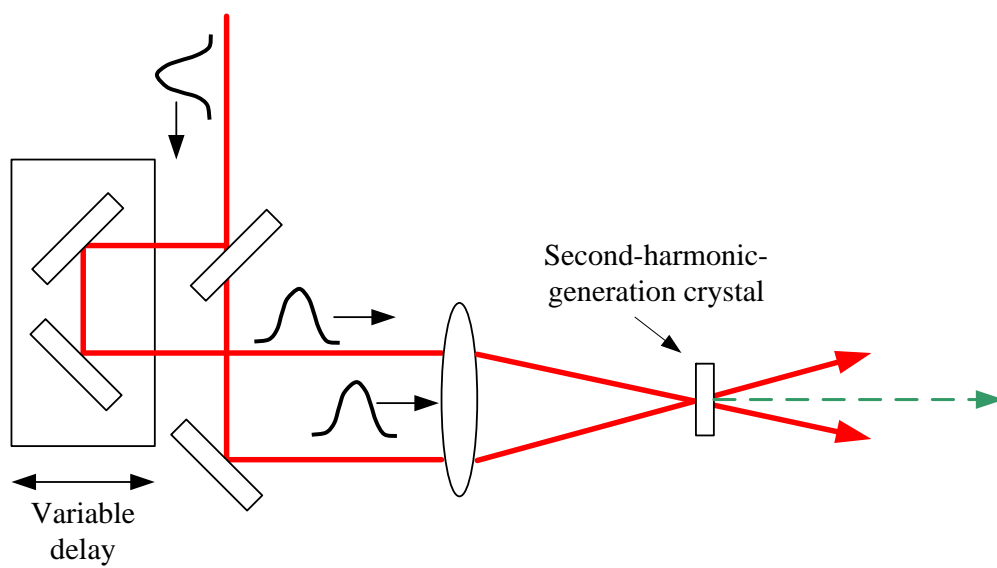


**Figure B.3:** Schematic of a second-harmonic generation frequency-resolved optical gating.

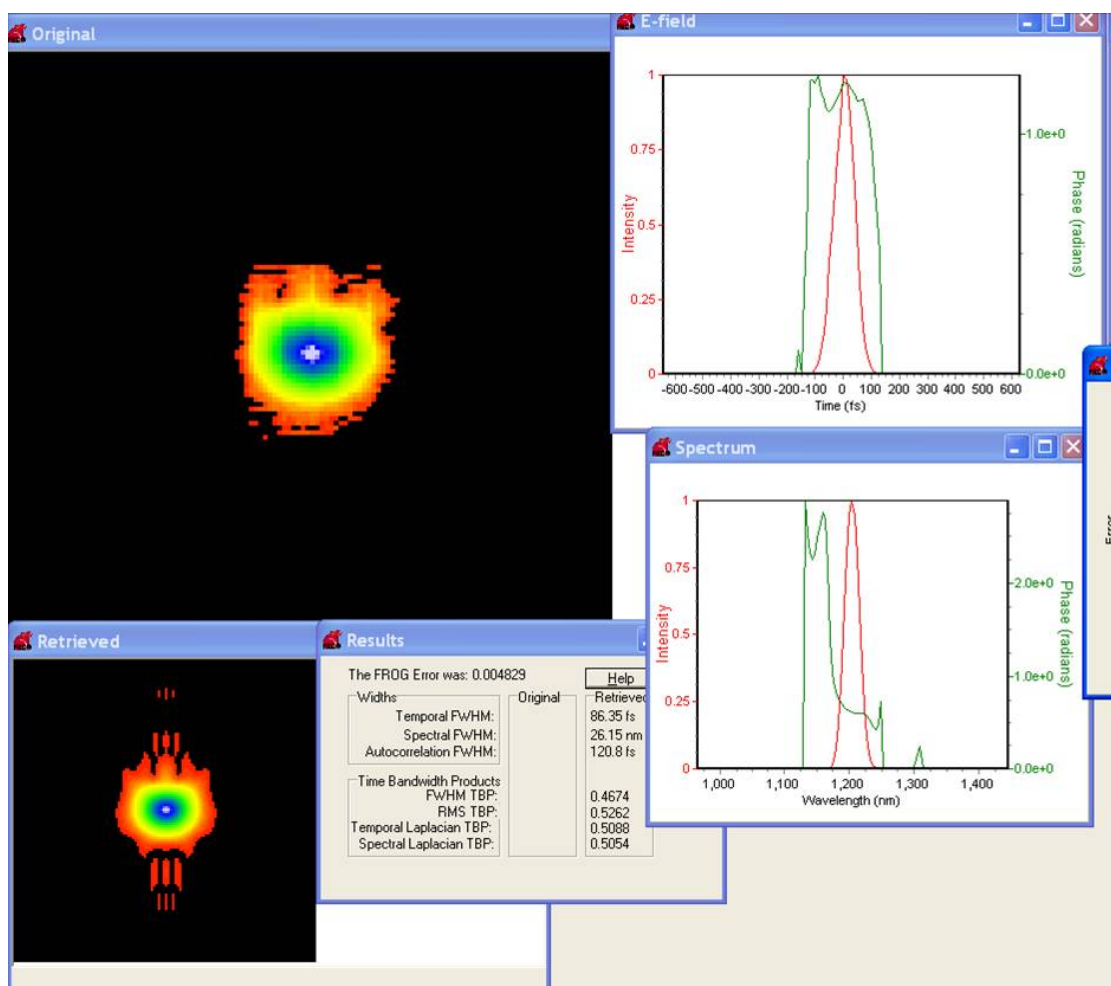


**Figure B.4:** Original and retrieved FROG data with the center wavelength at 1212 nm and a pulse duration of 86.35 fs.

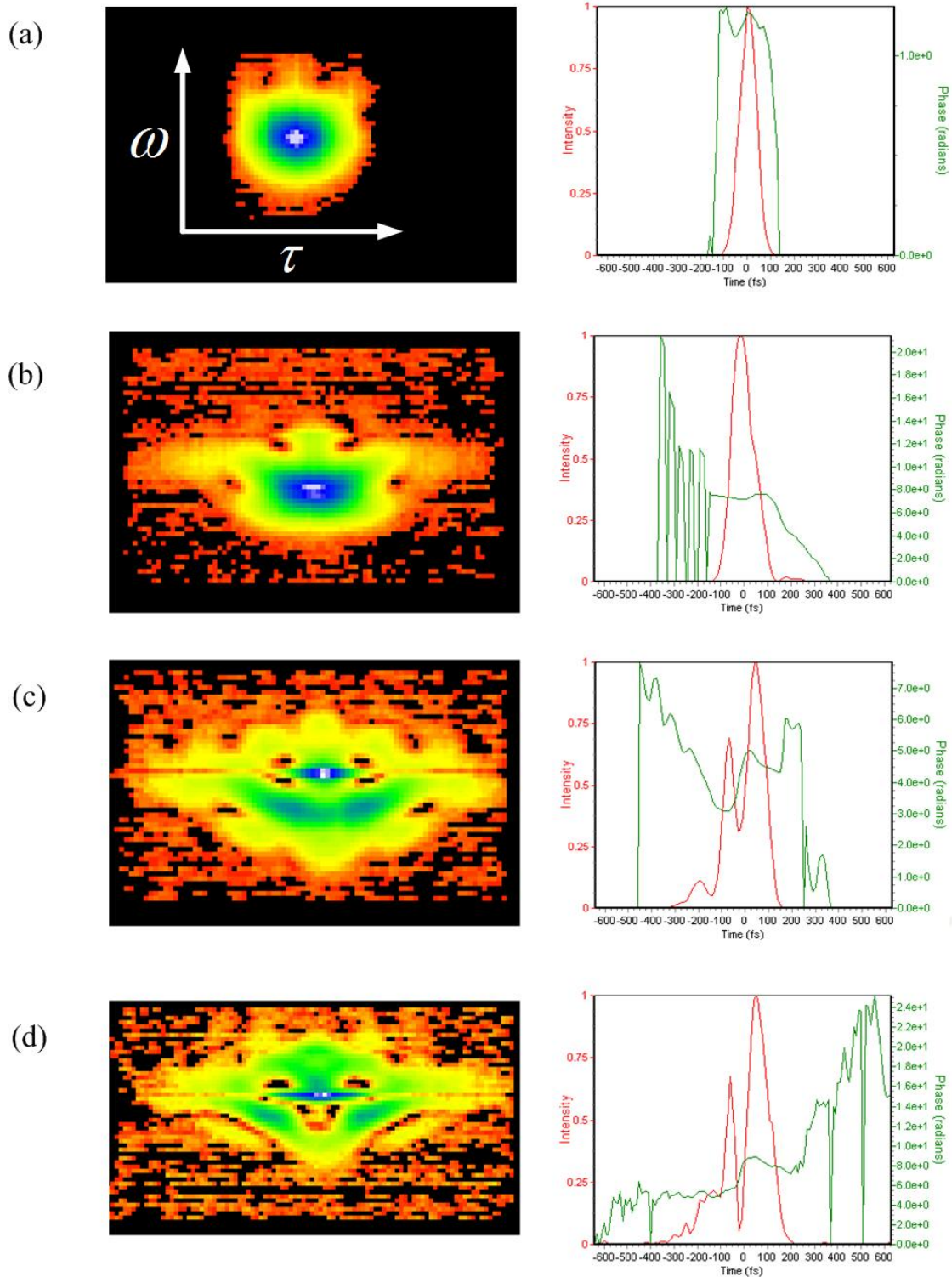


**Figure B.5:** A variety of measured spectrograms and retrieved pulses. (a) The pulse duration is  $86.35\text{fs}$  and the center wavelength is  $1212\text{nm}$ . (b) The pulse duration is  $114.2\text{fs}$  and the center wavelength is  $1223\text{nm}$ . (c) The pulse duration is  $183.1\text{fs}$  and the center wavelength is  $1240\text{nm}$ . (d) The pulse duration is  $182.3\text{fs}$  and the center wavelength is  $1262\text{nm}$ .

# Bibliography

- [1] T. H. Maiman, “Stimulated optical radiation in ruby”, *Nature* 187, 493-494 (1960).
- [2] P. A. Franken, A. E. Hill, C. W. Peters, and G. Weinreich, “Generation of optical harmonics”, *Phys. Rev. Lett.* 7, 118-119 (1961).
- [3] E. J. Woodbury and W. K. Ng, “Ruby laser operation in the near IR”, *Proc. IRE* 50, 2367 (1962).
- [4] R. Y. Chiao, C. H. Townes, and B. P. Stoicheff, “Stimulated Brillouin scattering and coherent generation of intense hypersonic waves”, *Phys. Rev. Lett.* 12, 592-595 (1964).
- [5] R. L. Carman, R. Y. Chiao, and P. L. Kelly, “Observation of degenerate stimulated four-photon interaction and four-wave parametric amplification”, *Phys. Rev. Lett.* 17, 1281-1283 (1966).
- [6] F. P. Kapron, D. B. Keck, and R. D. Maurer, “Radiation losses in glass optical waveguides”, *Appl. Phys. Lett.* 17, 423-425 (1970).
- [7] R. H. Stolen, E. P. Ippen, and A. R. Tynes, “Raman oscillation in glass optical waveguide”, *Appl. Phys. Lett.* 20, 62-64 (1972).
- [8] E. P. Ippen and R. H. Stolen, “Stimulated Brillouin scattering in optical fibers”, *Appl. Phys. Lett.* 21, 539-541 (1972).
- [9] R. H. Stolen and A. Ashkin, “Optical Kerr effect in glass waveguide”, *Appl. Phys. Lett.* 22, 294-296 (1973).
- [10] R. H. Stolen, J. E. Bjorkholm, and A. Ashkin, “Phase-matched three-wave mixing in silica fiber optical waveguides”, *Appl. Phys. Lett.* 24, 308-310 (1974).
- [11] R. H. Stolen, “Phase-matched-stimulated four-photon mixing in silica-fiber waveguides”, *IEEE J. Quantum Electron.* 11, 100-103 (1975).
- [12] R. H. Stolen and C. Lin, “Self-phase-modulation in silica optical fibers”, *Phys. Rev. A* 17, 1448-1453 (1978).

- [13] R. H. Stolen, "The early years of fiber nonlinear optics", *J. Lightwave Technol.* 26, 1021-1031 (2008).
- [14] A. Hasegawa and F. Tappert, "Transmission of stationary nonlinear optical pulses in dispersive dielectric fibers: I. Anomalous dispersion", *Appl. Phys. Lett.* 23, 142-144 (1973).
- [15] L. F. Mollenauer, R. H. Stolen, and J. P. Gordon, "Experimental observation of picosecond pulse narrowing and solitons in optical fibers", *Phys. Rev. Lett.* 45, 1095-1098 (1980).
- [16] L. F. Mollenauer and R. H. Stolen, "The soliton laser", *Opt. Lett.* 9, 13-15 (1984).
- [17] P. S. J. Russell, "Photonic-crystal fibers", *J. Lightwave Technol.* 24, 4729-4749 (2006).
- [18] N. G. R. Broderick, T. M. Monro, P. J. Bennett and D. J. Richardson, "Non-linearity in holey optical fibers: measurement and future opportunities", *Opt. Lett.* 24, 1395-1397 (1999).
- [19] J. M. Dudley, G. Genty, and S. Coen, "Supercontinuum generation in photonic crystal fiber", *Rev. Mod. Phys.* 78, 1135-1184 (2006).
- [20] J. C. Knight, and D. V. Skryabin, "Nonlinear waveguide optics and photonic crystal fibers", *Opt. Express* 15, 15365-15376 (2007).
- [21] A. R. Bhagwat, and A. L. Gaeta, "Nonlinear optics in hollow-core bandgap fibers", *Opt. Express* 16, 5035-5047 (2008).
- [22] M. A. Foster, A. C. Turner, M. Lipson, and A. L. Gaeta, "Nonlinear optics in photonic nanowires", *Opt. Express* 16, 1300-1320 (2008).
- [23] J. L. Hall, and T. W. Häsch, in *Femtosecond Optical Frequency Comb Technology: Principle, Operation, and Application*, (eds Ye, J. & Cundiff, S. T.) 1-11 (Springer, 2005).
- [24] W. J. Wadsworth, R.M. Percival, G. Bouwmans, J.C. Knight, T.A. Birks, T.D. Hedley, and P. St. J. Russell, "Very high numerical aperture fibers", *IEEE Photon. Technol. Lett.* 16, 843 (2004).
- [25] T.A. Birks, J.C. Knight, and P.St.J. Russell, "Endlessly single-mode photonic crystal fibre", *Opt. Lett.* 22, 961 (1997).
- [26] J. C. Knight, T. A. Birks, R. F. Cregan, P. St. J. Russell, and P. D. de Sandro, "Large mode area photonic crystal fibre", *Electron. Lett.* 34, 1347 (1998).

- [27] J. M. Dudley, “Supercontinuum generation in photonic crystal fiber”. *Rev. Mod. Phys.* 78, 1135 (2006).
- [28] J. C. Knight, J. Arriaga, T. A. Birks, A. Ortigosa-Blanch, W. J. Wadsworth, and P. St. J. Russell, “Anomalous dispersion in photonic crystal fiber”, *IEEE Photon. Technol. Lett.* 12, 807 (2000).
- [29] A. Nolan, G. E. Berkey, M. Li, X. Chen, W. A. Wood, and L. A. Zenteno, “Single-polarization fiber with a high extinction ratio”, *Opt. Lett.* 2, 1855 (2004).
- [30] T. Schreiber, F. Röser, O. Schmidt, J. Limpert, R. Iliew, F. Lederer, A. Petersson, C. Jacobsen, K. Hansen, J. Broeng, and A. Tünnermann, “Stress-induced single-polarization single-transverse mode photonic crystal fiber with low nonlinearity”, *Opt. Express* 13, 7621 (2005).
- [31] P. S. J. Russell, “Photonic crystal fibers”, *Science* 299, 358 (2003).
- [32] G. P. Agrawal, *Nonlinear Fiber Optics*, 4th ed., Academic Press, New York, (2006).
- [33] R. H. Stolen, J. P. Gordon, W. J. Tomlinson, and H. A. Haus, “Raman response function of silica-core fibers”, *J. Opt. Soc. Am. B* 6, 1159-1166 (1989).
- [34] R. H. Stolen and J. E. Bjorkholm, “Parametric amplification and frequency conversion in optical fibers”, *IEEE J. Quantum Electron.*, vol. QE-18, 1062-1072, (1982).
- [35] G. Cappellini and S. Trillo, “Third-order three-wave mixing in single-mode fibers: exact solutions and spatial instability effects”, *J. Opt. Soc. Amer. B*, 8, 824-838 (1991).
- [36] A. Vatarescu, “Light conversion in nonlinear single-mode optical fibers”, *J. Lightwave Technol.*, 5, 1652-1659, (1987).
- [37] Z. Tong, C. Lundström, P. A. Andrekson, C. J. McKinstrie, M. Karlsson, D. J. Blessing, E. Tipsuwannakul, B. J. Puttnam, H. Toda and L. Grüner-Nielsen, “Towards ultrasensitive optical links enabled by low-noise phase-sensitive amplifiers”, *Nature Photonics* 5, 430-436 (2011).
- [38] K. Inoue and T. Mukai, “Signal wavelength dependence of gain saturation in a fiber optical parametric amplifier”, *Opt. Lett.* 26, 10-12 (2001).
- [39] M. E. Marhic, N. Kagi, T.-K. Chiang, and L. G. Kazovsky, “Broadband fiber optical parametric amplifiers”, *Opt. Lett.*, 21, 573-575, (1996).

- [40] P. A. Andrekson, M. Westlund, J. Li and P.-O. Hedekvist, "Fiber-based optical parametric amplifiers and their applications", *IEEE J. Quantum Electron.*, 8, 506-520, (2002).
- [41] J. E. Sharping, "Microstructure Fiber Based Optical Parametric Oscillators", *J. Lightw. Technol.* 26, 2184 (2008).
- [42] M. H. Dunn and M. Ebrahimzadeh, "Parametric generation of tunable light from continuous-wave to femtosecond pulses," *Science* 286, 1513-1517, (1999).
- [43] J. C. Diels, and W. Rudolph, *Ultrashort laser pulse phenomena*, Academic Press, (1996).
- [44] M. Dantus, and V. Lozovoy, "Experimental coherent laser control of physico-chemical processes", *Chem. Rev.* 104, 1813-1859, (2004).
- [45] F. Ganikhanov, S. Carrasco, X. Sunney Xie, M. Katz, W. Seitz, and D. Kopf, "Broadly tunable dual-wavelength light source for coherent anti-Stokes Raman scattering microscopy", *Opt. Lett.* 31, 1292-1294, (2006).
- [46] M. E. Marhic, K. K.-Y. Wong, G. Kalogerakis, and L. G. Kazovsky, "Toward Practical Fiber Optical Parametric Amplifiers and Oscillators", *Opt. Photon. News* 15, 20-25 (2004).
- [47] Y. Q. Xu, S. G. Murdoch, R. Leonhardt, and J. D. Harvey, "Widely tunable photonic crystal fiber Fabry-Perot optical parametric oscillator", *Opt. Lett.* 33, 1351-1353 (2008).
- [48] J. E. Sharping, M. A. Foster, A. L. Gaeta, J. Lasri, O. Lyngnes, and K. Vogel, "Octave-spanning, high-power microstructure-fiber-based optical parametric oscillators", *Opt. Express* 15, 1474-1479 (2007).
- [49] J. E. Sharping, C. Pailo, C. Gu, L. Kiani, and J. R. Sanborn, "Microstructure fiber optical parametric oscillator with femtosecond output in the 1200 to 1350 nm wavelength range ", *Opt. Express* 18, 3911-3916 (2010).
- [50] K. Kieu, B. G. Saar, G. R. Holtom, X. S. Xie, and F. W. Wise, "High-power picosecond fiber source for coherent Raman microscopy", *Opt. Lett.* 34, 2051-2053 (2009).
- [51] H. Chen, H. Wang, M. N. Slipchenko, Y. Jung, Y. Shi, J. Zhu, K. K. Buhman, and J. Cheng, "A multimodal platform for nonlinear optical microscopy and microspectroscopy ", *Opt. Express* 17, 1282-1290 (2009).
- [52] M. E. Marhic, *Fiber Optical Parametric Amplifiers, Oscillators and Related Devices* (Cambridge Univ. Press, London, 2008).

- [53] Y. Zhou, K. K. Y. Cheung, S. Yang, P. C. Chui, and K. K. Y. Wong, “Widely-tunable picosecond optical parametric oscillator using highly-nonlinear fiber”, *Opt. Lett.* 34, 989 (2009).
- [54] C. Gu, H. Wei, S. Chen, W. Tong, and J. E. Sharping, “Fiber optical parametric oscillator for sub-50 fs pulse generation: optimization of fiber length”, *Opt. Lett.* 35, 351 (2010).
- [55] Y. Zhai, C. Pailo, M. Slipchenko, D. Zhang, H. Wei, S. Chen, W. Tong, J. Cheng, and J. E. Sharping, “Fiber OPO for Multimodal CARS Imaging”, *Frontiers in Optics, FMG4*, (2010).
- [56] A. Y. H. Chen, G. K. L. Wong, S. G. Murdoch, R. Leonhardt, J. D. Harvey, J. C. Knight, W. J. Wadsworth, and P. St. J. Russell, “Widely tunable optical parametric generation in a photonic crystal fiber”, *Opt. Lett.*, 30, 762-764 (2005).
- [57] Y. Q. Xu and S. G. Murdoch, “High conversion efficiency fiber optical parametric oscillator”, *Opt. Lett.*, 36, 4266-4268 (2011).
- [58] J. E. Sharping, J. R. Sanborn, M. A. Foster, D. Broaddus, and A. L. Gaeta, “Generation of sub-100-fs pulses from a microstructure-fiber-based optical parametric oscillator”, *Opt. Express* 16, 18050-18056 (2008).
- [59] R. Trebino, *Frequency-resolved optical gating : the measurement of ultrashort laser pulses*, (Kluwer Academic Publishers, 2000).
- [60] J. D. V. Khaydarov, J. H. Andrews, and K. D. Singer, “Pulse-compression mechanism in a synchronously pumped optical parametric oscillator ”, *J. Opt. Soc. Am. B* 12, 2199-2208 (1995).
- [61] L. Lefort, K. Puech, S. D. Butterworth, Y. P. Svirko, and D. C. Hanna, “Generation of femtosecond pulses from order-of-magnitude pulse compression in a synchronously pumped optical parametric oscillator based on periodically poled lithium niobate ”, *Opt. Lett.* 24, 28-30 (1999).
- [62] Y. Zhou, B. P. P. Kuo, K. K. Y. Cheung, S. Yang, P. C. Chui, and K. K.-Y. Wong, “Wide-Band Generation of Picosecond Pulse Using Fiber Optical Parametric Amplifier and Oscillator ”, *IEEE J. Quant. Electron.* 45, 1350-1356 (2009).
- [63] G. P. Agrawal, P. L. Baldeck, and R. R. Alfano, “Temporal and spectral effects of cross-phase modulation on copropagating ultrashort pulses in optical fibers”, *Phys. Rev. A* 39, 5063 (1989).
- [64] M. N. Islam, L. F. Mollenauer, R. H. Stolen, J. R. Simpson, and H. T. Shang, “Cross-phase modulation in optical fibers”, *Opt. Lett.* 31, 625 (1987).



- [65] S. Wabnitz, and J. M. Soto-Crespo, “Stable coupled conjugate solitary waves in optical fibers”, *Opt. Lett.* 23, 265-267 (1998).
- [66] C. Gu, C. Goulart, and J. E. Sharping, “Cross-phase-modulation-induced spectral effects in high-efficiency picosecond fiber optical parametric oscillators”. *Opt. Lett.* 36, 1488-1490 (2011).
- [67] P. L. Baldeck, R. R. Alfano, and G. P. Agrawal, “Induced - frequency shift of copropagating ultrafast optical pulses”, *Appl. Phys. Lett.* 52, 1939 (1988).
- [68] B. Ya. Zel’Dovich, N. F. Pilipetsky and V. V. Shkunov, *Principles of Phase Conjugation*, Springer Series in Optical Sciences, (1985).
- [69] R. A. Fisher, *Optical Phase Conjugation*, Academic Press, Optics and Photonics Series, (1983).
- [70] A. Yariv, D. Fekete and D. M. Pepper, “Compensation for channel dispersion by nonlinear optical phase conjugation”, *Opt. Lett.* 4, 52-54 (1979).
- [71] D. M. Pepper, “Applications of Optical Phase Conjugation”, *Scientific American* 254, 74-83 (1986).
- [72] R. W. Boyd, *Nonlinear Optics* (Academic Press, New York, 2008).
- [73] A. Yariv and D. M. Pepper, “Amplified reflection, phase conjugation, and oscillation in degenerate four-wave mixing”, *Opt. Lett.*, 1, 16-18 (1977).
- [74] P. Vizmuller, *RF Design Guide Systems, Circuits And Equations* (Artech House Antennas and Propagation Library, Boston, 1995).
- [75] M. J. F. Digonnet, *Rare-Earth-Doped Fiber Lasers and Amplifiers* (CRC Press, New York, 2001).
- [76] Z. Yaqoob, D. Psaltis, M. S. Feld, and C. Yang, “Optical phase conjugation for turbidity suppression in biological samples”, *Nature Photon.* 2, 110-115 (2008).
- [77] W. Wan, Y. Chong, L. Ge, H. Noh, A. D. Stone and H. Cao, “Time-Reversed Lasing and Interferometric Control of Absorption”, *Science* 331, 889-892 (2011).
- [78] A. Yariv, “Phase conjugate optics and real-time holography”, *IEEE J. Quant. Electron.* 14, 650-660 (1978).
- [79] P. Yeh, *Introduction To Photorefractive Nonlinear Optics* (Wiley Series in Pure and Applied Optics, New York, 1993).

- [80] M. A. Foster, R. Salem, D. F. Geraghty, A. C. Turner-Foster, M. Lipson, and A. L. Gaeta, "Silicon-chip-based ultrafast optical oscilloscope". *Nature* 456, 81-84 (2008).
- [81] R. Salem, M. A. Foster, A. C. Turner, D. F. Geraghty, M. Lipson, and A. L. Gaeta, "Optical time lens based on four-wave mixing on a silicon chip". *Opt. Lett.* 33, 1047-1049 (2008).
- [82] M. A. Foster, R. Salem, Y. Okawachi, A. C. Turner-Foster, M. Lipson, A. L. Gaeta, "Ultrafast waveform compression using a time-domain telescope", *Nature Photon.* 3, 581-585 (2009).
- [83] R. Trebino, *Frequency-Resolved Optical Gating: The Measurement Of Ultrashort Laser Pulses* (Kluwer, Boston, 2002).
- [84] C. Iaconis and I. A. Walmsley, "Spectral phase interferometry for direct electric-field reconstruction of ultrashort optical pulses", *Opt. Lett.* 23, 792-794 (1998).
- [85] S. Watanabe, T. Naito, and T. Chikama, "Compensation of chromatic dispersion in a single-mode fiber by optical phase conjugation", *IEEE Photon. Technol. Lett.* 5, 92-95 (1993).
- [86] B. H. Kolner, "Space-time duality and the theory of temporal imaging". *IEEE J. Quant. Electron.* 30, 1951-1963 (1994).
- [87] K. Mori, T. Morioka, and M. Saruwatari, "Wavelength-shift-free spectral inversion with an optical parametric loop mirror", *Opt. Lett.* 21, 110-112 (1996).
- [88] K. Inoue, "Spectral inversion with no wavelength shift based on four-wave mixing with orthogonal pump beams", *Opt. Lett.* 22, 1772-1774 (1997).  
"Multimodal coherent anti-Stokes Raman spectroscopic imaging with a fiber optical parametric oscillator", *Appl. Phys. Lett.* 98, 191106 (2011).
- [89] M. E. Fermann, V. I. Kruglov, B. C. Thomsen, J. M. Dudley, and J. D. Harvey, "Self-Similar Propagation and Amplification of Parabolic Pulses in Optical Fibers", *Phys. Rev. Lett.* 84, 6010 (2000).
- [90] J. M. Dudley, C. Finot, D. J. Richardson, and G. Millot, "Self-similarity in ultrafast nonlinear optics", *Nature Physics* 3, 597-603 (2007).
- [91] D. R. Solli, J. Chou, and B. Jalali, "Amplified wavelength-time transformation for real-time spectroscopy", *Nature Photonics* 2, 48-51 (2007).
- [92] M. Lax, J. H. Batteh, and G. P. Agrawal, "Channeling of intense electromagnetic beams", *J. Appl. Phys.* 52, 109 (1981).

- [93] G. P. Agrawal, “Fast-Fourier-transform based beam-propagation model for stripe-geometry semiconductor lasers: Inclusion of axial effects”, *J. Appl. Phys.* 56, 3100 (1984).
- [94] M. Lax, G. P. Agrawal, M. Belic, B. J. Coffey, and W. H. Louisell, “Electromagnetic-field distribution in loaded unstable resonators”, *J. Opt. Soc. Am. A* 2, 731 (1985).
- [95] B. Hermansson, D. Yevick, and P. Danielsen, “Propagating beam analysis of multimode waveguide tapers ”, *IEEE J. Quantum Electron.* 19, 1246 (1983).